Tunnelling and noise in GaAs and graphene nanostructures

Submitted by Alexander S. Mayorov to the University of Exeter as a thesis for the degree of Doctor of Philosophy in Physics
September, 2008

I certify that all material in this thesis which is not my own work has been identified and that no material has previously been submitted and approved for the award of a degree by this or any other University.

Alexander S. Mayorov
September, 2008

Abstract

Experimental studies presented in this thesis have shown the first realisation of resonant tunnelling transport through two impurities in a vertical double-barrier tunnelling diode; have proved the chiral nature of charge carriers in graphene by studying ballistic transport through graphene p-n junctions; have demonstrated significant differences of $1/f$ noise in graphene compared with conventional two-dimensional systems.

Magnetic field parallel to the current has been used to investigate resonant tunnelling through a double impurity in a vertical double-barrier resonant tunnelling diode, by measuring the current-voltage and differential conductance-voltage characteristics of the structure. It is shown that such experiments allow one to obtain the energy levels, the effective electron mass and spatial positions of the impurities.

The chiral nature of the carriers in graphene has been demonstrated by comparing measurements of the conductance of a graphene p-n-p structure with the predictions of diffusive models. This allowed us to find, unambiguously, the contribution of ballistic resistance of graphene p-n junctions to the total resistance of the p-n-p structure. In order to do this, the band profile of the p-n-p structure has been calculated using the realistic density of states in graphene. It has been shown that the developed models of diffusive transport can be applied to explain the main features of the magnetoresistance of p-n-p structures.

It was shown that $1/f$ noise in graphene has much more complicated concentration and temperature dependences near the Dirac point than in usual metallic systems, possibly due to the existence of the electron-hole puddles in the electroneutrality region. In the regions of high carrier concentration where no inhomogeneity is expected, the noise has an inverse square root dependence on the concentration, which is also in contradiction with the Hooge relation.

Acknowledgements

I would like here to say thank you to several people who helped me during my years of research at the university of Exeter. Firstly to my supervisor Alex Savchenko, for his encouragement and support. A lot of thanks also go to the PhD students I worked with: Evgeniy Galaktionov, Fedor Tikhonenko. Special thanks to Adam Price who corrected my English and David Horsell who read this thesis and spent a lot of time to make it clearer. Great thanks go to Andrew Kretinin from whom I learned how to measure noise.

The DBRTD sample was supplied by Giancarlo Faini of the Laboratoire de Photonique et Nanostructures, CNRS in Marcoussis, France. I am grateful to Roman Gorbachev who fabricated all graphene samples I have used. Also I want to thank Alex Beaton who helped me with the graphene doping experiment.

Thanks to theoreticians Matvey Entin from the Institute of Semiconductor Physics, Novosibirsk, Russia and Francisco Guinea from Instituto de Ciencia de Materiales de Madrid, Spain, who helped me to get a better understanding of the physics I was dealing with. Also I would like to express my gratitude to Professor Kvon Ze Don from the Institute of Semiconductor Physics, Novosibirsk with whom I worked for a month. He was also the one who told me about Exeter university, and the ORS scholarship.

I would like to thank all the technical staff in the Physics Department who helped me, especially Dave Manning and Adam Woodgate for their generous supply of liquid helium, and Paul Wilkins for solving all my technical problems.

Finally, I owe a big thank you to my mother Tat'yana, and to my sister Maria for support over the last years. Thanks to my friends Alexey Petrenko and Anatoly Patrakov who were not here but helped me a lot. I would like to thanks Mr. and Mrs. Allison who ensured that I did not have any problem with my accommodation during my PhD study.

Thanks also to all the people I have interacted with during my PhD study at Exeter but did not mention here.

Contents

List of Figures

List of Tables

List of publications

Publications

- R. V. Gorbachev, A. S. Mayorov, A. K. Savchenko, D. W. Horsell, F. Guinea Conductance of p-n-p Graphene Structures with Air-Bridge Top Gates Nano Lett. 8, 1995 (2008).

- R. V. Gorbachev, F. V. Tikhonenko, A. S. Mayorov, D. W. Horsell, A. K. Savchenko Weak localisation in bilayer graphene Physica E 40, 1360 (2008).

- A. S. Mayorov, Z. D. Kvon, A. K. Savchenko, D. V. Scheglov, A. V. Latyshev Coulomb blockade in an open small ring with strong backscattering Physica E 40, 1121 (2008).

- R. V. Gorbachev, F. V. Tikhonenko, A. S. Mayorov, D. W. Horsell, and A. K. Savchenko Weak Localization in Bilayer Graphene Phys. Rev. Lett. 98, 176805 (2007).

- A. S. Mayorov, A. K. Savchenko, M. V. Entin, G. Faini, F. Laruelle, and E. Bedel Resonant tunnelling via two impurity levels in a vertical tunnelling nanostructure Phys. Stat. Sol. (c) 4, 505 (2007).

- A. V. Kretinin, S. H. Roshko, A. K. Savchenko, A. S. Mayorov, and Z. D. Kvon 1/f noise near the metal-to-insulator transition in the 2DEG in a Si-MOSFET Phys. Stat. Sol. (c) 3, 339 (2006).

Conference presentations

- International Conference on Superlattices, Nanostructures and Nanodevices (ICSNN 2006) Oral contribution: Resonant tunnelling via two impurity levels in a vertical tunnelling nanostructure

- International Conference on Superlattices, Nanostructures and Nanodevices (ICSNN 2006) Poster contribution: Resistance fluctuations near the metal-to-insulator transition in the DEG in a Si-MOSFET

Introduction

Due to miniaturisation trends in semiconductor technology, interest in mesoscopic physics research has risen over the last three decades. Nanotechnology has grown into a separate field of modern science, which will have wide applications in the future. The state of the art in the field is to control the movement of a single electron through a nanodevice such as a resonant tunnelling diode. Different methods of tunnelling spectroscopy are an important tool for investigating the electronic structure of these nanodevices in the energy, and momentum space. Studies have been done on such systems as quantum dots, quantum wells, and ballistic transistors. Zero-dimensional structures where electrons are confined in all three dimensions have been used to investigate properties of the surrounding contacts, including studies of local-density-of-states (LDOS) fluctuations, Landau-level formation, and Fermi edge singularities. The aim of this work is to study resonant tunnelling through a double impurity in a vertical double-barrier resonant tunnelling diode and to find some physical models to describe the behaviour of the system in magnetic field.

When conductance occurs via single-electron transport, fluctuations of the electron current are important to study. In this case we not only look at the average current through the system, but also noise. When we talk about noise we usually think of the ways to reduce it in any device applications. The importance of the physics of fluctuations stems from the fact that the ultimate accuracy of measurement of any physical quantity is limited by the fluctuations in this quantity, and the sensitivity of many devices is also limited by these fluctuations. Interest continues to grow in understanding the fundamental processes underlying different types of noise, in particular $1/f$ noise and shot noise. Some of such studies in a double-barrier resonant tunnelling diode and graphene transistor structures are presented in this thesis.

Recently, graphene, a new two-dimensional material has attracted much attention because of its unusual and counterintuitive properties not seen in the conventional two-dimensional systems. Graphene is a single atomic layer of graphite, successfully isolated from graphite only in 2004. This material previously existed only as a theoretical concept but has now become a hot research topic due to its possible electronic application. For instance, graphene is considered to be the successor of silicon in nanoelectronics because of its high room temperature carrier mobility. Also the charge carriers in graphene have a property called chirality, which is similar to spin and opens an interesting field for fundamental research. Little is currently known about the noise properties of graphene and it is one of the aims of this thesis to address this. The first study of $1/f$ noise in graphene is presented which reveals a new mechanism of noise in the Dirac region when both electrons and holes are present.

The First Chapter contains a brief introduction to the main concepts used to describe transport properties of conventional low-dimensional systems: transport in a two-dimensional electron gas, and resonant tunnelling through a quantum well. In this chapter noise as a useful tool to investigate properties of a conductive system not seen in conductance is introduced.

In the Second Chapter a description of the samples is given with a brief introduction describing the technology used in the sample preparation. The circuitry for current, conductance, and voltage noise measurements is discussed.

The rest of the thesis describes the experimental results. At the beginning of each experimental chapter an introduction to the theoretical results and experimental observations related to the topic of the chapter is presented. After this, the experimental and theoretical results of this work are given.

The Third Chapter is devoted to electron transport in a double-barrier resonant tunnelling diode. Experimental results on resonant tunnelling through two impurities are discussed and the main parameters of these impurities are derived using a model describing a diamagnetic shift of their energy levels.

The results of measurements of transport properties of chiral particles (electrons and holes with a linear dispersion relation) in ballistic graphene p-n junctions are given in Chapter Four. Preliminary results are also given on oscillatory behaviour of the resistance in p-n-p structures which can be a result of the Klein paradox and

wave interference of the chiral particles in graphene.

Chapter Five describes an experimental study of $1/f$ noise in graphene and multi-layer graphene where a dip in the (normalised) noise is observed in the Dirac point which shifts together with the Dirac point shift due to doping. The influence of the temperature on $1/f$ noise in graphene reveals that the dip in $1/f$ noise as a function of gate voltage can only be observed at high temperatures, but at low temperatures (0.26 K) there is no such a dip.

Finally, in the Conclusion all the main results obtained in this work are summarised and suggestions for further work are given.

Chapter 1

Basic concepts

1.1 Introduction

In this chapter the basic concepts behind the properties of low-dimensional systems used in this thesis are introduced.

The experimental part of this thesis is mainly devoted to graphene, a 2D layer of carbon atoms with unusual electronic properties, so the difference between conventional two-dimensional electron systems and graphene will be emphasised. The Boltzmann kinetic equation will be introduced which is a widely used description of the transport properties of two-dimensional systems. The Landauer-Büttiker formalism used in mesoscopic physics will also be introduced, which is important in small-sized systems.

An introduction to the physics of noise is given in the second part of this chapter. Four types of noise are discussed, together with the measurements which have to be done in order to distinguish them and to characterise the noise properties of the systems.

1.2 Low-dimensional systems

1.2.1 Two-dimensional electron gas

A two-dimensional electronic gas (2DEG) is an electronic gas in which particles can move freely only in two dimensions (2D), but in the third dimension are confined in a potential well. Restricted movement of the electrons can be achieved by

imposing a confining potential, for example, by electric field from a 'gate' in a field-effect transistor structure or by a specially constructed conduction band profile of GaAs/AlGaAs based heterostructure. The latter is called a modulation-doped field-effect transistor (MODFET) and is shown in Fig. 1.1. The 2DEG is formed near the interface GaAs/AlGaAs because the potential $\varepsilon_c(z)$ has a band-offset $\Delta\varepsilon_c \sim 0.3$ eV. The electrons in the 2DEG fill the energies from the ground state ε_0 to the chemical potential in the bulk μ_s and form (in the triangular well) a distribution of electron density proportional to the probability $|u_0(z)|^2$ (square of wave function for the ground state in the quantum well). In a Si-based metal-oxide field-effect transistor (Si-MOSFET) with SiO_2 as a dielectric layer the gate is used as one plate of the capacitor to which a voltage is applied to produce a finite concentration of carriers in the 2DEG, which plays the role of the second plate. The relation between the carrier concentration of the 2DEG, n, and the gate voltage, V_g, is well known:

$$n = \frac{\varepsilon_{ox}\varepsilon_{vac}}{d}(V_g - V_T), \tag{1.1}$$

where ε_{ox} is the dielectric constant of the oxide, ε_{vac} is the permittivity of free space, d is the distance from the gate to the 2DEG, and V_T is the threshold voltage at which the 2DEG is created under the oxide layer. In a MODFET with a quantum well the concentration can be nonzero at zero applied gate voltage (i.e. the 2DEG is already present), because electrons transfer from the doped layer to the well.

Because of the confinement, the movement of carriers perpendicular to the plane is quantised. At some position of the Fermi level only one subband can be occupied, Fig. 1.1, and the ground state of free carriers in the 2DEG is shifted up above the bottom of conduction band

$$\varepsilon = \varepsilon_0 + \frac{\hbar^2(k_x^2 + k_y^2)}{2m^*}, \tag{1.2}$$

where k_x and k_y are the components of the wavevector and ε_0 is the subband shift from the bottom of the conduction band. When the bottom of the first subband (ε_0) is taken as the reference energy, electrons in the 2DEG behave as free particle with effective mass m^* in two-dimensions resulting from the usual parabolic dispersion relation (last term in RHS of Eq. 1.2). The total carrier concentration depends on

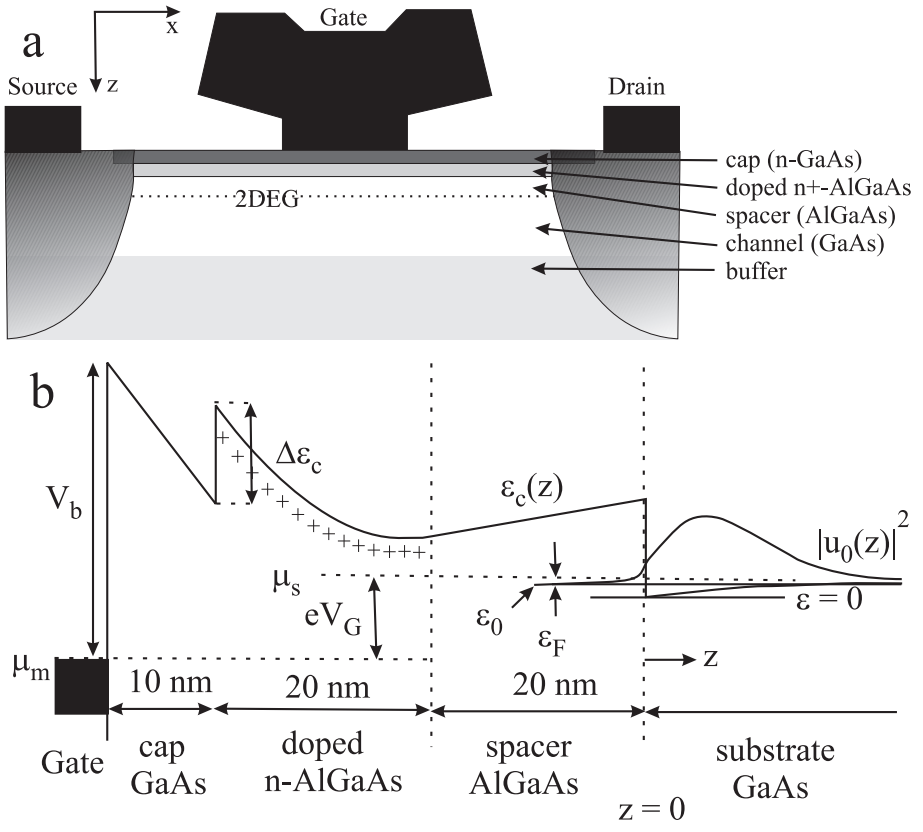

Figure 1.1: (a) Cross-section through a high-frequency GaAs-AlGaAs MODFET. (b) Self-consistent solution of the conduction band $\varepsilon_c(z)$ through modulation-doped layers with a positive gate bias $V_g = \mu_s - \mu_m = 0.2$ V (the difference between bulk and metal chemical potentials) and $n = 3\times10^{15}$ m^{-2} in the 2DEG. Adapted from [1].

the density of states, which, for the parabolic dispersion relation in 2D, Eq. 1.2, is:

$$\nu(\varepsilon) = g_s g_v \frac{m^*}{2\pi\hbar^2}, \tag{1.3}$$

where g_s and g_v are the spin and valley degeneracies, respectively. For GaAs, for example, $g_s = 2$ and $g_v = 1$. It can be seen that $\nu(\varepsilon)$ is independent of energy for 2D systems. To find the total concentration we have to integrate this density of states with the Fermi-Dirac distribution function (the probability for a particle to occupy a state at temperature T):

$$n(\varepsilon_F) = \int_0^\infty g_s g_v \frac{m^*}{2\pi\hbar^2} \left(1 + \exp\frac{\varepsilon - \varepsilon_F}{k_B T}\right)^{-1} d\varepsilon, \tag{1.4}$$

where ε_F is the Fermi energy, and k_B is the Boltzmann constant. At low temperatures where the electron gas can be considered as a degenerate Fermi gas

($k_BT << \varepsilon_F$) the Fermi-dirac distribution becomes a step function and Eq. 1.4 can be simplified to get a linear dependence of the concentration on the Fermi energy: $n(\varepsilon_F) = g_s g_v m^* \varepsilon_F / 2\pi\hbar^2$. If the Fermi energy is equal to zero the concentration at a finite temperature will not be equal to zero: $n(0) = \ln 2 g_s g_v m^* k_B T / 2\pi\hbar^2$.

1.2.2 The Boltzmann equation

Transport properties of electrons in a diffusive 2DEG with applied electric or magnetic fields can be described by a Boltzmann equation, which describes the evolution of a nonequilibrium distribution function, $f(\mathbf{k}, \mathbf{r}, t)$ in a 5-dimensional phase space, where $\mathbf{k} = (k_x, k_y)$ is the 2D wavevector, $\mathbf{r} = (x, y)$ is the coordinate vector, and t is time. The nonequilibrium distribution function gives the probability to find a particle with wavevector $\mathbf{k}$ in a unit volume near the point $\mathbf{r}$ at time t. This function describes the statistical properties of the system when it can not be described by the Fermi-Dirac distribution function, which works only at thermodynamical equilibrium. An electric field, $\mathbf{E}_0$, and external magnetic field, $\mathbf{B}$, both move the electron gas away from equilibrium. The differential equation for the nonequilibrium distribution function is written as [2]

$$\frac{\partial f}{\partial t} + \mathbf{v}(\mathbf{k}) \cdot \nabla_{\mathbf{r}} f - \frac{e}{\hbar} \left(\mathbf{E}_0 + [\mathbf{v}(\mathbf{k}) \times \mathbf{B}] \right) \cdot \nabla_{\mathbf{k}} f = \left(\frac{\partial f}{\partial t} \right)_{scat}, \tag{1.5}$$

where $\mathbf{v}$ is the velocity of the electron, $\nabla_{\mathbf{r}} = (\partial/\partial x, \partial/\partial y)$ and $\nabla_{\mathbf{k}} = (\partial/\partial k_x, \partial/\partial k_y)$. The term $(\partial f/\partial t)_{scat}$ is called the collision integral which describes how the distribution function changes under the influence of scattering processes by, for example, Coulomb impurities, phonons. There is no general solution of Eq. 1.5, but an analytical solution is possible to obtain in certain cases, if some simplifications are used. In the linear regime of conduction the current does not affect the conductivity of the 2DEG. In this regime one can assume that deviation from the equilibrium state is weak and we need to find a small correction, $f_1(\mathbf{k}, \mathbf{r}, t) = f(\mathbf{k}, \mathbf{r}, t) - f_0(\mathbf{k}, \mathbf{r}, t)$, from the equilibrium Fermi-Dirac distribution function, f_0. In the absence of magnetic field the stationary kinetic equation is written as [2]

$$\mathbf{v}(\mathbf{k}) \cdot \nabla_{\mathbf{r}} f - \frac{e}{\hbar} \mathbf{E}_0 \cdot \nabla_{\mathbf{k}} f = - \left(\frac{f - f_0}{\tau(\mathbf{k})} \right), \tag{1.6}$$

where the collision integral is written in a different form, using $\tau(\mathbf{k})$, which is called the momentum relaxation time. This time describes how fast the system returns to the equilibrium state if all external forces are switched off. If we take into account only scattering processes where the energy of the particle is conserved (elastic scattering), then the relaxation time can be written as [2]

$$\frac{1}{\tau(\mathbf{k})} = \sum_{\mathbf{k}'} W(\mathbf{k}, \mathbf{k}') \left(1 - \frac{\mathbf{k} \cdot \mathbf{k}'}{|\mathbf{k}|^2}\right), \tag{1.7}$$

where $W(\mathbf{k}, \mathbf{k}')$ is the probability per-unit-time for an electron to be scattered from the state with a wavevector $\mathbf{k}$ to a new one with wavevector $\mathbf{k}'$, and $(1 - (\mathbf{k} \cdot \mathbf{k}')/|\mathbf{k}|^2) = 1 - \cos\theta$, where θ is the angle between the two wavevectors. This quantity has to be calculated separately, usually using quantum mechanics. If there are two independent scattering mechanisms in the system with relaxation times $\tau_1(\mathbf{k})$ and $\tau_2(\mathbf{k})$, then the total relaxation time is

$$\tau(\mathbf{k}) = \left(\tau_1(\mathbf{k})^{-1} + \tau_2(\mathbf{k})^{-1}\right)^{-1}. \tag{1.8}$$

Eq. 1.6 can be solved if we assume that $\tau(\mathbf{k})$ is independent of the electric field (there is no overheating of the electron gas by the current) and there is no temperature gradient in the system. The solution is given by

$$f(\mathbf{k}) = f_0(\mathbf{k}) + \frac{\tau(\mathbf{k})}{\hbar} e E_0 \left(\frac{\partial f_0(\mathbf{k})}{\partial \mathbf{k}}\right). \tag{1.9}$$

This solution is used to obtain the current density through the system:

$$\mathbf{j} = -\frac{2e}{(2\pi)^2} \int \mathbf{v}(\mathbf{k}) f(\mathbf{k}) d\mathbf{k} = \frac{e^2}{2\pi^2} \int \tau(\mathbf{k}) \mathbf{v}(\mathbf{k}) (\mathbf{v}(\mathbf{k}) \cdot \mathbf{E}_0) \left(\frac{\partial f_0(\mathbf{k})}{\partial \mathbf{k}}\right) d\mathbf{k}. \tag{1.10}$$

Because the kinetic equation (Eq. 1.6) is semiclassical there are several limitations as to where it can be used. The electron wavelength, λ must vary slowly. This condition is written as $\lambda|\mathbf{F}| = \lambda|e\mathbf{E}_0| \ll \bar{\varepsilon}$, which means that the energy gained due to force $\mathbf{F}$ over distance λ has to be much smaller than average electron energy, $\bar{\varepsilon}$. There is also a limitation for the strength of magnetic field: for a nondegenerate electron gas ($k_B T \gg \varepsilon_F$) this is $\hbar\omega_c \ll k_B T$, and for degenerate one ($k_B T \ll \varepsilon_F$) it is $\hbar\omega_c \ll \varepsilon_F$, where $\omega_c = eB/m^*$ is the cyclotron frequency. Finally, there is a

condition for the relaxation time: $l = |\mathbf{v}_F|\tau \gg \lambda$, which states that the mean free path, l, has to be much larger than the wavelength ($\mathbf{v}_F$ is the Fermi velocity).

The coefficient of proportionality (in general it is a tensor) between the current density and electric field ($\mathbf{j} = \sigma\mathbf{E}_0$) is called the conductivity and can be written as

$$\sigma = e^2 n\tau/m^*, \tag{1.11}$$

where τ is the momentum relaxation time which in a degenerate system depends on the Fermi energy. We can introduce the mobility, μ, which describes how easily electrons are affected by an electric field:

$$\mu = v_d/|\mathbf{E}_0| = e\tau/m^*, \tag{1.12}$$

where v_d is the drift velocity, which shows an average directional drift of the carries under an influence of the electric field. The mobility is directly related to the relaxation time.

1.2.3 Landauer-Büttiker approach

We now discuss how the resistance of a narrow two-terminal sample with a 2DEG can be calculated [3]. We consider a two-terminal sample, shown in Fig. 1.2 with a bias voltage, V, applied at 0 K. The Fermi level in the left contact is higher by eV than in the right contact. This creates a noncompensated current flow from the left to the right contact. If the width W of the sample is small, the movement of electrons perpendicular to the current is quantised into several modes M. (In the x-direction the electron is a plane wave but in y-direction there are M-modes described by standing waves, so that there is no current flow in the y-direction.) The grey region in Fig. 1.2 is an impurity or disorder potential. We know about this region only by the probability of a carrier to transmit through it, T, from the left to the right contact. In our picture it is the only source of scattering in the system; the contacts and leads are ideal. The current from the left contact to the sample, if a voltage $V = (\mu_1 - \mu_2)/e$ is applied, [3]

$$I_1^+ = (2e/h)M(\mu_1 - \mu_2), \tag{1.13}$$

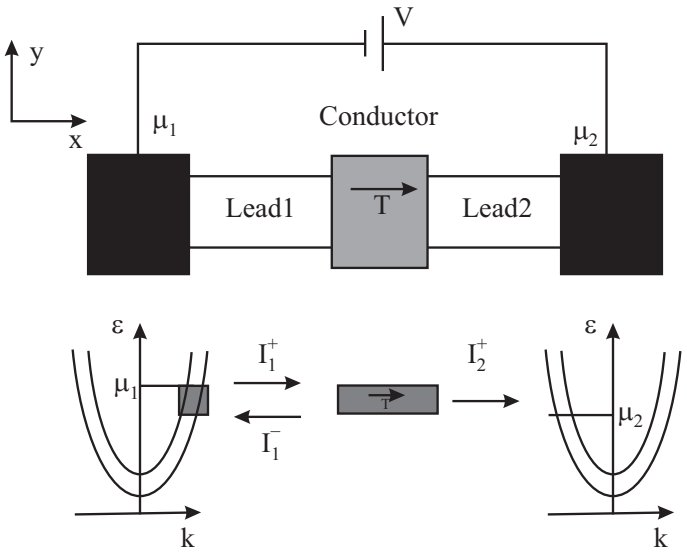

Figure 1.2: Top: A conductor with transmission probability T connected to two large contacts through two leads. Bottom: subbands in the leads with Fermi levels μ_1 and μ_2. "Zero" temperature is assumed such that the energy distribution of the incident electrons in the two leads can be assumed to be step function. Note that $k = k_x$. Adapted from [3].

as it can be shown that each mode carries the same current. Here the factor of 2 accounts for the spin degeneracy of the electrons. (We assume that the transmission for each mode is the same.) This is not the total current in the left lead. There is also the current which reflects with probability $R = 1 - T$ from the scatterer: $I_1^- = (2e/h)MR(\mu_1 - \mu_2)$. These two currents produce the total current through the sample:

$$I = I_1^+ - I_1^- = (2e/h)MT(\mu_1 - \mu_2). \tag{1.14}$$

We can introduce the conductance as

$$G = \frac{I}{V} = \frac{I}{(\mu_1 - \mu_2)/e} = \frac{2e^2}{h}MT. \tag{1.15}$$

If the transmission depends upon the mode number, a simple product MT must be replaced by a sum over all modes

$$G = \frac{2e^2}{h}\sum_{i=1}^{M} T_i, \tag{1.16}$$

where T_i is the transmission of the i^{th} propagating mode. When the transmission is perfect for each mode $T = 1$, as in a ballistic device then the conductance has a

finite universal value $2Me^2/h$.

1.2.4 Quantum dots and shallow donors in GaAs

If an electron is confined in a small box, then a discreet energy spectrum is formed. Such a box is called a quantum dot (QD). In QDs quantum effects are more significant than in 2DEGs, because no classical approach can be applied to a system with a fully discreet energy spectrum. One can estimate the ground state energy of a QD from the uncertainty principle, $\Delta x \Delta p_x \geq \hbar/2$, as

$$\varepsilon_{dot} \sim \frac{3\hbar^2}{8m^* d^2}, \tag{1.17}$$

where $d \sim \Delta x$ is a characteristic size of the QD, m^* is the effective mass of the electron. A parabolic potential is usually a good approximation for the confining potential for the electrons in QD.

Zero-dimensional states can not only be created artificially using a QD but they can naturally be present in the system because semiconductors are never pure materials. Impurities or defects in crystal lattice are common in GaAs structures. If an alien atom replaces an atom in the GaAs crystal, then it is called a substitutional defect, which can be a donor or acceptor. The energy levels of these impurities are shallow and the charged-impurity potential can be described by an effective Coulomb potential which takes into account the dielectric constant, ε_r, of the crystal and the effective mass of an electron or hole, m^*. The quantitative model for such impurities is a modified hydrogen atom model and the energy spectrum of these impurities is given by

$$\varepsilon_l = -\frac{m^* e^4}{8h^2 \varepsilon_r^2 \epsilon_{vac}^2} \frac{1}{s^2}, \tag{1.18}$$

where ϵ_{vac} is the vacuum permittivity, and s is the number of the level. The energy in Eq. 1.18 is calculated from the bottom of the conduction band. The ground state has $s = 1$. This binding energy of a shallow donor in GaAs is ~ 10 meV and is three orders of magnitude smaller than the Rydberg energy (13.6 eV). This energy also has the meaning of the ionisation energy, because when an electron gains this energy it will move freely in the conduction band.

In a quantum well the bottom of the conduction band is shifted up by the value

of the energy of the ground state in the well. In the limit of an infinitely narrow quantum well an impurity placed in it becomes effectively two-dimensional and the energy spectrum of the impurity has energy levels that are deeper by a factor of 4 [4].

If the impurity is placed exactly on the edge of an infinite potential barrier then, due to symmetry considerations, its energy spectrum will change in such a way that only odd states survive, namely the new ground state is formed from the first exited state of the initial symmetric potential without the infinite potential barrier.

1.2.5 Semimetals

Semimetals are chemical compounds with electronic properties in between metals and dielectrics. The most known semimetals are bismuth, tin, and graphite (an allotrope of carbon). Semimetals, unlike semiconductors have finite electrical conductivity at absolute zero. The change in their conductivity with temperature is distinct from that of a metal. The characteristic feature of semimetals is a small overlap between the valence and the conductance bands with a carrier concentration of $10^{18} - 10^{20}$ cm^{-3}, or 10^{-3} per atom. This means that there are accessible states at zero temperature for electrons to scatter to and also that increase in the number of free carriers with increasing temperature is small. Charge carriers in semimetals have larger mobility than in metals and low effective mass. Due to small overlap of the bands it is easy to change it by applying, for example, a magnetic field, which can trigger a semimetal-dielectric transition by the formation of an indirect band gap.

1.2.6 p-n junctions

When two pieces of silicon doped with acceptors (p) and with donors (n) are connected, electrons transfer between them in such a way that the Fermi energy will be constant through the whole system. At the junction between the pieces a region of the order of the screening length without charges in it is formed that creates a barrier ($e\phi_c$) to charge flow. This diode has a strongly nonlinear I-V characteristic. Usually diodes work in the regime when a positive potential applied to the n part of the structure produces exponential growth of the current. Here we are interested

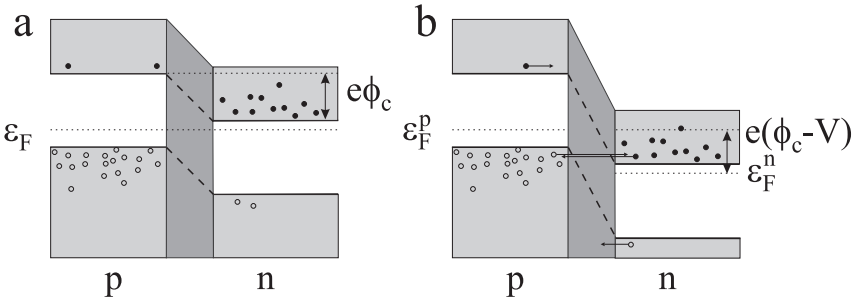

Figure 1.3: (a) p-n diode structure at zero bias. The Fermi level has the same value in the p and n regions of the structure. (b) p-n diode structure at a negative bias applied to produce a tunnel current of holes from the p to n region and current of electrons from the n to p region.

in the opposite regime when a sufficient negative voltage (required to align the top of the valence band of the p-region with the bottom of the conduction band of the n-region) applied to the n-region produces a tunnelling current from the p-region to the n-region, as shown in Fig. 1.3.

1.2.7 Resonant tunnelling diode

A GaAs resonant tunnelling diode (RTD) is based on a GaAs quantum well separated from the contacts by two AlGaAs barriers. The quantum well states are the subbands in the narrow GaAs layer. In Fig. 1.4 the I-V characteristic of a double-barrier RTD is illustrated. When a subband has energy ε_s is larger than the Fermi level in the left contact (at small biases) there is no current flow, Fig. 1.4(a). If a larger bias is applied, ε_s drops below this Fermi level and the current increases, Fig. 1.4(b). It reaches a maximum value when the resonant level is aligned with the bottom of the conduction band in the left contact, Fig. 1.4(c). The current becomes small again if the bias is increased further, because less number of electrons can tunnel when the energy and the lateral components of the wavevectors have to be conserved.

The current in 3D has to be integrated not only over different energies of the electrons, but also over the direction of tunnelling. The total current is given by [1]

$$I = 2e \int \frac{d\mathbf{k}}{(2\pi)^2} \int_0^\infty \frac{dk_z}{2\pi} f_0(\varepsilon(\mathbf{K}, \mu_L)) v_z(\mathbf{K}) T(k_z), \tag{1.19}$$

where $\mathbf{K}$ is the 3D wavevector, $\mathbf{k}$ is the 2D wavevector in the direction perpendicular

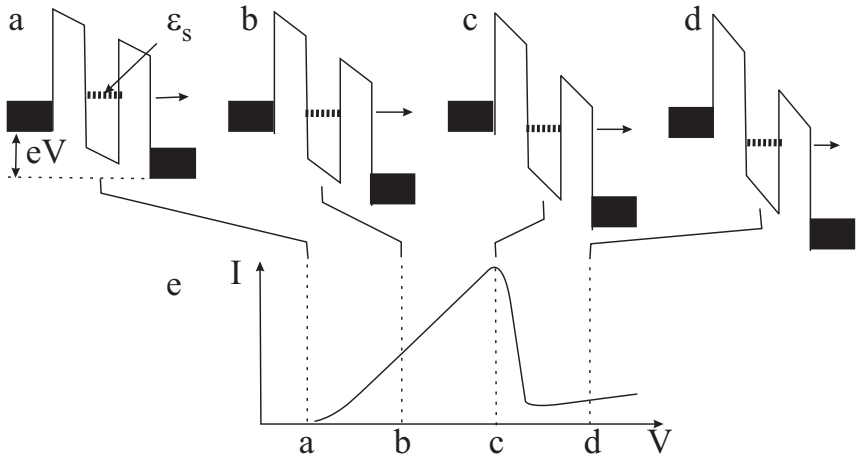

Figure 1.4: Profile of a resonant-tunnelling diode at different bias voltages V. The bias increases from (a) to (d), giving rise to the I-V characteristic shown in (e). The shaded areas on the left and right are the Fermi seas in the contacts. Adapted from [1].

to the current, v_z is the projection of the electron velocity on the z-direction (where current flows), μ_L is the Fermi level in the left contact, and $T(k_z)$ is the energy-dependent transmission coefficient. We can rewrite this current in a much simpler way when the integration over $\mathbf{k}$ is made:

$$I = \frac{e}{h}\frac{m^*}{\pi\hbar^2}\int_{U_L}^{\mu_L}(\mu_L - \varepsilon)T(\varepsilon)d\varepsilon, \tag{1.20}$$

where U_L is the potential of the conduction band bottom of the left contact, and $\varepsilon = U_L + \hbar^2 k_z^2/2m^*$ is the "longitudinal component" of the total energy. (Zero temperature is assumed.)

For resonant tunnelling, the transmission can be approximated by the Breit-Wigner formula [1] $T(\varepsilon) \sim T_0(1 + (\varepsilon - \varepsilon_s)/(\Gamma/2))^{-1}$, where Γ is the full width at half-maximum which stems from the fact that there is no bound state in the well but electrons can tunnel to the contacts, and T_0 is the maximum transmission observed in the resonance. If we substitute this expression in Eq. 1.20 we obtain

$$I = \frac{e}{h}\frac{m^*}{\pi\hbar^2}(\mu_L - \varepsilon_s)\frac{\pi}{2}\Gamma T_0, \tag{1.21}$$

where $\varepsilon_s = \varepsilon_s^0 - \beta_s e V_{sd}$, where ε_s^0 is the subband energy without voltage applied, and β_s is the coefficient between energy and voltage, which depends on V_{sd} and the position of the state between the contacts. The last expression explains the shape

in Fig. 1.4(e). The current grows as the subband level is shifted down in energy with increasing voltage until U_L is reached when current stops flowing.

1.3 Basics of noise

1.3.1 General noise characteristics

When one measures the resistance by the voltage drop along a resistor for a fixed current, the voltage is not constant in time but fluctuates in a random way.

Consider a signal which fluctuates as a function of time, $V(t)$, Fig. 1.5(a). If we specify a period Δt the set of measurements will be seen as a set of values of $\{V_i\}$ measured at specific moments t_i with frequency $1/\Delta t$. To find the real average resistance of the sample the averaged value, $\overline{V}$, over several measurements, N, are taken:

$$\overline{V} = \frac{1}{N}\sum_{i=1}^{N} V_i. \tag{1.22}$$

If only the average resistance needs to be known then the average in Eq. 1.22 is enough; but is there any useful information in the set $\{V_i\}$? Theoretical and experimental study of noise tell us that the answer is "yes". Moreover the noise gives information which is difficult or impossible to determine from the resistance, such as the concentration of defects, interaction of carriers, and correlations in electron transport [5, 6]. The noise theory helps to find a way to characterise noise and analyse its properties, and to remove it if required.

Eq. 1.22 can be rewritten in terms of a probability distribution function. This distribution function is simply a histogram where the set of voltage values are distributed into bins of size ΔV. The probability for a value to be in the range $V_j \pm \Delta V/2$ is $p_j = N_j/N$ where N_j is the number of values in the bin and N is the total number of values ($\sum p_j = 1$). The distribution of the considered signal is shown in Fig. 1.5(c). For M bins we can rewrite Eq. 1.22 as

$$\overline{V} = \sum_{j=1}^{M} V_j p_j. \tag{1.23}$$

This expression is also called the first moment of the distribution, and the set of probabilities $\{p_j\} = \{f(V_j)\}$ can be called a discreet probability function. From this

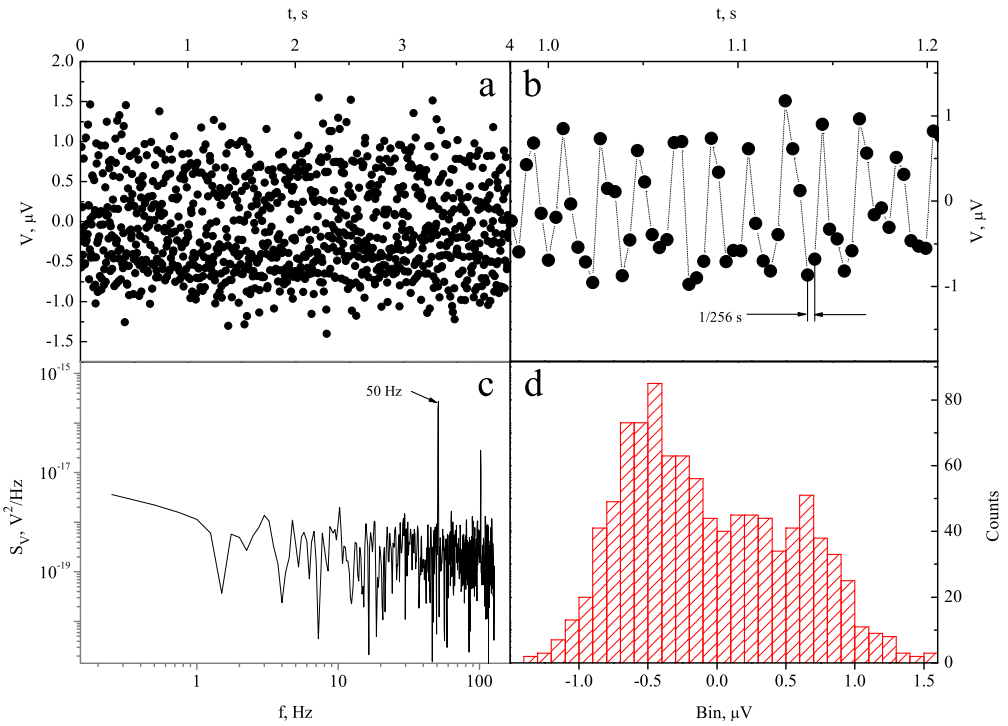

Figure 1.5: (a) A random variable V as a function of time (1024 points are shown). (b) Zoom-in of the time domain signal shown in (a). (c) Spectral density, S_V, on a log-log scale as a function of frequency. The largest spikes correspond to 50 Hz harmonics. (d) Distribution of the values in the signal presented in (a) into bins.

we can introduce a useful relation for the average of a general function $g(V_j)$ as

$$\overline{g(V)} = \sum_{j=1}^{M} g(V_j) p_j. \tag{1.24}$$

Another characteristic of a random signal is how far it deviates from its average value, the variance (the second central moment):

$$\operatorname{var} V = \overline{V^2} - (\overline{V})^2. \tag{1.25}$$

The time domain signal contain all possible information about the noise. But usually noise is studied in the frequency domain where a real signal is interpreted as the sum of many harmonics in some frequency range. Fourier analysis is the most powerful method for noise analysis. The time domain signal is approximated by a

Fourier series sum

$$V(j\Delta t) = \sum_{n=-T_V/\Delta t}^{T_V/\Delta t} a_n \exp\left(i2\pi f_n j\Delta t\right). \tag{1.26}$$

where T_V is the time of measurements, $f_n = n/T_V$ is the frequency, and Fourier coefficients

$$a_n = \frac{\Delta t}{T_V} \sum_j V_j \exp\left(i2\pi f_n j\Delta t\right). \tag{1.27}$$

Another characteristic of noise can be introduced, called the spectral density, Fig. 1.5(c), by [5]

$$S_V(f) = \lim_{T_V\to\infty} 2T_V \overline{a_n a_n^*}, \tag{1.28}$$

where the asterisk denotes the complex conjugation of the coefficient. $S_V(f)$ describes the square of the amplitude of the signal in the range of frequencies with a bandwidth of Δf centered around f divided by Δf. One can distinguish between different types of noise by studying the dependence of S_V on the frequency. For example, thermal noise has a flat spectrum where the spectral density is independent of frequency, and $1/f$ noise has spectral density inversely proportional to frequency. These types of noise are described below.

In some cases it is more mathematically convenient to work with continuous signals, $V(t)$, where all discreet sums should be replaced by integrals. We can say that noise is characterised by [6]

$$S_V(f) = 2\psi_V(\omega) = 2\int_{-\infty}^{+\infty} e^{i\omega(t_1-t_2)}\psi_V(t_1-t_2)d(t_1-t_2), \tag{1.29}$$

where $\psi_V(\tau)$ is the correlation function, t_1-t_2 is the difference between two moments in time. Thus the spectral power is directly related to the correlation function, which can be determined by averaging of the product of two functions δV over a long time period:

$$\psi_V(t_1-t_2) = \psi_V(t_1,t_2) = \lim_{T_V\to\infty} \frac{1}{T_V}\int_{-T_V/2}^{+T_V/2} \delta V(t_1+t)\delta V(t_2+t)dt. \tag{1.30}$$

where $\delta V(t) = V(t) - \overline{V(t)}$.

We have discussed fluctuations of voltage only, but in general current and resis-

tance can also fluctuate. These fluctuations lead to the four most common types of noise. The first type is thermal noise of a resistor which appears at nonzero temperatures [5]. The others are nonequilibrium types of noise, which appear when a bias is applied to the resistor. These types of noise include random telegraph noise (RTN), $1/f$ noise or flicker noise, and shot noise.

1.3.2 Thermal noise

The noise generated by thermal agitation of electrons in a resistor is called thermal or Nyquist-Johnson noise. The spectral density of the current for this type of noise is independent of frequency:

$$S_I = 4k_B T G, \tag{1.31}$$

where k_B is Boltzmann's constant, T is the temperature of the resistor and G is the conductance of the resistor. Eq. 1.31 can be converted to voltage by substitution $S_V = S_I R^2$. Thermal noise can be used as a thermometer, because it is generic for all resistors. The only parameter that is required is the resistance of the sample which is usually easy to measure. In general thermal noise is the lowest possible noise in any device as it cannot be suppressed.

1.3.3 Random telegraph noise

Random telegraph noise (RTN) or burst noise can be described by a random switch model [5]. The power spectrum $S_u(\omega)$ has the shape of a Lorentzian function:

$$S_u(\omega) = (u_1 - u_2)^2 p_1 p_2 \frac{4\tau}{1 + \omega^2 \tau^2}. \tag{1.32}$$

where the variable u describes a two-level system and changes between the values u_1 (high energy state) and u_2 (low energy state), p_1 is the probability to find the value u_1, $p_2 = 1 - p_1$ is the probability to find the value u_2, respectively, and τ is the "relaxation time" (the average time spent in each state before making a transition to another state, or the inverse of the total rate of the transition, backward and forward, in the process). One of the reasons that RTN occurs is the process of charging and discharging of impurities in an oxide or dielectric close to the conducting channel. Usually RTN is an undesirable effect in measurements and applications where stable

behaviour of devices is required.

1.3.4 $1/f$ noise or flicker noise

When a constant voltage is applied to a resistor the current will exhibit fluctuations. The spectral density of these fluctuation is frequency dependent. It is proportional to $1/f^{\alpha}$ where α is close to unity. This kind of noise is often called flicker noise or 'one over f' noise. Analysis of these fluctuation has revealed that they come from fluctuations of the sample resistance [7, 8].

Fluctuations with $1/f$ spectra have been observed in a wide variety of physical systems. Its exact physical origins are still unclear in most systems and the dispute over the origin of $1/f$ noise is still unresolved [9]. Usually for similar systems there is a specific mechanism which produces $1/f$ noise [10]. There are several models to describe $1/f$ noise in solids, which are based on the carrier number fluctuations [11] and mobility fluctuations [12].

Several models of $1/f$ noise emerge by using the superposition of Lorentzian spectra with widely distributed relaxation times. A random process with characteristic time has a Debye-Lorentzian spectrum [13] (cf. Eq. 1.32):

$$S(\omega) \propto \frac{\tau}{1+\omega^2\tau^2}. \tag{1.33}$$

The resulting spectrum may be generated by postulating an appropriate distribution $D(\tau)$ of the characteristic times within the sample. Then

$$S(\omega) \propto \int \frac{\tau}{1+\omega^2\tau^2} D(\tau) d\tau. \tag{1.34}$$

In particular, if $D(\tau) \propto \tau^{-1}$ for $\tau_1 < \tau < \tau_2$ then

$$S(\omega) \propto \omega^{-1} \quad \text{for} \quad \tau_2^{-1} \ll \omega \ll \tau_1^{-1}. \tag{1.35}$$

It was shown that $1/f$ noise in metals is produced by the movement of defects or impurities [6]. Defects in these experiments were generated by radiation damage from an electron beam. The noise was related to the mobile defects only, as was shown by annealing experiments where noise reduced significantly (by two orders of

magnitude as these defects were decreased). Nevertheless the type of these defects still remains unknown [6].

1.3.5 Shot noise

Shot noise is the result of random fluctuations of the electric current in a conductor. These fluctuations are caused by the fact that the current is carried by discrete charges. In the case of totally uncorrelated current, when the events of arriving of electrons are independent of each other, shot noise has the so-called full Poissonian behaviour, with noise power S_I which depends linearly on the current: $S_I = 2eI$. The transition of the noise from thermal noise (at zero current) to shot noise at nonzero temperature for a sample with N propagating modes is described by [14]

$$S_I = 2\frac{e^2}{2\pi\hbar}\sum_{n=1}^{N}[2k_BTT_n^2 + T_n(1-T_n)eV\coth(eV/2k_BT)], \tag{1.36}$$

where T is the temperature, and T_n is a transmission coefficient of the n^{th} channel. The prefactor of 2 is due to spin degeneracy. In the linear regime when the applied voltage is small compared to the temperature T, ($eV << k_BT$) one can observe thermal noise with conductance given by Eq. 1.16.

When a source of negative correlation is introduced, for example, due to the Pauli-exclusion principle an electron can not go through the system because of the Coulomb repulsion, the noise amplitude was shown to be reduced. For a resonant tunnelling (RT) through a double-barrier structure this is attributed to the finite dwell time of the resonant state [15]. Theoretical models for purely coherent transport and for sequential tunnelling have been developed for this suppression. This suppression of the shot noise was also observed for resonant tunnelling in zero-dimensional systems. To characterise the relative amplitude of shot noise, the dimensionless Fano factor, F is used, being defined as $F = S/2eI$. In metallic diffusive system independent on shape and concentration $S_I = 2eFI$, with Fano factor F equal to 1/3 [15].

An enhancement of shot noise (in this case the Fano factor is larger than 1) in the case of RT via localized states have been observed in [16]. This enhancement originates from Coulomb interaction between two localized states which imposes

correlations between electron transfers.

Chapter 2

Samples and experimental techniques

2.1 Introduction

The aim of this chapter is to describe the samples used and to show how resistance, current, and noise have been measured.

In the first part of this chapter the structure of the vertical double-barrier resonant tunnelling diode (DBRTD; chapter 3) and an introduction to the method of its fabrication is given. The geometry of the graphene samples (chapter 4 and chapter 5) is given and the basic characteristics such as the resistivity $\rho(V_g)$ and the position of the Dirac point are described.

The second part of this chapter is devoted to the circuitry used to measure small resonant currents in DBRTDs and noise measurements in graphene (chapter 5). The ^{3}He cryostat used to control the temperature and magnetic field in many of experiments in this thesis is also briefly described.

2.2 Samples

2.2.1 Double barrier resonant tunnelling diode

In chapter 3 the results of the study of resonant tunnelling through a double impurity in a DBRTD are presented. The study was performed on a single sample entitled K110Re23b supplied by Giancarlo Faini from the Laboratoire de Photonique

Component Layer	Material	Doping level (Si)	Thickness (nm)
Source	GaAs	$2 \times 10^{17} cm^{-3}$	200
Spacer Layer	GaAs	0	30
Bottom Barrier	$Al_{0.33}Ga_{0.67}As$	0	8.7
Quantum Well	GaAs	0	5.1
Top Barrier	$Al_{0.33}Ga_{0.67}As$	0	8.7
Spacer Layer	GaAs	0	20
Drain	GaAs	$2 \times 10^{17} cm^{-3}$	200
Top	GaAs	$1 \times 10^{18} cm^{-3}$	500

Table 2.1: The profile of heterostructure M240 (with doping levels and thicknesses) on which K110Re23b sample is based.

et Nanostructures, CNRS in Marcoussis, France. This sample was fabricated by molecular beam epitaxy (MBE) on a GaAs substrate and its profile is given in Table 2.1. A GaAs quantum well of 5.1 nm width is grown between two barriers (8.7 nm of $Al_{0.33}Ga_{0.67}As$) with a band gap offset of 0.3 eV. There are two undoped GaAs spacers of 30 nm and 20 nm between the Si-doped (about 2×10^{17} cm^{-3}) source and drain contacts, respectively. To confine the current carriers in two lateral dimensions a plasma etching was used. Ni was deposited on top of the structure to serve as a mask for high energy (50 keV) Ga ions. A cylindrical pillar of 70 nm diameter was formed. Then the Ni layer was removed to re-grow a GaAs top electrode. (A polyimide layer was deposited between the pillar and the rest of the structure to make the structure more rigid.) Finally a top Au-Ni-Ge contact of several micron lateral size was deposited and annealed. The sample was electrically bonded in a ceramic package. A more detailed explanation of the fabrication procedure is given in [17].

Without applied source-drain voltage (V_{sd}) the bottom of the conduction band in the quantum well lies above the Fermi level. If a sufficiently high V_{sd} voltage is applied (when the first subband level in the quantum well aligns with the Fermi level in the source) the current can flow from the source to drain via resonant tunnelling, Sec 1.2.7. The estimated energy of the first subband is 100 meV with respect to the bottom of the conduction band (from 1D model with finite potential barriers).

Fig. 2.1 shows an example of a self-consistent 1D model of the conduction band profile of the structure at 67 mV applied between source and drain (the temperature is 1 K). The calculations are performed by means of the heterostructure

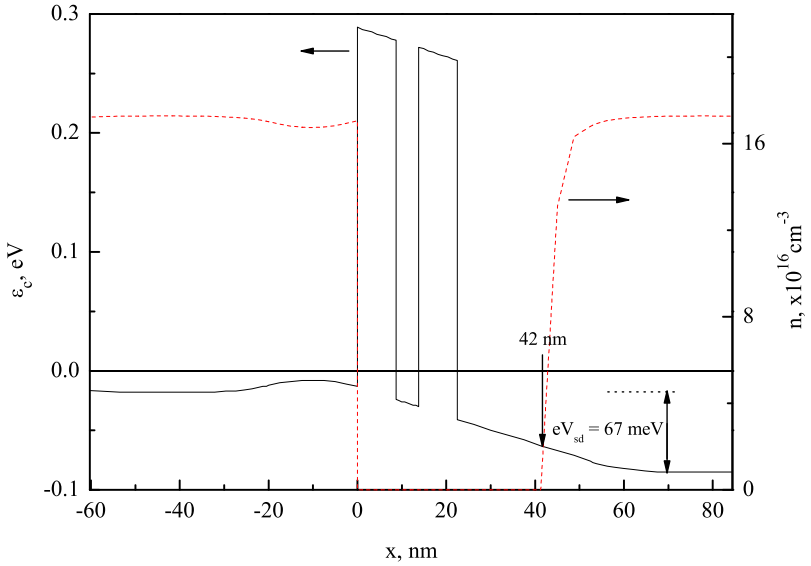

Figure 2.1: The calculated conduction band profile, ε_c, of the DBRTD structure with $V_{sd} = 67$ mV. The dashed line is the electron concentration as a function of x-coordinate. The Fermi level is at zero energy.

modelling program HETMOD using the nominal doping level and composition of the heterostructure from Table 2.1. It can be seen that the left part of the structure (before the barrier) is filled with an electron gas and the bottom of the conduction band is equal to -13 meV. On the other side of the structure a depletion region is formed. The total length of the structure between contacts with high electron concentration is 42 nm at $V_{sd} = 67$ mV. If V_{sd} is increased the length of the depletion region will also increase.

2.2.2 Graphene samples for noise measurements

In this thesis six graphene and one multilayer graphene sample have been used. These samples were fabricated by Roman Gorbachev from the laboratory of Quantum Transport in Nanostructures at Exeter University. All of them were produced by a mechanical exfoliation technique [18]. Highly ordered pyrolytic graphite for samples ML2 and SL4 or natural graphite for sample SL6 (formed from a stack of graphene flakes) is split by means of adhesive tape into several thinner flakes. These flakes are deposited on a Si/SiO_2 substrate. Among them are flakes of single-

	ML2	SL4	SL6
Length, μm	4.29	3.5	22.5
Width, μm	0.6	1.5	1.5
ρ_D, kOhm	1.4	1.7	3.5
V_D, V	0 V or 15 V	0	3.3 V

Table 2.2: Characteristic of graphene samples for noise measurements.

atom thickness which can be identified optically. (The interference of light from the 300 nm SiO_2 layer creates a contrast difference between single-layer and multi-layer flakes.) As soon as the flakes are found, standard electron beam lithography is used to define electric contacts to the flake (the contact material is Cr/Au). The technology is more elaborate for the samples with top-gates and will be explained below.

Three samples for noise measurements have been studied. The two samples, SL4 and SL6, are single-layer graphene. This was proved by means of quantum Hall effect measurements. Sample SL6 has length 22.5 μm and the highest mobility away from the Dirac point ($\sim$ 20000 $\mathrm{cm^2V^{-1}s^{-1}}$). The third sample, ML2, is multilayer graphene of more than 2 layers thickness (established using optical contrast). The geometrical sizes (the samples have approximately rectangular shape) are presented in Table 2.2. In this table the resistivity in the Dirac point, ρ_D, and the position of the Dirac point in the gate voltage are shown.

The two single-layer samples for noise measurements have the width which is larger than 1 μm and therefore have practically zero bandgap. If the width of the flake is small, then the edges make a significant contribution to the band structure, forming a band gap of size increasing approximately linearly as a function of inverse width [19]. Such narrow graphene stripes are called nanoribbons. It was shown that the band gap of 20 nm width graphene nanoribbon is approximately 26 meV [20]. Thus if we take a stripe with 1.5 μm width, the band gap will be 75 times smaller than 26 meV ($\sim$ 0.35 meV corresponds to 4 K).

Fig. 2.2(a) shows a SEM image of sample SL4. The electrical contacts are shown as outlines in the figure. Fig. 2.2(b) shows the resistivity of the sample as a function of gate voltage at $T = 0.25$ K, where the characteristic peak in the Dirac point (0 V) can be clearly seen. In the inset one can see the first quantum Hall plateau in $G_{xy}(\nu)$, which is observed at $2e^2/h$ in agreement with experiment [21, 22] and

theory [23] for single layer graphene.

Sample SL6 has six terminals with the distance between two Hall contacts of about 0.5 μm, and the area of the sample under the potential contact is about $\sim 0.5 \times 0.5\,\mu\mathrm{m}^2$. The distance from the potential contacts to the nearest current contact is about 1 μm.

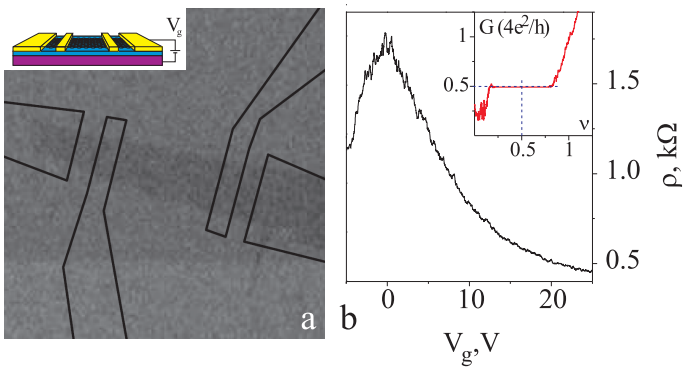

Figure 2.2: (a) SEM image of sample SL4, where the positions of the contacts are shown as outlines. The inset shows a diagram of a graphene sample on n^+Si substrate (purple), covered by 300 nm SiO_2 (blue) and contacted by Au/Cr (yellow). Control of the carrier density, n, is achieved by varying V_g. (b) Resistivity of the sample as a function of V_g at $T = 0.25$ K. The mobility is 10000 $\mathrm{cm^2V^{-1}s^{-1}}$ outside the Dirac region. The inset shows the first quantum Hall plateau in the conductance, where the filling factor $\nu = nh/4eB$. Adapted from [24].

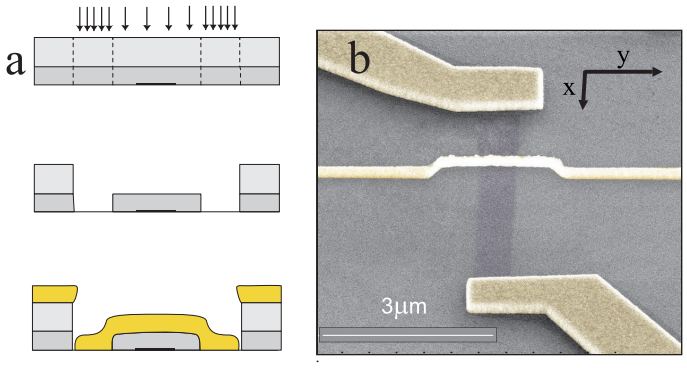

Figure 2.3: (a) Three stages of the air-bridge fabrication: electron beam lithography with two exposure doses, development, and deposition of the metal film. (b) A false-colour SEM image of a graphene flake with a metal air-bridge gate (image is tilted by 45°).

	S1	S2	S3	S5
Width, μm	0.3-0.15	0.6	0.15	0.35
Length, μm	5	4.3	1.45	5
ρ_D, kOhm	6.9	4.87	6.36	14
V_D, V	0.05	1.11	1.68	-0.75

Table 2.3: Characteristic of graphene *p*-*n*-*p* samples.

2.2.3 Graphene *p*-*n*-*p* samples

To fabricate the *p*-*n*-*p* structures, we have chosen graphene flakes of rectangular geometry on SiO_2/Si substrates with a 300 nm oxide layer. The samples have the following dimensions, in μm: L=5, W=0.24 (sample S1); L=4.3, W=0.6 (sample S2) and L=1.45, W=0.15 (sample S3). The mobility of these samples away from the Dirac point (at a carrier density of $3 \times 10^{11}\,\mathrm{cm}^{-2}$) is 13, 11 and 6 $\times 10^3\,\mathrm{cm}^2\mathrm{V}^{-1}\mathrm{s}^{-1}$, respectively. The procedure of the top-gate fabrication is illustrated in Fig. 2.3(a). Two layers of PMMA with different molar masses are spun on the flake: a soft resist (495K) on top of a hard resist (950K). They were then patterned using low-energy 10 keV, e-beam lithography (to achieve larger undercut in the top PMMA layer). Two different exposure doses were used in the areas of the span and pillars of the bridge, while the area outside the bridge was not exposed. The dose in the span is just enough to expose the soft resist, but too small to affect the underlying hard layer. Both layers are exposed at a larger dose in the areas of the pillars (and contacts). The structures are then developed and covered with 5/250 nm of Cr/Au. The 'lift off' removes PMMA leaving the bridge with a span up to 2 μm supported by two pillars. Figure 2.3(b) shows an SEM image of sample S2 with a suspended top-gate and two Ohmic contacts. The carrier mean free path in our samples $l \approx 45 - 100$ nm and the distance between the top-gate and the flakes is 130–210 nm. In the attempt to produce a *p*-*n*-*p* structure with ballistic properties, the top-gate is made short, 100–170 nm, in the direction of the current flow.

The parameters of four samples used in the thesis are presented in Table 2.3. All the samples are too narrow (less than 0.6 μm) to make a multiple-terminals, thus only two-terminal samples are made and the quantum Hall effect to characterise the sample was measured using a two-terminal geometry.

2.3 Circuitry and methods

2.3.1 I-V characteristics

A resonant current through single impurities in a DBRTD can be very small (down to ~ 10 pA). Thus to measure small signals a low-noise preamplifier was used and all circuit elements were placed inside a screen room to minimise ambient noise. An EG&G 181 current preamplifier was used to detect DC and AC currents of the order of a few pA. The circuit we have used to measure simultaneously the current, $I(V_{sd})$, and differential conductance, $dI(V_{sd})/dV_{sd}$, of the DBRTD is shown in Fig. 2.4. There are two sources of voltage: AC of 0.1 mV at 17 Hz (oscillator output of EG & G Lock-in amplifier model 5110) and DC (DAC of a CIL Microsystem PCI 6380). The DC signal was filtered using a low-pass RC-filter with cut-off frequency $f_{cut} = 4$ Hz. The output signal of the current preamplifier contained both DC and AC components. The DC component was filtered with a low-pass filter ($f_{cut} = 1$ Hz) and passed to an ADC input of the PCI 6380. The AC component was measured by the Lock-in amplifier with a time constant of ~ 1 s. The experiment was automatiated using the software CryoMeas written for Acorn computer by Dr. C. J. B. Ford from the Cavendish Laboratory, University of Cambridge. Instruments were connected through IEEE-bus, except the Lock-in amplifier, because of interference which comes from the IEEE bus. The output DC signal of the Lock-in amplifier proportional to the AC input of the Lock-in amplifier was measured by PCI 6380.

2.3.2 Resistance measurements

Graphene structures were measured using a constant current circuit with a 100 MΩ ballast resistor shown in Fig. 2.5. This current was $\sim 1 - 10$ nA. The voltage along the sample was measured using a low-noise voltage LI-75A amplifier of a NF Corporation. DC voltages applied to the gates were filtered with RC-filters with $f_{cut} = 1$ Hz.

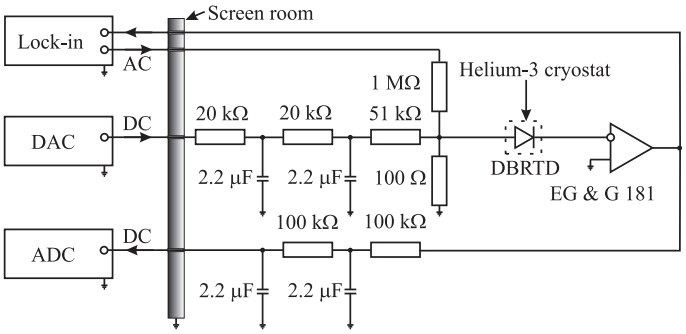

Figure 2.4: The circuit used for measurements of $I(V_{sd})$ and dI/dV_{sd}.

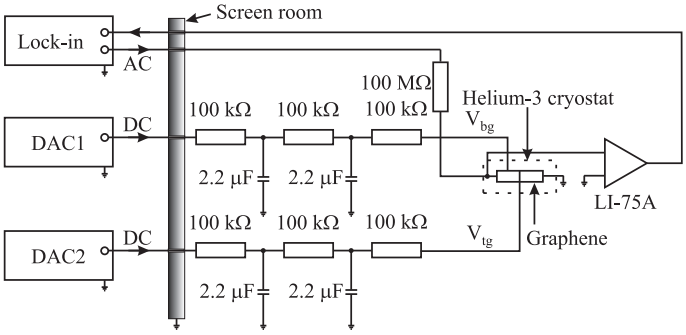

Figure 2.5: The circuit used for measurements of $G(V_{bg})$ and $G(V_{tg})$.

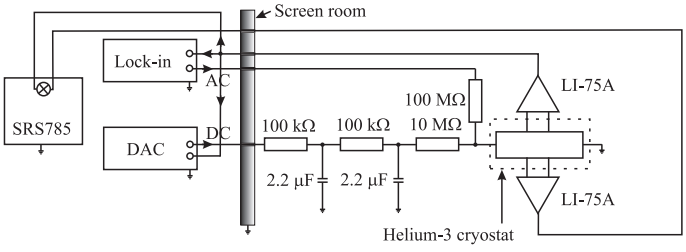

Figure 2.6: The circuit used for measurements of voltage noise.

2.3.3 Noise

The circuit for noise measurements is shown in Fig. 2.6. A constant current regime was used for both resistance and noise measurements (AC signal from the Lock-in was set to zero during noise measurements). Resistance was measured before and after noise measurements. Two low-noise voltage amplifiers were used simultaneously, connected to the opposite pairs of potential contacts. The output voltage signals of these two amplifiers were paired by a cross-correlation technique using double-channel spectrum analyser SRS785 (Stanford Research).

The cross-correlation method is used to remove the voltage noise of preamplifiers. By detecting only the correlated signals in both channels the analyser also suppresses the uncorrelated noise which comes from the thermal noise of the wires connected to the potential contacts. This technique does not suppress the current noise of the preamplifiers. However, if the sample has the same resistance at different source-drain voltages, the current noise (which depends only on this resistance) gives the same contribution to the noise spectrum at any V_{sd}. The background noise will therefore contain the thermal noise of the sample and some contribution from the current noise of the preamplifiers. In the analysis presented in this thesis the background noise is subtracted from the noise measured at a finite V_{sd} applied, which leaves only non-equilibrium voltage noise of the sample.

2.3.4 Temperature and magnetic field control

For the low temperature work the current-voltage and conductance-voltage measurements were carried out in a liquid Helium-4 dewar and using Helium-3 system HelioxTL Oxford Instruments. The Helium-3 system, Fig. 2.7, allows one to measure the temperature dependence of the current in a wide range of temperatures from 0.26 to ~ 200 K. A superconducting magnet can generate fields up to 12 T in the sample space.

The sample is mounted on a probe which is lowered down to the sample space. In order to reach base temperature, ^{3}He is released from the sorption pump and condensed into the bottom of the sample space (the "^{3}He pot") by cooling it by the 1K pot. (The 1K pot contains a small volume of liquid Helium-4 and is cooled by pumping the vapour from its surface.) When the sample is placed into the liquid

^{3}He, the sorption pump is cooled down to the temperature of the 1K pot and it starts pumping the ^{3}He vapour. This pumping cools the liquid Helium-3 down to 0.26 K. (This temperature is stable for about 100 hours.) In order to change the temperature, a heater is used to heat the sorb and the ^{3}He pot to achieve a stable temperature from 0.26 K to 3.2 K when the liquid ^{3}He is evaporated. Above this temperature the sample is in a gaseous rather than liquid surroundings. The heating power can be controlled to reach temperatures up to 200 K.

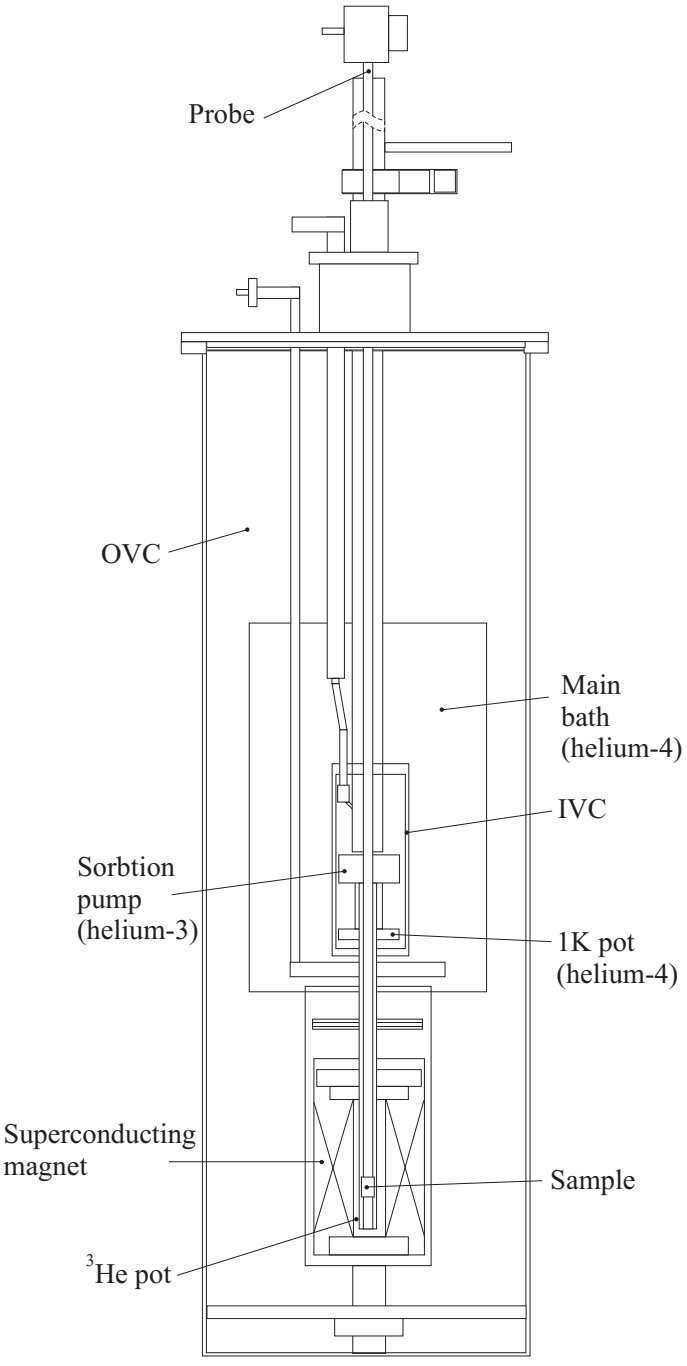

Figure 2.7: Scheme of Helium-3 cryostat.

Chapter 3

Transport through impurities in a vertical double-barrier resonant tunnelling diode

3.1 Introduction

In this chapter we describe transport measurements in a double-barrier resonant tunnelling diode (DBRTD). We have observed resonant tunnelling through single-impurity states and through double-impurity states. The effect of magnetic field on resonant tunnelling through double-impurity states is studied.

The first part of this chapter is an introduction to the physics of resonant tunnelling in a DBRTD. The theoretical models used previously for analysis of resonant currents are introduced. Some experimental results on resonant tunnelling via a single impurity or localised states in quantum dots (QD) embedded into DBRTDs are discussed.

In the second part, the experimental results on transport at low temperatures and high magnetic fields are discussed in detail using a new theoretical model. Random telegraph noise (RTN) has been observed in transport through DBRTD at 4.2 K and analysed.

3.2 Theory of resonant tunnelling

3.2.1 Resonant tunnelling via a quantum well in a DBRTD

One of the most studied devices in semiconductor physics is the resonant tunnelling diode. The current-voltage characteristics of the resonant tunnelling diode have been investigated widely in the last three decades. All possibilities of tunnelling paths and experimental conditions (such as temperature and external magnetic field) were investigated both experimentally and theoretically [25].

The region between the barriers, Fig. 1.4, of a DBRTD contains several subbands due to quantum well confinement. These diodes conduct at some applied source-drain bias, V_{sd}, when the bottom of the first subband aligns with the Fermi level in the source, Fig. 1.4(a). This bias is called the threshold voltage. If larger V_{sd} is applied, the Fermi level crosses the second subband and the current increases further.

The general behaviour of the I-V characteristic of DBRTD with negative differential resistance (NDR), Fig. 1.4(e), was discussed in [26]. Lets consider a DBRTD with one subband only, Fig. 3.1. The tunnelling current between the 3D regions via a 2D quantum well disappears at large applied V_{sd} when the bottom of the conduction band in the source aligns with the bottom of this subband. The resulting shape of the current peak is triangular, with a gradual growth at smaller bias voltages and a rapid decrease at larger V_{sd}, Fig. 1.4(e). This simple model explains the presence of NDR, see Sec. 1.2.7. If only energy subbands are considered to contribute to the current through the DBRTD, its value below the threshold voltage should be very small, but more detailed measurements [27] have revealed the existence of current peaks below this voltage. These current peaks are associated with resonant tunnelling through zero-dimensional bound states formed by shallow donor impurities in the quantum well.

3.2.2 Tunnelling through one impurity

The presence of impurities with energies below the first subband in a DBRTD dramatically increases the transparency of the structure due to resonant tunnelling (RT) which occurs when the energy of the tunnelling electrons coincides with the

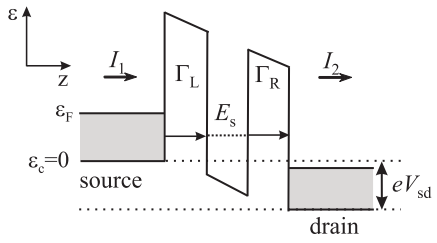

Figure 3.1: Tunnelling through a resonant state with energy E_s in a double-barrier structure. Γ_L and Γ_R are the tunnelling rates from the source to the resonant state and from the drain to the state, respectively. I_2 is the total current.

impurity level, Fig. 3.1. RT through a single impurity in a barrier has been studied in different structures, both in lateral transistors and vertical diodes [27–31]. In [27] a vertical DBRTD based on GaAs/$Al_{0.4}Ga_{0.6}As$ was investigated. The lateral size of the structure was changed electrostatically by a lateral gate (effective cross-section area reduced from 0.7 to 0.1 μm^2). In this confined structure the authors observed a tunnelling via single-impurity state by measuring current dependence on source-drain voltage and side gate voltage.

In the case of resonant tunnelling from a 3D source to a 3D drain via a 0D state in the barrier one can see a peak in I-V characteristic [32]. Due to the conservation of energy in tunnelling, the shape of the peaks has to be triangular. A resonant current appears when the energy E_s lies between the Fermi level and conduction band edge in the source, i. e. $0 < \varepsilon_s < \varepsilon_F$. Because the density of states decreases towards zero energy in 3D, the maximum current occurs when the impurity energy is equal to the Fermi energy in the source contact. By applying bias one can effectively move the impurity energy level ε_s from ε_F to zero energy (defined as the bottom of conduction band in the source) where current is zero. At intermediate biases the current decreases linearly with source-drain bias.

If tunnelling via a 0D impurity occurs from a 2D source, a triangular shape of the current peak is observed with a rapid increase of the current when the impurity energy level crosses the Fermi level in the 2DEG [33]. The current slowly decreases if larger bias voltages are applied.

We now consider sequential tunnelling through a single resonant level as shown in Fig. 3.1, when electron loose their phase after tunnelling from the source to the state. An electron tunnels from the source through the resonant state with energy E_s inside DBRTD with the rate $\Gamma_L/\hbar$. This state can exist due to unintentional

doping or can be a quantum dot formed during growth of the structure, Section 1.2.4. Then the electron tunnels to the drain with the rate $\Gamma_R/\hbar$. We can write a system of rate equations for the currents

$$I_1 = 2e\frac{\Gamma_L}{\hbar}[f_s(1-f) - f(1-f_s)], \tag{3.1}$$
$$I_2 = -2e\frac{\Gamma_R}{\hbar}[f_d(1-f) - f(1-f_d)],$$

where f_s and f_d are the Fermi-Dirac distribution functions in the source and drain, respectively, f is the probability that the resonant level is occupied and the factor of two accounts for the two spins. For current conservation we must have $I_1 - I_2 = 0$. Hence we have expression for the sequential current

$$I_1 = \frac{2e}{\hbar}\frac{\Gamma_R\Gamma_L}{\Gamma_R + \Gamma_L}, \tag{3.2}$$

where we assumed that $T = 0$ and there is a finite bias. This equation shows that to get the largest current we have to have $\Gamma_L = \Gamma_R$, which corresponds to an equal distance from the impurity to the drain and to the source. Therefore, impurities placed in the middle of the structure can be more easy detected. If this impurity is placed near one of the contacts then the tunnelling rate between them will be large but the current through the structure will be determined by the smaller tunnelling rate.

3.2.3 Tunnelling through two states

The theory of RT via two impurities was proposed in [34] and this effect was observed experimentally on a short lateral transistor [35]. It is difficult to distinguish between one- and two-impurity RT in the ohmic regime of conduction – at zero bias both effects give peaks in the conductance as a function of impurity energy. However, their I-V characteristics are quite different. Single-impurity RT produces a step-like I-V characteristic, with the threshold of the current corresponding to the impurity level coinciding with the Fermi level in the contact [32]. In comparison, the I-V characteristic of two-impurity RT has a distinct peak at the voltage, corresponding to the alignment of the two impurity levels [35] below the Fermi level in the source.

In [36] an impurity state in a RTD was used to detect the electronic structure of

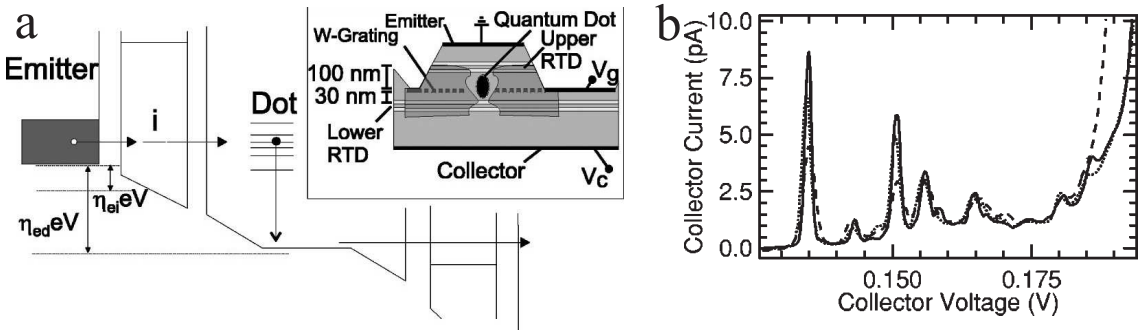

Figure 3.2: a) Conduction-band profile of a device used to probe the states of a QD with an impurity state in a DBRTD. The inset shows a schematic overview of the structure, indicating the depleted region around the tungsten wires. The quantum dot is formed between the two DBRTDs. b) I-V characteristics measured at $B = 0\,\mathrm{T}$ and $V_g = -50\,\mathrm{mV}$ for different temperatures. The solid line is for 0.3 K, the dotted 4.2 K, and the dashed 10 K. For $V_c < 0.12$ V the current is less than 0.1 pA and has no fine structure. Note the emitter corresponds to source and the collector to drain in my text. Adapted from [36].

an electrostatically defined quantum dot, Fig. 3.2a. The impurity state localised in the DBRTD moved in energy with applied voltage and at several values of V_{sd} sharp resonances occurred. These resonances are only possible when the energy level of the impurity aligns with an energy level in the QD. If we denote the energy state of the impurity by ε_i and the energy state in the QD by ε_{dot} then the corresponding shift of the states with V_{sd} are given by linear relations:

$$\begin{aligned} \varepsilon_i &= \varepsilon_i^0 - eV_{sd}\eta_i, \\ \varepsilon_{dot} &= \varepsilon_{dot}^0 - eV_{sd}\eta_{dot}, \end{aligned} \tag{3.3}$$

where ε_i^0 and ε_{dot}^0 are the energy states of the impurity and QD, respectively, at $V_{sd} = 0$, and η_i and η_{dot} are the leverage factors (coefficients of proportionality between energy and V_{sd} which are dependent on the position of the impurity and dot along the RTD). The values of η_i and η_{dot} can change from 0 (state placed near the source) to 1 (placed near the drain). The position of the resonance can be found from the equality $E_i = E_{dot}$, where the energies are taken from Eq. 3.4. The voltage where the resonance occurs is

$$V_{sd}^r = \frac{\varepsilon_{dot}^0 - \varepsilon_i^0}{e(\eta_{dot} - \eta_i)}. \tag{3.4}$$

The results of measurements with several peaks in the I-V characteristic for

different temperatures are presented in Fig. 3.2(b). It is seen that current peaks occur, with a finite background due to the overlap of the tails of the nearest peaks.

In [37] tunnelling via two QDs formed by GaAs quantum wells between AlAs barriers (triple barrier structure) in series was studied. The barrier between the two QDs was small in comparison to the barriers between the QDs and the contacts. This helped to form a strong coupling between two electron states in QDs to form a new molecular state. The authors observed steps, but not peaks, in the I-V characteristic which they attribute to the tunnelling via a state in the quantum-dot molecule. The current through this molecular state was described by the Eq. 3.2 for a single state in the well.

3.2.4 Effect of magnetic field

Impurity energy levels are affected by an external magnetic field, B, when the spreading of the wavefunction of the state becomes comparable to the magnetic length, $l_B = \sqrt{\hbar/eB}$. Magnetic field acts as an additional confining potential on the electron wavefunction and hence causes a (diamagnetic) shift of the energy level. It has been shown in [38], Fig. 3.3(a), that for a parabolic potential in the XY-plane

$$V(x,y) = \frac{1}{2}m^*\omega_0^2(x^2+y^2), \tag{3.5}$$

the energy spectrum in magnetic field oriented in the z-direction (direction of the current) is given by

$$\varepsilon_{N,l} = (2N+|s|+1)\hbar\sqrt{\omega_0^2+\frac{\omega_c^2}{4}} - \frac{s}{2}\hbar\omega_c, \tag{3.6}$$

where m^* is the effective mass of electrons, ω_0 determines the curvature of the potential, N is the radial quantum number ($N = 0, 1, 2, ...,$), s is the angular momentum quantum number ($s = 0, \pm1, \pm2, ...,$), and $\omega_c = eB/m^*$ is the cyclotron frequency. The potentials of a shallow impurity and QD can be (in the first approximation) taken as parabolic potential with an effective parameter ω_0. The influence of magnetic field on the ground state, $\varepsilon_{0,0}$, is the smallest. If $\omega_c \gg \omega_0$ then we have a linear dependence of energy on B-field, as for a zero Landau level, $\varepsilon_{0,0} = \hbar\omega_c/2$. In the opposite case, $\omega_0 \gg \omega_c$, a deep level (or weak magnetic field) will not be

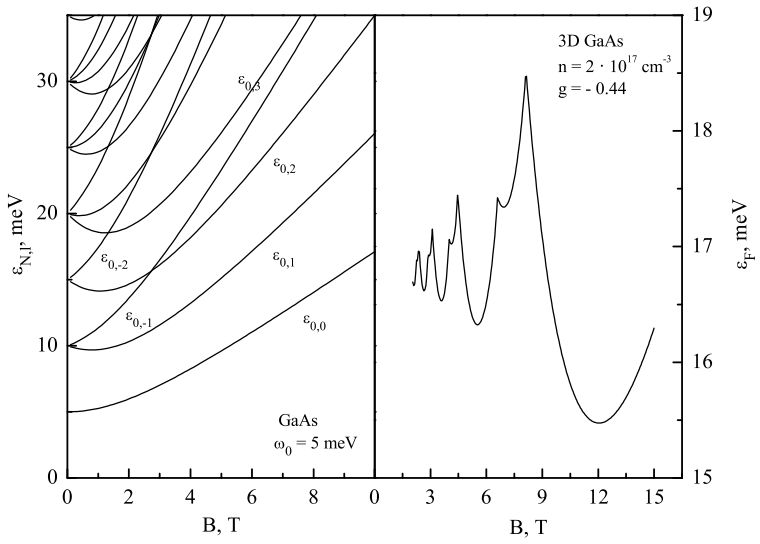

Figure 3.3: (a) Several energy levels of the impurity with $\hbar\omega_0 = 5$ meV as a function of magnetic field, Eq. 3.6. (b) Oscillations of the Fermi level in magnetic field, Eq. 3.7.

weakly affected by the magnetic field and we can expand the ground state energy as $\varepsilon_{0,0} \approx \hbar\omega_0(1+\omega_c^2/8\omega_0^2)$, which is quadratic in B. If we consider an anisotropy in the potential, for example, the well has a different size in x and y direction, then the magnetic field effect on the energy state will be more complicated than that given by Eq. 3.6.

The Fermi level in the source shifts as a function of magnetic field. The movement of the Fermi level at fixed concentration, n, of the 3D electron gas in the source can be determined from [2]

$$n = \frac{\sqrt{2}(m^*)^{3/2}}{\pi^2\hbar^3}\mu_B B \sum_{N,\sigma} \sqrt{E_F - (2N+1)\mu_B B} + \sigma g \mu_B B \qquad (3.7)$$

where $\mu_B = e\hbar/2m^*$ is the effective Bohr magneton, spin number σ takes values $\pm 1/2$, and g is the Lande g-factor of electrons. At a fixed concentration the Fermi level oscillates as a function of magnetic field, Fig. 3.3(b). In high magnetic fields spin splitting has to be taken into account (the last term in Eq. 3.7).

From an experimental point of view, a parabolic potential is a good approximation of the confinement potential of a QD. Many authors [33,36,37,39] used Eq. 3.6 to explain the shifts of the peaks or steps in the tunnelling current as a function of

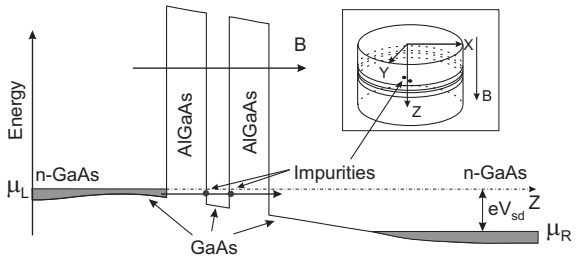

Figure 3.4: Schematic presentation of the double-barrier resonant tunnelling GaAs/$Al_{0.33}Ga_{0.67}As$ structure with an applied bias. The two dots indicate impurities in resonance.

V_{sd} and magnetic field.

Because tunnelling is sensitive to the local density of electron states in the source, the local structure of the Landau levels in GaAs has been studied by a tunnelling with magnetic field applied [40], where a single impurity of radius 10 nm (estimated from the expression $r \sim \sqrt{2\hbar/m^*\omega_0}$) was used as a detector. In magnetic field parallel to the current the local density of states can be detected, because the maximum current occurs in the region of the impurity and using magnetic field the effective impurity size can be changed (in strong magnetic field this size is given by $r \sim \sqrt{2\hbar/m^*\omega_c}$). The authors have also observed a diamagnetic shift of the ground state (N=0, s=0) described by Eq. 3.6.

In [39] resonant tunnelling from a 2DEG via InAs QDs embedded in an AlGaAs barrier was studied. Two orientations of magnetic field with respect to the current were used to estimate the size of the resonant state. When magnetic field perpendicular to the current was applied, the variation in the voltage corresponding to the current peak is determined by

$$e\Delta V = -\frac{\beta e^2 B^2}{2}\left(\frac{\langle z_e^2\rangle}{m^*} - \gamma\frac{\langle z_d^2\rangle}{m_d}\right), \tag{3.8}$$

where $\sqrt{\langle z_e^2\rangle}$ is the spatial extent of the electron wave function in the emitter, estimated using self-consistent numerical calculations, $\sqrt{\langle z_d^2\rangle}$ is the spatial extent of the barrier state, m^* and m_d are the electron masses for the electron and the electron in the well, β is the leverage factor, and γ is a geometric factor related to the shape of the confinement potential.

3.3 Experiment and analysis

3.3.1 General I-V characteristic of DBRTD

Our experiments have been performed on a vertical GaAs/AlGaAs diode structure (KIIORe23b, supplied by Giancarlo Faini from the Laboratoire de Photonique et Nanostructures, CNRS in Marcoussis, France) at temperatures down to $T = 0.25$ K. Two AlGaAs barriers of width 8.7 nm confine a 5 nm wide GaAs quantum well. The GaAs contacts contain doped regions which are separated from the barriers by spacers of 20 nm and 30 nm thickness. Fig. 3.4 shows the band diagram of the structure with a positive bias applied to the right contact. In the lateral (XY) direction the sample is etched into a pillar with a diameter of 70 nm [41]. The small cross-sectional area of the device allows one to detect the presence of individual impurities in the current through the structure [42].

We have studied sample KIIORe23b in a helium dewar at 4.2 K by measurements of I-V characteristics at different ranges of V_{sd}. Measurements of the signals below 100 nA were performed using a low-noise current preamplifier EG & G 181 (which can detect DC currents as small as 0.25 pA. A general picture of the I-V characteristic of this sample is shown in Fig. 3.5. The I-V characteristic has a diode-like behaviour with threshold voltages at 0.17 V and -0.15 V. Negative differential conductance (NDC) has been observed in the regions around ± 0.1 V. The experiments below concentrate on the region below the threshold voltage, to study the resonances that cause this NDC.

3.3.2 Random telegraph noise in DBRTD at 4.2 K

The I-V characteristic measurements below 0.1 V have shown several current peaks which are due to tunnelling through localised states inside the DBRTD. Around these peaks the current is observed to switch between two states with an approximate period of 1 s. This RTN at 4.2 K is shown in Fig. 3.6. On the graph increasing and decreasing sweeps of the bias voltage are shown. It appears that the direction of the sweep has no effect on the RTN, that is there is no hysteresis effect. The most intense noise occurs in the range from 60 mV to 80 mV in V_{sd} around the current peak of 20 pA. It can be seen that there are two main states for the current indicating

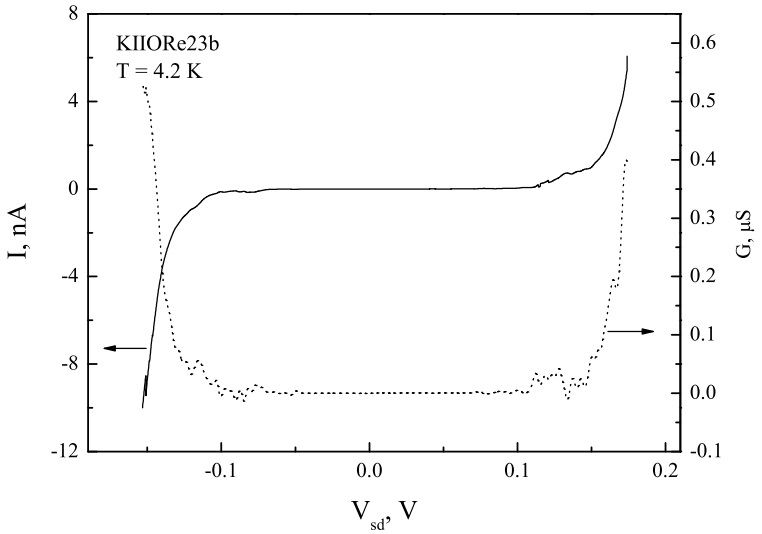

Figure 3.5: The I-V characteristic (solid line) of the KIIORe23b sample from -0.15 V to 0.17 V at 4.2 K. The dotted line shows the simultaneously measured differential conductance, G, as a function of V_{sd}. Negative differential conductance near ± 0.1 V corresponds to the presence of peaks in the I-V characteristic.

that noise originates from the switching of a single impurity (however, there are also small-amplitude switchings with much lower rate). The two states look identical when shifted along V_g. RTN can be produced by charging and discharging of an impurity in one of the contacts or in the barrier close to the drain. In this case charging this impurity does not change the amplitude of the peak, but it creates an effective source-drain bias, which shifts the peak position by a constant voltage. In the insert of Fig. 3.6 a slow voltage sweep is shown. The peak at 70.7 mV is shifted by the change in occupancy of the impurity state to a new position 73 mV. This fluctuating peak has good reproducibility with time and from one cool-down to another (the amplitude varies between 19 and 22 pA).

To analyse this RTN we have divided the V_{sd} region from 56 mV to 78 mV around the peak (with 27500 data points) into 50 smaller regions (with 550 point in each). Then we have calculated the distribution of the current in each region. The resulting histogram was fitted by a double Gaussian function to find the maxima of the distribution. The results of the analysis are shown in Fig. 3.7(a,b). The solid circles represent the first state which is populated at smaller V_{sd}, and the empty circles are related to the second state, which is populated at the larger biases. The

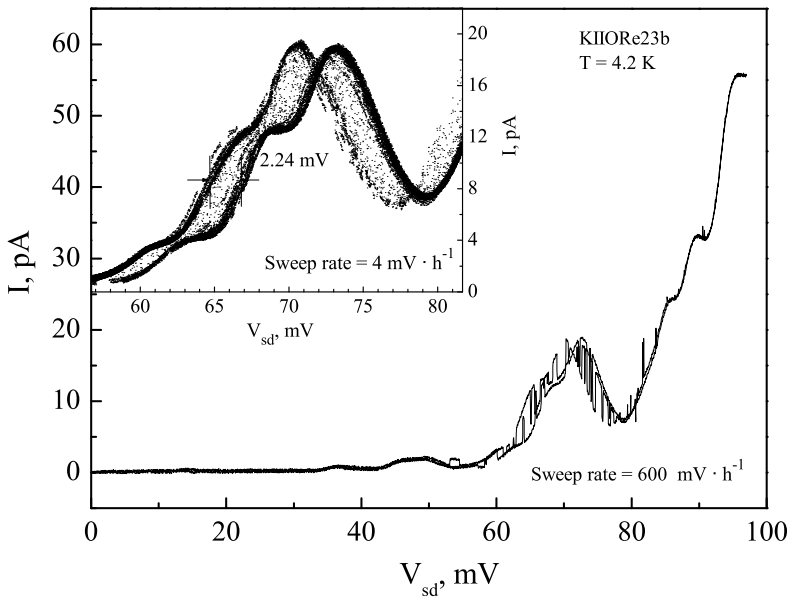

Figure 3.6: The $I(V_{sd})$ characteristic of sample KIIORe23b at 4.2 K measured twice with sweep rate 600 mVh^{-1}. One can see switching between two states. Inset: the $I(V_{sd})$ characteristic measured with sweep rate 4 mVh^{-1} with results presented as individual points. The shift in V_{sd} between the two states is about 2.4 mV.

position of the minimum between the two peaks in the histogram can be used to distinguish the two states from each other. The total number of counts from this minimum to the left represents the total time of population of the low-current state. We can find the probability to find an electron in state 2 as a function of V_{sd} by dividing this number by the total number of counts, Fig. 3.7(c), which shows an approximately a linear dependence on V_{sd}.

It is expected that RTN rate has an exponential increase with increasing temperature [6] because it is easier to occupy an impurity at higher temperature. Thus to get a more stable system without RTN lower temperatures are required.

3.3.3 I-V characteristics at T=0.25 K

Fig. 3.8 shows an I-V characteristic of sample KIIORe23b at 0.25 K measured in a Helium-3 cryostat. The threshold voltage has not changed in comparison to that observed in a dewar at 4.2 K, Fig. 3.5. One can distinguish several regions in the I-V characteristic: a region with small peaks of amplitude less than 0.1 nA and

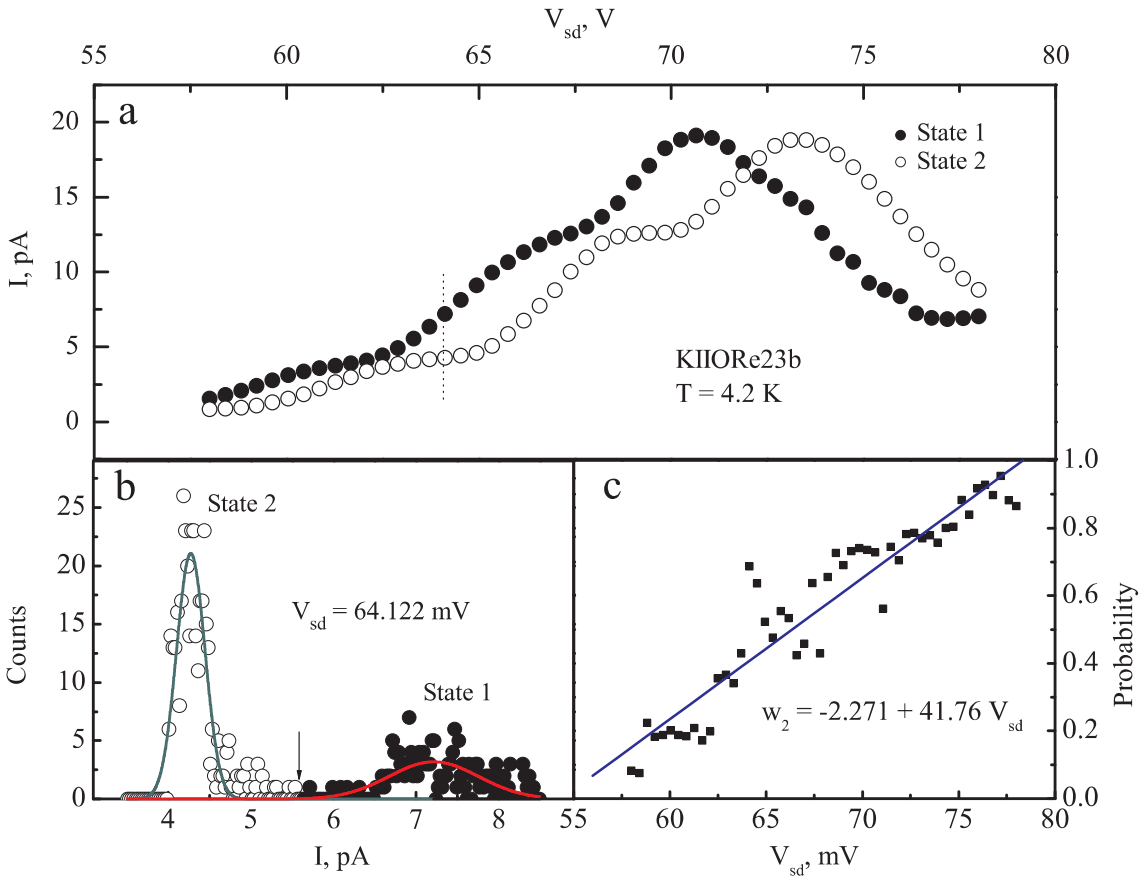

Figure 3.7: (a) Current as a function of V_{sd} of sample KIIORe23b for two separated states at 4.2 K. State 1 is shown by filled circles and state 2 by empty circles. (b) Distribution of the currents at $V_{sd} = 64.122$ mV (shown in (a) by dashed vertical line). Arrow shows current value (5.45 pA) taken to separate two states. Solid line shows fit using sum of two Gaussian functions. (c) Probability to find an electron in state 2 as a function of V_{sd}. The solid line is a linear fit.

small background; a region with larger peaks with amplitudes of about 0.1 nA on a background of about 0.1 nA; and a larger V_{sd} region where the current increases rapidly at the threshold voltage of 0.15 V. We are interested in the first region with small well resolved peaks of 10 pA amplitude.

We have focused our attention to the range of voltages from 55 mV to 70 mV, where several peaks are seen. This region of the source-drain bias (with the current of the order of 10 pA) below the threshold voltage corresponds to transport via impurities in the structure. At the beginning of the experiment, the I-V characteristic was not stable and many RTN signals which not only shifted the current peaks but also changed their amplitudes were observed. The structure of the peaks was stabilised by sweeping the voltage in this range of V_{sd} for two weeks at base temperature. Fig. 3.9(a) shows the I-V characteristic of sample KIIORe23b where

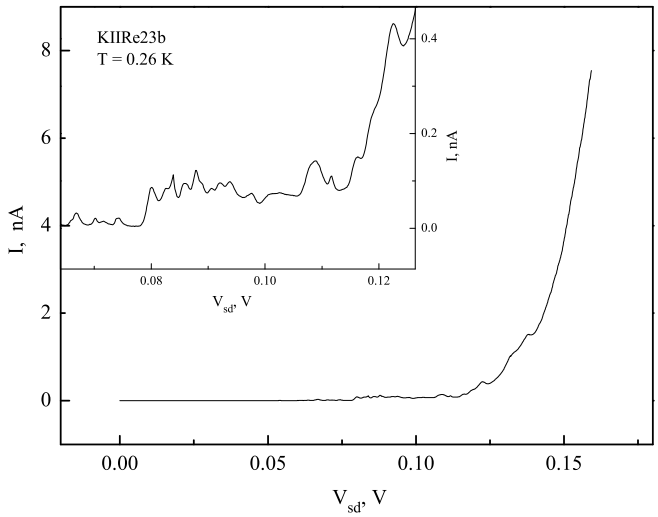

Figure 3.8: General view of the I-V characteristic of sample KIIORe23b at 0.25 K. Inset: zoomed in region before threshold voltage with many small current peaks with the amplitude of 50 pA.

both current peaks with small RTN and a quite stable peak near at 67.8 mV are present.

The peak at 67.8 mV is of Lorentzian shape and it was studied in detail. It is not well separated from the nearest current peaks from which we conclude that the background (in the first approximation) comes from the tails of these peaks. This is demonstrated by the fact that the I-V characteristic in this range can be fully described by the sum of several peaks of Lorentzian shape, Fig. 3.9(b).

The observed peak in the I-V characteristic is interpreted as a result of two-impurity RT. The position of the peak on the voltage scale contains information about the energy levels of the two impurities, and the peak amplitude and its width are determined by the spatial position of the impurities (the overlap of the two wavefunctions with each other and the contacts, as well as the relative shift of the two energy levels with bias).

We have seen that the shape of the peaks in the pre-threshold region is temperature independent, which is in agreement with RT through two levels placed between the Fermi levels in the right and left contacts, Fig. 3.4, and not affected by temperature smearing of the distribution functions in the contacts. The shape of the peak

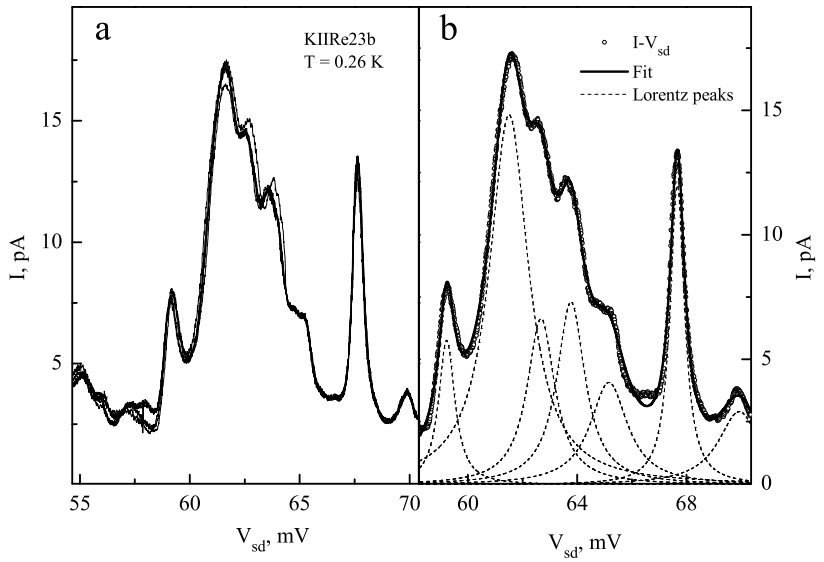

Figure 3.9: The I-V characteristic of sample KIIORe23b at 0.25 K from 55 mV to 79 mV. (a) Several sweeps with small RTN. (b) Fitting of the I-V characteristic (empty circles) using seven Lorentzian peaks (dashed curves). The resulting fit is shown by a solid thick line.

is described by a Lorentzian [35]:

$$I(\Delta V_{sd}) = \frac{2e}{\hbar} \frac{\Gamma_L \Gamma_R |H_{LR}|^2}{(\beta_{LR} e \Delta V_{sd}/2)^2 \Gamma_L \Gamma_R / (\Gamma_R + \Gamma_L) + (\Gamma_R + \Gamma_L)(\Gamma_R \Gamma_L + |H_{LR}|^2)}, \quad (3.9)$$

where $\Gamma_L(\Gamma_R)$ is the tunnelling rate from the left (right) impurity to the left (right) contact, H_{LR} is the overlap integral between the wavefunctions of the two impurities, $\beta_{LR} = \beta_R - \beta_L$, $\beta_{L,R} = \mathrm{d}\varepsilon_{L,R}/\mathrm{d}eV_{sd}$ is the leverage factor related to the shift of the impurity level with a voltage applied, ε_L and ε_R are the energies of two levels (with respect to the Fermi level in the left contact), ΔV_{sd} is the bias voltage with respect to the resonant value V^r. The amplitude of the peak

$$I_0 = I(\Delta V_{sd} = 0) = \frac{2e}{\hbar} \frac{\Gamma_L \Gamma_R |H_{LR}|^2}{(\Gamma_R + \Gamma_L)(\Gamma_R \Gamma_L + |H_{LR}|^2)}, \quad (3.10)$$

and the half-width at half-height is determined by

$$W_{1/2} = \frac{2}{\beta_{LR} e} (\Gamma_L + \Gamma_R) \sqrt{1 + \frac{|H_{LR}|^2}{(\Gamma_L + \Gamma_R)^2}}. \quad (3.11)$$

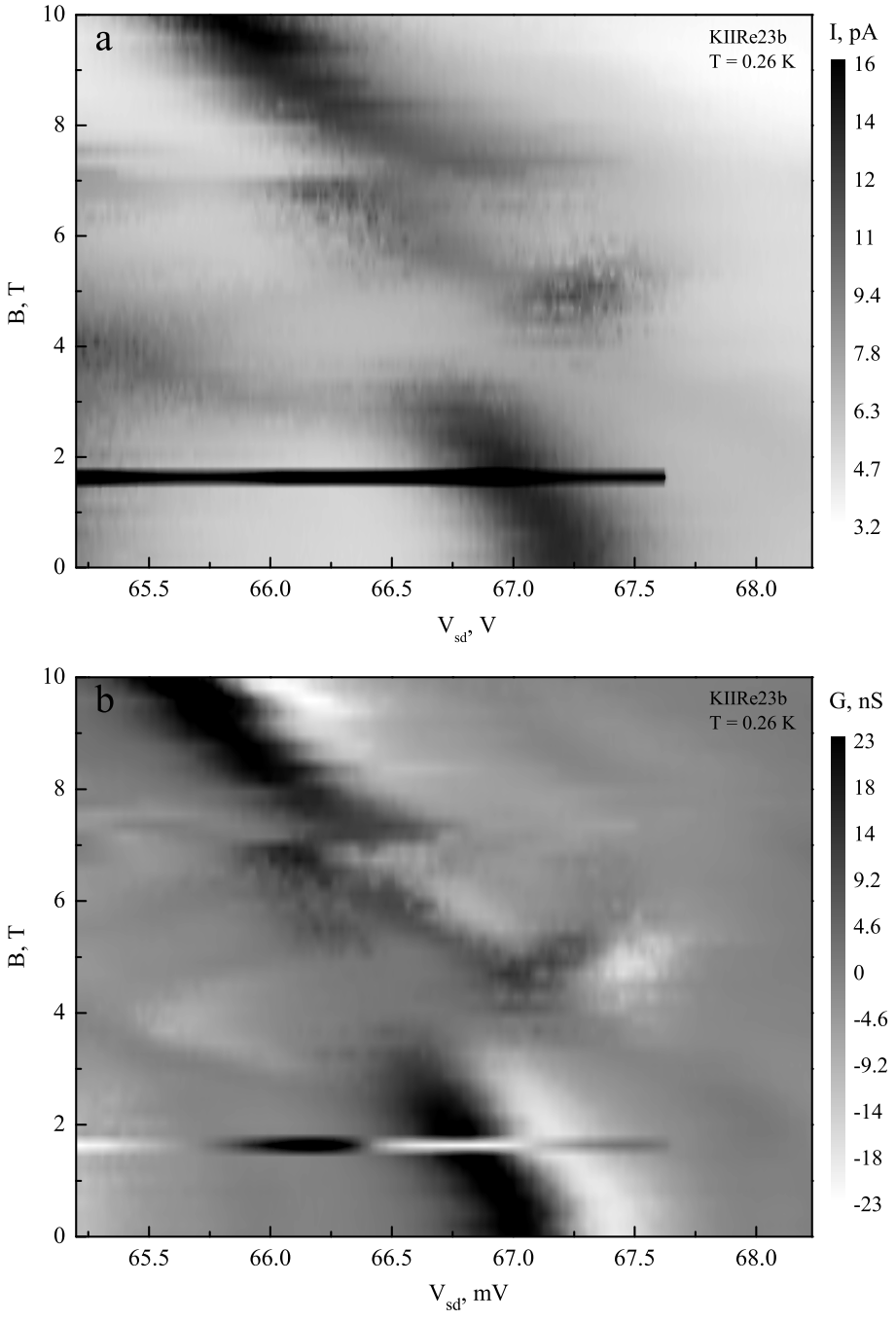

Figure 3.10: (a) Grey-scale of the current as a function of V_{sd} and B of sample KIIORe23b at 0.25 K (first measurement). The darkest region represents the largest current. The black line at $B = 1.6$ T is RTN. (b) Grey-scale of the conductance as a function of V_{sd} and B measured simultaneously with the current. NDC is seen as white regions on the graph.

3.3.4 Effect of magnetic field on the current peak

To understand more about the properties of these two impurities, a magnetic field parallel to the current has been applied. Fig. 3.10(a), shows how the I-V characteristic changes as a function of magnetic field. The differential conductance, Fig. 3.10(b), shows the position of the current peak more distinctly. The reproducibility test (Fig. 3.11) performed confirmed that there was no effects on the shift of the peak due to RTN.

The dark line near 1.6 T in Fig. 3.10(a) is indeed the second state of a RTN in the I-V characteristic, which has a larger current. The studied peak in the current was stable during several days when magnetic field dependance experiments have been performed. This is confirmed by repeated experiment, Fig. 3.11, where no RTN at $B = 1.6$ T was detected (one has to notice though that the RTN seen in Fig. 3.10 around $B = 1.6$ T is not associated to a special B-field, and it only occurred in that moment of time during the long term experiment).

Fig. 3.11 shows the current characteristics for the peak at $V_{sd} = 67$ mV in magnetic fields up to 10 T. The main feature is a shift of the peak to smaller voltages in weak magnetic fields. From 0 T to 2 T the amplitude of the current peak does not change, but above 2 T the amplitude decreases linearly as a function of magnetic field and becomes zero at 4 T, Fig. 3.12. In the range of magnetic fields from 4 T to 8 T there are two current peaks with a random switching between them. In this region the amplitudes of the peaks can both increase or decrease with V_{sd} and B. Another region begins at 8 T, when another current peak is seen, whose amplitude increases monotonically and the position of the peak shifts to smaller voltages, indicating a similar origin for this peak shift as for the peak observed at small magnetic fields (below 4 T). To analyse the shift of the peak seen below 4 T we have used a fitting procedure with a Lorentz shape function (analogous to Eq. 3.9 but with a background):

$$I = y_0 + \frac{A_L \omega^2}{4(x - x_c)^2 + \omega^2}, \tag{3.12}$$

where y_0 is a background current which probably comes from the tails of the nearest peaks, x_c is the position of the maximum of the peak in V_{sd}-scale, A_L is a current amplitude, and ω is the full width at half maximum.

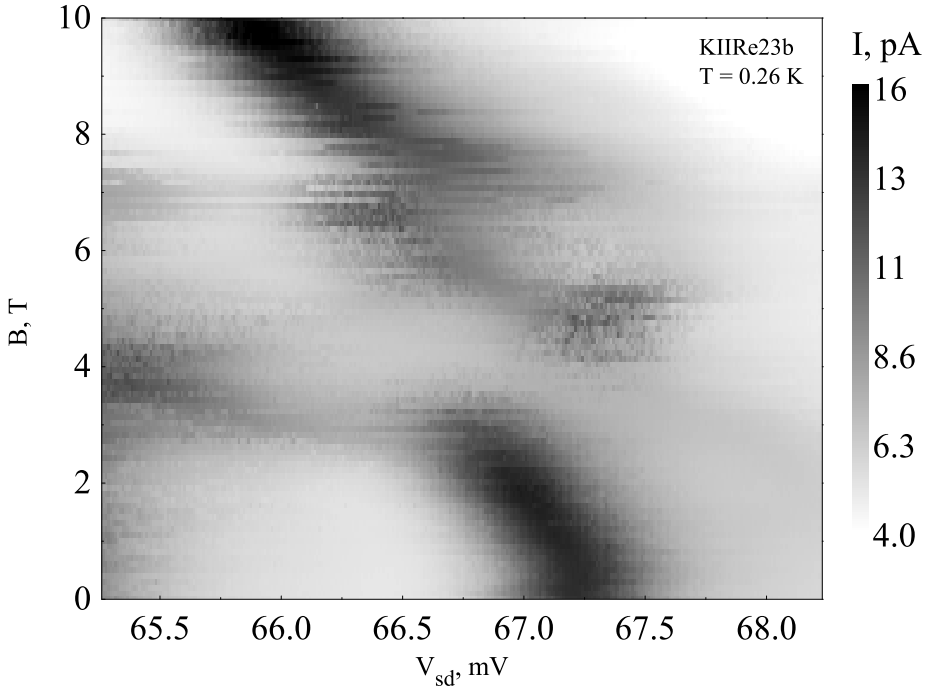

Figure 3.11: Grey-scale of the current as a function of V_{sd} and B of sample KIIORe23b at 0.25 K (second measurement).

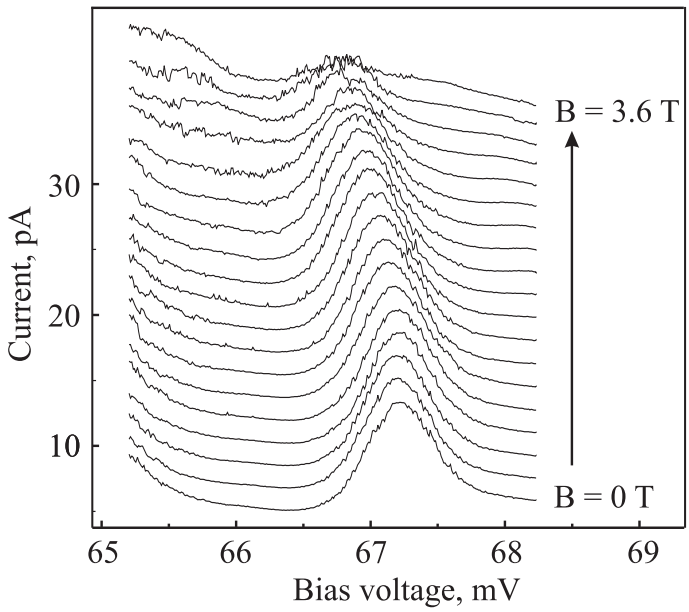

Figure 3.12: Current as a function of bias at different magnetic fields. The curves are shifted vertically from the curve at $B = 0$ T for clarity.

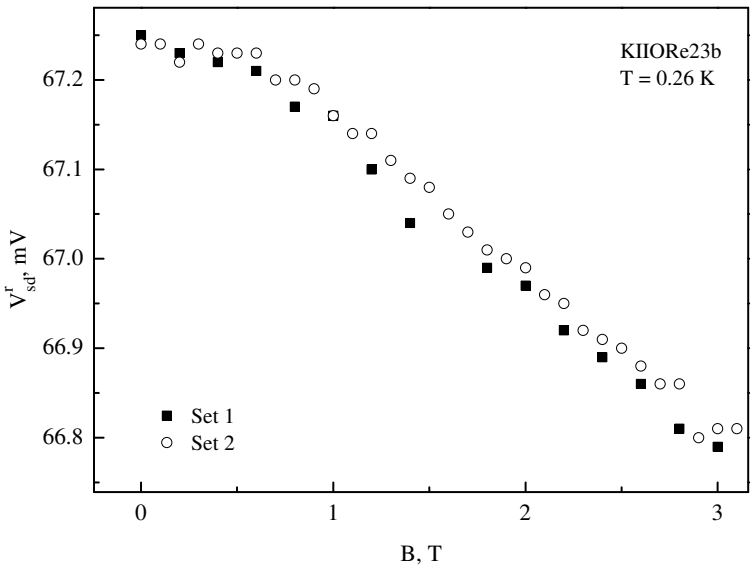

Figure 3.13: The position of the current peak as a function of magnetic field from 0 T to 3 T for two sets of experiments.

Figure 3.13 shows the shift of the current peak due to magnetic field. On the graph two sets of experimental data are presented, taken a day apart. One can see a good agreement in the shift of the current peak position as a function of magnetic field, which can be described as a linear dependence from 0.7 T to 3 T:

$$V^{\mathrm{r}}_{sd}[\mathrm{V}] = 0.06734 - 1.784 \cdot 10^{-4} B[\mathrm{T}]. \tag{3.13}$$

This (diamagnetic) shift has different sign to be explained in terms of single impurity diamagnetic shift. Indeed, according to Eq. 3.6 in strong magnetic field one should see a liner diamagnetic shift up with increase of the energy state $\varepsilon_{0,0} = \hbar\omega_c = \hbar eB/2m^*$ and it is required a larger V_{sd} to achieve a new resonant level of the impurity. For the two-impurity RT the shift of the current peak comes from the difference of the shift of the two levels (if for example both levels are shifted with B by exactly the same energy, no shift of the peak in I-V will be detected). On the other hand, if the left impurity (close to the source) shifts faster in B-field than the right impurity we will observe a shift of the current peak to lower voltages as seen in experiment.

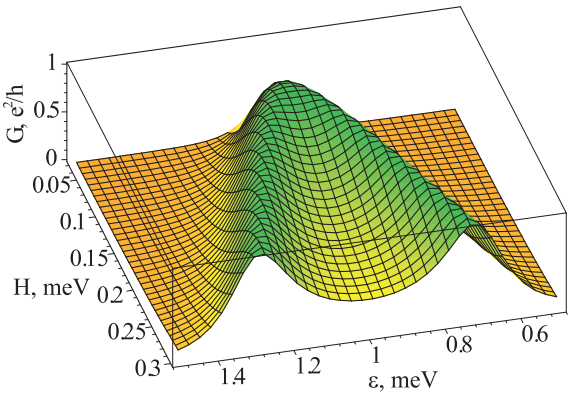

Figure 3.14: Conductance as a function of electron energy and overlap integral; $\Gamma = 0.1\,\text{meV}$; $\varepsilon^r = 1\,\text{meV}$, Eq. 3.19.

3.3.5 Analysis of the current peak in the presence of magnetic field

Let us consider the situation of tunnelling through two impurities inside a resonant tunnelling diode at zero temperature. From [34] the conductance

$$G = \frac{e^2}{h} T(\varepsilon, \varepsilon_1, \varepsilon_2) = \frac{e^2}{h} \frac{4\Gamma_L \Gamma_R |H_{LR}|^2}{|(\varepsilon - \varepsilon_1 + i\Gamma_L)(\varepsilon - \varepsilon_2 + i\Gamma_R) - |H_{LR}|^2|^2}, \tag{3.14}$$

where $T(\varepsilon, \varepsilon_1, \varepsilon_2)$ is the transmission probability for an electron with energy ε through two localised states at ε_1 and ε_2. (The leak rates and overlap integral can change with applied voltage, but at the low voltages we neglect these changes.)

If we assume that $\varepsilon_1 = \varepsilon_2 = \varepsilon^r$ and $\Gamma_L = \Gamma_R$ we can plot the conductance (Eq. 3.14) as a function of the electron energy ε and overlap integral, Fig. 3.14. One can see that if $H_{LR} \ll \Gamma_L$ one gets a single peak in the conductance, which splits into two in the case when $H_{LR} \gg \Gamma_L$.

The energies of the impurities as a function of bias can be written in the following form

$$\varepsilon_1 = \varepsilon_1^0 - \beta_L eV, \tag{3.15}$$

$$\varepsilon_2 = \varepsilon_2^0 - \beta_R eV, \tag{3.16}$$

where ε_1^0 and ε_2^0 are the localised state energies without bias, and V is an applied voltage. In this vertical double-barrier structure we do not have a gate to vary the energy levels of the impurities (which would be the case in lateral structures with

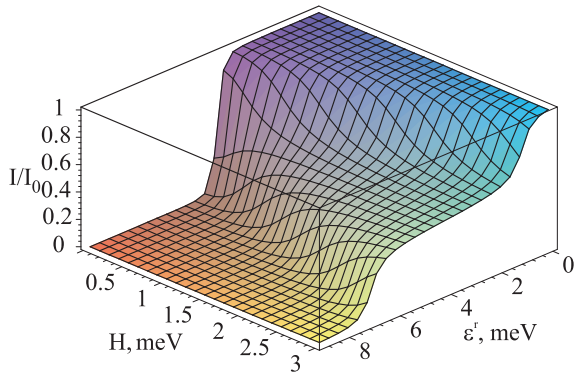

Figure 3.15: Normalised amplitude of the current peak as a function of resonance level position ε^r and overlap integral H; $\Gamma = 0.3\,\text{meV}$; $\mu = 4\,\text{meV}$, Eq. 3.19.

double quantum dots). However, we can use an external magnetic field which will similarly shift the energy levels. If the potential energy of the localised states can be presented by a parabolic potential, then we can rewrite expressions (3.15) and (3.16) taking into account the diamagnetic shift of each impurity level [38]:

$$\varepsilon_1 = \sqrt{(\varepsilon_1^0)^2 + \left(\frac{\hbar\omega_c}{2}\right)^2} - \beta_1 eV, \qquad \varepsilon_2 = \sqrt{(\varepsilon_2^0)^2 + \left(\frac{\hbar\omega_c}{2}\right)^2} - \beta_2 eV, \tag{3.17}$$

where $\omega_c = eB/m^*$ is the cyclotron frequency of an electron with effective mass $m^* = 0.067m_0$ in bulk GaAs. Here we assume that the leak rates do not depend on applied magnetic field and the magnetic field orientation is parallel to the current. This means that magnetic field does not change the size of the impurity wave function in the direction of current flow and thus the leak rates and the overlap integral are not changed significantly by magnetic field.

As we are interested in the amplitude of the current, we need to discuss the situation at resonance, which happens when the energies of the two impurities are equal. The resonant energy of the two impurities (counted from the bottom of the conduction band in the source) is

$$\varepsilon^r = \left(1 + \frac{\beta_1}{\beta_2 - \beta_1}\right)\sqrt{(\varepsilon_1^0)^2 + \left(\frac{\hbar\omega_c}{2}\right)^2} - \frac{\beta_1}{\beta_2 - \beta_1}\sqrt{(\varepsilon_2^0)^2 + \left(\frac{\hbar\omega_c}{2}\right)^2}. \tag{3.18}$$

This is found from the condition $\varepsilon_1 = \varepsilon_2$ using Eq. 3.17. Integration of Eq. 3.14 over energy with infinite limits can be replaced by integration over a semi-finite interval due to the step-function shape of the Fermi-Dirac distribution function. (The full procedure of integration is presented in Appendix A.) The resulting expression for

the maximum current is

$$I_{max} = \frac{e}{h}\frac{\Gamma_L\Gamma_R|H_{LR}|^2}{H(H^2+\Gamma^2)}\left[\frac{1}{2}\ln\left(\frac{(\mu+H-\varepsilon^r)^2+\Gamma^2}{(\mu-H-\varepsilon^r)^2+\Gamma^2}\right)+\right.$$
$$\left.+\frac{H}{\Gamma}\left[\tan^{-1}\left(\frac{\mu+H-\varepsilon^r}{\Gamma}\right)+\tan^{-1}\left(\frac{\mu-H-\varepsilon^r}{\Gamma}\right)+\pi\right]\right], \tag{3.19}$$

where $H = \sqrt{|H_{LR}|^2 - \frac{1}{4}(\Gamma_L-\Gamma_R)^2}$ and $\Gamma = \frac{1}{2}(\Gamma_L+\Gamma_R)$.

Fig. 3.15 shows the dependence on resonant level position ε^r and overlap integral H of the current amplitude normalised over the current magnitude at $\varepsilon^r = 0$. In the figure one can see the transition from a smooth 'single-step' monotonic dependance for $H \ll \Gamma$ to a 'two-step' dependence in the case when $H \gg \Gamma$.

3.3.6 Diamagnetic shift and current amplitude

The fact that the amplitude of the current peak does not depend on magnetic field (from 0 T to 2 T), Fig. 3.16, tells us that the overlap of the wave functions is not affected by magnetic field. This means that in Eq. 3.19 H_{LR} is not affected by B-field, that is the impurities are spatially aligned along the direction of the magnetic field (i.e. the distance between the impurities in the XY-plane is smaller than the magnetic length, 18 nm at 2 T).

We interpret the shift of the peak by the diamagnetic shift of impurity levels, caused by squeezing the electron wavefunctions in the XY-plane of the structure. If two impurities were shifting equally in magnetic field, the position of the resonance would remain unchanged. The shifts towards smaller V_{sd} means that the shift of the left impurity is stronger than that of the right impurity (Fig. 3.4). (The fact that the resonance is observed at a positive bias also means that the original (zero bias) position of the left energy level is lower than that of the right level.)

The position of the current peak in voltage, V^r, can be written analytically for a simple model of two parabolic confining potentials of the two impurities (one can show that the results of this approximation are close to that obtained for Coulomb

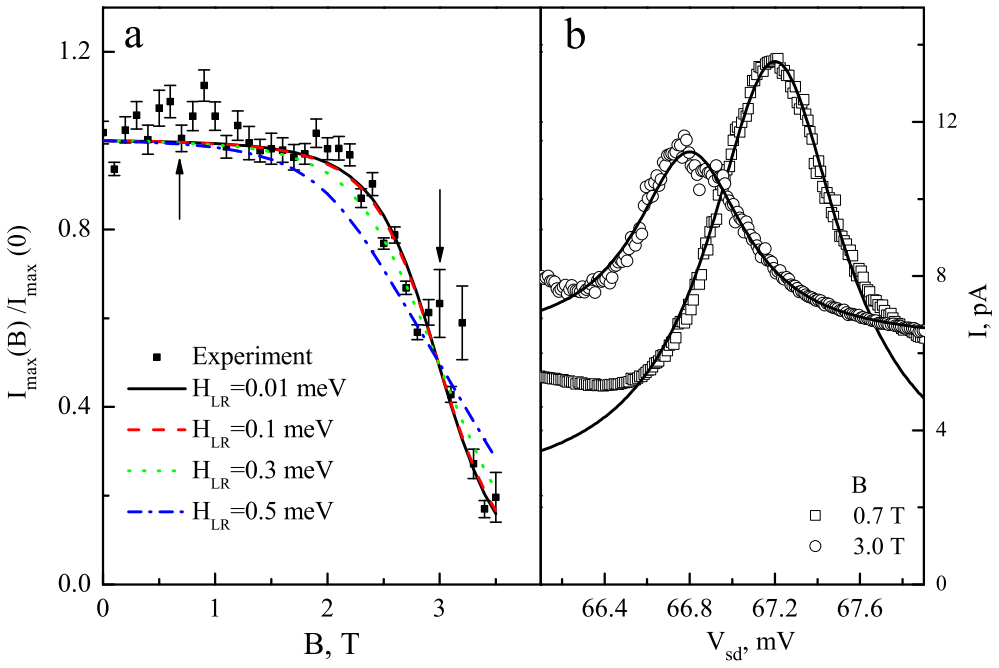

Figure 3.16: (a) The ratio of the current amplitudes as a function of magnetic field from 0 T to 3.5 T. Four curves generated from Eq. 3.18 with different overlap parameter, H_{LR} are presented. (b) Current as a function of bias, V_{sd}, for two magnetic fields (0.7 T, 3 T), shown in (a) with arrows.

impurities [4]):

$$V^r = \frac{1}{e\beta_{LR}} \left(\sqrt{(\varepsilon_R - \varepsilon_{0R})^2 + \left(\frac{\hbar\omega_{cR}}{2}\right)^2} - \sqrt{(\varepsilon_L - \varepsilon_{0L})^2 + \left(\frac{\hbar\omega_{cL}}{2}\right)^2} + \varepsilon_{0R} - \varepsilon_{0L} \right), \tag{3.20}$$

where ε_L and ε_R are the energies of the two levels, ε_{0R} and ε_{0L} are the energies of the bottoms of the parabolic potentials, $\omega_{cR,L} = eB/m_{R,L}$. The difference in the diamagnetic shifts of the two impurities, controlled by the difference in their cyclotron masses, can be easily obtained from the linear shift seen above 1.5 T, Fig. 3.17, given by Eq. 3.13. (The linear dependence in Eq. 3.20 corresponds to the situation when the diamagnetic shifts are stronger than the ground state energy of the impurities. In other words, the parabolic potential in the XY plane is weaker than the magnetic field potential at $B > 1.5$ T.) This gives us directly the relation between the two cyclotron masses (m^* is the bulk electron mass in GaAs), with

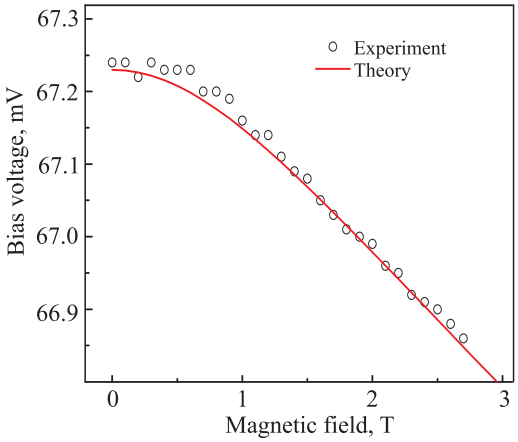

Figure 3.17: Position of the current peak as a function of magnetic field, with a fitting curve, Eq. (3.20).

$m_L < m_R$:

$$\frac{m^*}{m_R} - \frac{m^*}{m_L} = -0.2\beta_{LR}. \tag{3.21}$$

We can obtain a self-consistent picture by assuming that the two impurities are positioned in the AlGaAs barriers, close to the interfaces with the GaAs quantum well, Fig. 3.4. The geometry of the structure will then give the value of $\beta_{LR} \sim 0.1$ and therefore the difference between the two masses of about 2%. The fitting of the whole curve in Fig. 3.17 gives then the values of the ground state energies of the impurities in the parabolic potential: $\varepsilon_R - \varepsilon_{0R} \simeq \varepsilon_L - \varepsilon_{0L} = 1.5$ meV. This value is about four times smaller than the value obtained from the comparison of the Coulomb potential (with the bulk mass) with the parabolic potential. Positioning of the impurities at the AlGaAs/GaAs interfaces accounts for the difference, as half of the Coulomb potential is now replaced by a high potential wall.

Let us now discuss the origin of the decrease in the current in Fig. 3.16(a) from $B = 2$ T to 4 T. One possibility is that the level of the left impurity is shifted up with magnetic field and at $B \sim 2$ T it becomes higher than the Fermi level in the left contact, Fig. 3.4. Then the range of fields where this decrease occurs (~ 1 T) is related to the width of the resonance. There is a problem, however, in this explanation because the width of the resonance determined from the current peak, Fig. 3.16(b), appears to be two times smaller than expected for such a scenario. This fact requires further investigation: it is possible that other effects (such as a decrease of the overlap in magnetic field, or slowing down of the energy level shift near the Fermi level) are responsible for the decrease of the current peak in magnetic field.

The result of fitting using Eq. 3.18 for different overlaps (H_{LR}) are also presented. We can conclude that the best fit is observed for the parameter $H_{LR} < 0.1$ meV, which implies small overlap between the two resonant states.

3.4 Conclusions

Resonant tunnelling through two impurities has been observed for the first time in a vertical double-barrier resonant tunnelling diode structure. The current-voltage characteristic has been studied in parallel magnetic field and analysed with the help of the developed model. It was shown that resonant tunnelling in magnetic field gives information about the properties of the impurities: the energy levels, the effective electron mass and spatial positions of the impurities in the structure.

Chapter 4

Charge carrier transport in graphene

4.1 Introduction

The aim of this chapter is to describe the diffusion model and simplifications we have used to model carrier transport in graphene. The model is used successfully to predict the energy dependence of the resistance in top-gated structures in graphene flakes with low mobility. There is a striking deviation from the model when a *p*-*n* junction is formed in graphene flakes where the carriers have a higher mean free path. This is discussed with the help of a ballistic transport model by Cheianov and Fal'ko [43].

Transport through *p*-*n* and *p*-*n*-*p* junction has been calculated numerically both in the diffusive and ballistic regime. For all calculations we have used Comsole FEMLab software, which uses a similar programming language to MatLab often used for scientific computations. (All source codes with comments are placed in Appendixes.) The code for the ballistic model was written by F. Guinea (Instituto de Ciencia de Materiales de Madrid, CSIC, E28049 Madrid, Spain). To describe oscillatory behavior observed in the transmission probability through a *p*-*n*-*p* junction we have used a code also provided by F. Guinea.

4.2 Graphene

Graphene is a two-dimensional crystal of carbon atoms connected in a honeycomb lattice. This single atom thick crystal was first created experimentally in 2004 by a University of Manchester research group lead by Andre Geim [18, 44]. Graphene has attracted considerable interest after its discovery, most notably because of its unusual, linear dispersion relation for the charge carriers [45], which emulates high energy relativistic physics in table-top experiments. Such phenomena as Klein tunnelling [46] and Zitterbewegung [47] which have analogues in quantum electrodynamics were theoretically predicted in 2006 in graphene.

The vast majority of experiments to date have been carried out on graphene made by a mechanical exfoliation technique [18] where a graphite monocrystal is repeatedly split into thinner and thinner slices using an adhesive tape. These slices may contain many layers of graphene and also single atomic layers. Then the slices are deposited on an oxidised Si wafer. As soon as graphene has been deposited, the problem of finding a monolayer in the deposit arises. It was found experimentally that the graphene layer affects the resonant backscattering of light through the SiO_2 on the Si surface, and the visibility of single/few layer graphene problem has been solved by means of thin-film optics theory [48, 49], where the dependence of reflected light intensity from the structure on angle of light beam incidence, thickness of substrate, and dielectric constant of the substrate has been calculated. It was discovered that single-layer graphene is better seen on top of Si wafer with specific thickness (100 nm and 300 nm) of SiO_2.

In spite of a single-atom thickness, graphene is chemically stable [18] and able to withstand lithography processing. In order to verify the single atomic nature of graphene, quantum Hall effect [21, 22] and Raman spectroscopy [50] are used. High quality samples with a six-terminal Hall bar geometry have revealed, in quantising magnetic fields, a peculiar half-integer quantum Hall effect in monolayer graphene [21, 22]. In Raman spectra so-called D peak can help to distinguish a single-layer from bilayer and triple layer graphene [50].

In the following subsections an introduction to the physics of graphene based on a low energy approximation of transport on honeycomb lattice is presented.

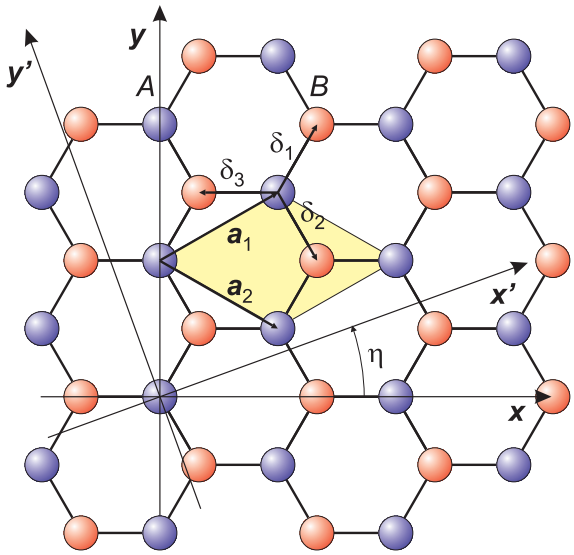

Figure 4.1: Graphene honeycomb crystal lattice. Two independent sublattices A and B are shown by different colours.

4.2.1 Crystal lattice

All the unique properties of graphene emerge from its honeycomb crystal lattice structure. The lattice of graphene consists of hexagons with carbon atoms placed in their corners with angles of 120° between them. The distance between nearest neighbours is $d = 0.142$ nm. In a unit cell of graphene, as shown in Fig. 4.1, there are two atoms shown by different colours. All atoms of type A, shown in blue, form a triangular sublattice where the atoms' positions can be expressed in terms of unit lattice vectors $\mathbf{a}_1$ and $\mathbf{a}_2$:

$$\mathbf{r}_A = m\mathbf{a}_1 + n\mathbf{a}_2, \tag{4.1}$$

where m and n take values $0, \pm 1, \pm 2....$ The unit vectors in two-dimensional space for the lattice shown in coordinate system (X, Y) in Fig. 4.1 are

$$\mathbf{a}_1 = \frac{d}{2}\left(3, \sqrt{3}\right), \mathbf{a}_2 = \frac{d}{2}\left(3, -\sqrt{3}\right). \tag{4.2}$$

The second sublattice made from B-type atoms is shifted by a vector $\delta_\mathbf{3}$. A sublattice, Λ_A, has a set of all possible vectors $\mathbf{r}_A$ and B sublattice, Λ_B, contains vectors $\mathbf{r}_A - \delta_3$. The vectors defining the nearest neighbours in sublattice B, shown by the

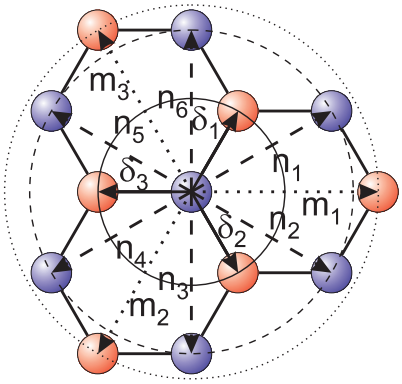

Figure 4.2: Neighbouring atoms in the graphene crystal: nearest neighbours, next to nearest neighbours, and third nearest neighbours in the same sublattice with translating vectors between them indicated by solid, dashed, and dotted lines, respectively.

solid lines in Fig. 4.2, are

$$\delta_1 = \frac{d}{2}\left(1, \sqrt{3}\right), \; \delta_2 = \frac{d}{2}\left(1, -\sqrt{3}\right), \; \delta_3 = \frac{d}{2}\left(-2, 0\right). \tag{4.3}$$

The vectors defining the second nearest neighbours in sublattice A, shown by the dashed lines, can be expressed in terms of unit vectors $\mathbf{a}_1$ and $\mathbf{a}_2$:

$$\mathbf{n}_1 = -\mathbf{n}_4 = \mathbf{a}_1, \; \mathbf{n}_2 = -\mathbf{n}_5 = \mathbf{a}_2, \; \mathbf{n}_6 = -\mathbf{n}_3 = \mathbf{a}_1 - \mathbf{a}_2. \tag{4.4}$$

Finally, the third-nearest atoms in sublattice A, shown by the dotted lines, are defined by:

$$\mathbf{m}_1 = \mathbf{n}_1 + \delta_2, \; \mathbf{m}_2 = \mathbf{n}_3 + \delta_3, \; \mathbf{m}_3 = \mathbf{n}_5 + \delta_1. \tag{4.5}$$

The choice of unit vectors and orientation of the cartesian coordinate basis is important because the form of the equation of motion for particles in such a lattice will be affected by this choice. In the published literature, for example [45], instead of $\mathbf{a}_2$ vector a vector with coordinates $d = \left(0, -\sqrt{3}\right)$ has been used. Different choice of basis will lead to different form of operators.

4.2.2 Band structure

The strong sp^2 hybridised, in-plane covalent bonds do not contribute to the transport properties of graphene, and only π orbitals oriented perpendicular to the plane

do so. In the tight-binding approximation the many-particle Hamiltonian (in the absence of magnetic field) for non-interacting quasiparticles, using up to third-nearest neighbours (see Fig. 4.2), can be written as [51, 52]

$$\begin{aligned} H^{\mathrm{tb}} = &-t \sum_{\mathbf{r}_i \in \Lambda_A} \sum_{j=1}^{3} a^\dagger(\mathbf{r}_i) b(\mathbf{r}_i + \delta_j) - t \sum_{\mathbf{r}_i \in \Lambda_B} \sum_{j=1}^{3} b^\dagger(\mathbf{r}_i) a(\mathbf{r}_i + R_I \delta_j) \\ &-t' \sum_{\mathbf{r}_i \in \Lambda_A} \sum_{j=1}^{6} a^\dagger(\mathbf{r}_i) a(\mathbf{r}_i + \mathbf{n}_j) - t' \sum_{\mathbf{r}_i \in \Lambda_B} \sum_{j=1}^{6} b^\dagger(\mathbf{r}_i) b(\mathbf{r}_i + R_I \mathbf{n}_j) \\ &-t'' \sum_{\mathbf{r}_i \in \Lambda_A} \sum_{j=1}^{3} a^\dagger(\mathbf{r}_i) b(\mathbf{r}_i + \mathbf{m}_j) - t'' \sum_{\mathbf{r}_i \in \Lambda_B} \sum_{j=1}^{3} b^\dagger(\mathbf{r}_i) a(\mathbf{r}_i + R_I \mathbf{m}_j), \end{aligned} \tag{4.6}$$

where R_I is an operator of rotation by π radians, $a^\dagger(a)$ is an electron creation (annihilation) operator on site $\mathbf{r}_i \in \Lambda_A$ and $b^\dagger(b)$ is that on site $\mathbf{r}_i \in \Lambda_B$. Index j changes from 1 to 3 for nearest neighbours and for third nearest neighbours and from 1 to 6 for third-nearest neighbours. Vectors δ_j, $\mathbf{n}_j$ $\mathbf{m}_j$ are defined by expressions 4.3, 4.4, 4.5, respectively. The parameters t, t', t'' represent the hopping energy between first, second, and third nearest neighbours respectively, and they are equal to 2.8 eV, 0.1 eV, 0.07 eV, respectively [53]. This Hamiltonian takes into account all hops between nearest neighbours in the lattice, ignoring many other contributions like disorder and smaller hopping energies for more distant sites.

We can introduce the Fourier transform of creation and annihilation operators by the following formulae:

$$\begin{aligned} a^\dagger(\mathbf{r}_i) = \frac{1}{\sqrt{N}} \sum_{\mathbf{k}} e^{-i\mathbf{k}\cdot\mathbf{r}_i} a^\dagger(\mathbf{k}),\ a(\mathbf{r}_i) = \frac{1}{\sqrt{N}} \sum_{\mathbf{k}} e^{i\mathbf{k}\cdot\mathbf{r}_i} a(\mathbf{k}), \\ b^\dagger(\mathbf{r}_i) = \frac{1}{\sqrt{N}} \sum_{\mathbf{k}} e^{-i\mathbf{k}\cdot\mathbf{r}_i} b^\dagger(\mathbf{k}),\ b(\mathbf{r}_i) = \frac{1}{\sqrt{N}} \sum_{\mathbf{k}} e^{i\mathbf{k}\cdot\mathbf{r}_i} b(\mathbf{k}), \end{aligned} \tag{4.7}$$

where N is the number of sites in sublattice A or B. If we substitute Eq. 4.7 into Eq. 4.6 we have

$$H^{\mathrm{tb}} = -\sum_k \begin{pmatrix} a^\dagger(\mathbf{k}) & b^\dagger(\mathbf{k}) \end{pmatrix} \begin{pmatrix} \phi'(\mathbf{k}) & \phi(\mathbf{k}) + \phi''(\mathbf{k}) \\ \phi^*(\mathbf{k}) + \phi''^*(\mathbf{k}) & \phi'^*(\mathbf{k}) \end{pmatrix} \begin{pmatrix} a(\mathbf{k}) \\ b(\mathbf{k}) \end{pmatrix}, \tag{4.8}$$

where

$$\phi(\mathbf{k}) = t\sum_{j=1}^{3} e^{i\mathbf{k}\cdot\delta_j},\ \phi'(\mathbf{k}) = t'\sum_{j=1}^{6} e^{i\mathbf{k}\cdot\mathbf{n}_j},\ \phi''(\mathbf{k}) = t''\sum_{j=1}^{3} e^{i\mathbf{k}\cdot\mathbf{m}_j}. \tag{4.9}$$

Here we have used the definition of the delta function

$$\delta(\mathbf{k}-\mathbf{k}') = \frac{1}{N}\sum_{\mathbf{r}_i\in\Lambda_A} e^{i\mathbf{k}'\mathbf{r}_i - i\mathbf{k}\mathbf{r}_i}.$$

Using Eq. 4.8 the dispersion relation $\varepsilon(\mathbf{k})$ for the charge carriers is calculated from the condition on the determinant

$$\begin{vmatrix} \phi'(\mathbf{k})+\varepsilon(\mathbf{k}) & \phi(\mathbf{k})+\phi''(\mathbf{k}) \\ \phi^*(\mathbf{k})+\phi''^*(\mathbf{k}) & \phi'^*(\mathbf{k})+\varepsilon(\mathbf{k}) \end{vmatrix} = 0. \tag{4.10}$$

By solving this quadratic equation the energy of carriers is

$$\varepsilon_{1,2}(\mathbf{k}) = -\Re\phi'(\mathbf{k}) \pm \sqrt{|\phi(\mathbf{k})+\phi''(\mathbf{k})|^2 - \Im\phi'(\mathbf{k})^2}. \tag{4.11}$$

where $\Re\phi'(\mathbf{k})$ and $\Im\phi'(\mathbf{k})$ are real and imaginary part of $\phi'(\mathbf{k})$, respectively. The positive sign corresponds to the conduction band and negative to the valence band. The latter expression can be simplified because imaginary part is cancels and the final result for the dispersion relation is

$$\varepsilon_{1,2}(\mathbf{k}) = -\phi'(\mathbf{k}) \pm \sqrt{|\phi(\mathbf{k})+\phi''(\mathbf{k})|^2}.$$

A simpler approximation used in the literature, when $|\phi| \ll |\phi'|$ and $|\phi| \ll |\phi''|$, is

$$E_{1,2}(\mathbf{k}) = \pm|\phi(\mathbf{k})|. \tag{4.12}$$

It takes into account the nearest neighbours only.

4.2.3 Effective Dirac equation

There are six points in the corners of Brillouin zone where the conduction band touches the valence band, called Dirac points:

$$\left(0, \pm\frac{4\pi}{3\sqrt{3}d}\right),\ \left(\frac{2\pi}{3d}, \pm\frac{2\pi}{3\sqrt{3}d}\right),\ \left(-\frac{2\pi}{3d}, \pm\frac{2\pi}{3\sqrt{3}d}\right). \tag{4.13}$$

The dispersion relation is linear around these points. There are two inequivalent Dirac points $K^+ = \left(0, \frac{4\pi}{3\sqrt{3}d}\right)$ and $K^- = \left(0, -\frac{4\pi}{3\sqrt{3}d}\right)$, which we choose in the opposite points in the first Brillouin zone defined as shown in Fig. 4.3. We can rewrite the tight-binding Hamiltonian (4.8) for nearest neighbours in the vicinity of K^+ and K^- points [54]as

$$H_1^{\mathrm{tb}+} \simeq \hbar v_F \sum_k \Psi^\dagger_{K^+}(\kappa) \begin{pmatrix} 0 & i\kappa_x + \kappa_y \\ -i\kappa_x + \kappa_y & 0 \end{pmatrix} \Psi_{K^+}(\kappa), \tag{4.14}$$

$$H_1^{\mathrm{tb}-} \simeq \hbar v_F \sum_k \Psi^\dagger_{K^-}(\kappa) \begin{pmatrix} 0 & i\kappa_x - \kappa_y \\ -i\kappa_x - \kappa_y & 0 \end{pmatrix} \Psi_{K^-}(\kappa), \tag{4.15}$$

where $v_F = 3td/2$ is a Fermi velocity. If we consider all contributions from nearest neighbours, the following expression will appear in the first order expansion of Eq. 4.8 for a single particle by a wavevector near the Dirac points K^+, K^-:

$$\tilde{H}_1^{\mathrm{tb}\pm} = \begin{pmatrix} 3t' & \hbar v_F^*(i\kappa_x \pm \kappa_y) \\ \hbar v_F^*(-i\kappa_x \pm \kappa_y) & 3t' \end{pmatrix}, \tag{4.16}$$

where the Fermi velocity is renormalised due to the presence of third neighbour hopping integral t'' as $v_F^* = 3d(t - 2t'')/2$, and $\pm$ indexes correspond to a specific Dirac point $K^\pm$. The second order expansion gives

$$\tilde{H}_2^{\mathrm{tb}\pm} = \begin{pmatrix} -\frac{9}{4}d^2t'(\kappa_x^2 + \kappa_y^2) & \alpha(\kappa_x \pm i\kappa_y)^2 \\ \alpha(\kappa_x \mp i\kappa_y)^2 & -\frac{9}{4}d^2t'(\kappa_x^2 + \kappa_y^2) \end{pmatrix}, \tag{4.17}$$

where $\alpha = 3\hbar t(1 + 4t''/t)d^2/8$. The diagonal terms of the Hamiltonian change the position of the Fermi energy and break the symmetry between holes and electrons can be absorbed in the chemical potential [51] as an additional term which shifts the Fermi energy. These terms have circular symmetry and change slightly the slope of the dispersion relation, but off-diagonal terms distort the spectrum and are responsible for 'trigonal warping' [55], so-called because of the triangular shape of the Fermi surface. The resulting dispersion relations for electrons and holes are

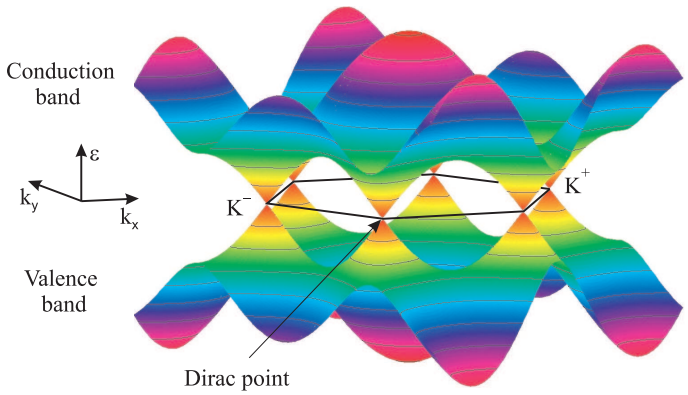

Figure 4.3: Band diagram for graphene in the nearest neighbours approximation described by Eq. 4.12. Two nonequivalent Dirac points (K^- and K^+) are shown.

given by the following expressions with second order in κ:

$$\varepsilon_e^{K^\pm} = 3t' + \hbar v_F^* \sqrt{\kappa_x^2 + \kappa_y^2} - \frac{9}{4} d^2 t' (\kappa_x^2 + \kappa_y^2) \pm \frac{\alpha \kappa_y}{\sqrt{\kappa_x^2 + \kappa_y^2}} (3\kappa_x^2 - \kappa_y^2),$$

$$\varepsilon_h^{K^\pm} = 3t' - \hbar v_F^* \sqrt{\kappa_x^2 + \kappa_y^2} - \frac{9}{4} d^2 t' (\kappa_x^2 + \kappa_y^2) \mp \frac{\alpha \kappa_y}{\sqrt{\kappa_x^2 + \kappa_y^2}} (3\kappa_x^2 - \kappa_y^2).$$

4.2.4 Rotation

A rotation of the coordinate system in Fig. 4.1 by an angle η changes the form of the Dirac equation, but should not change the dispersion relation. Thus, a phase factor can be added to the Dirac Hamiltonian to account for this. Calculations show that a single-particle Hamiltonian changes under rotation by an angle η as [55]

$$H^\pm = \hbar v_F \begin{pmatrix} 0 & e^{\pm i\eta}(i\kappa_x \pm \kappa_y) \\ e^{\mp i\eta}(-i\kappa_x \pm i\kappa_y) & 0 \end{pmatrix}, \tag{4.18}$$

From this Hamiltonian, other Hamiltonians used in literature can be obtained. For example, it can be transformed to a most common form when the rotation by $-\pi/2$ is made [52]:

$$H = \hbar v_F \begin{pmatrix} 0 & \kappa_x - i\kappa_y & 0 & 0 \\ \kappa_x + i\kappa_y & 0 & 0 & 0 \\ 0 & 0 & 0 & -\kappa_x + i\kappa_y \\ 0 & 0 & -\kappa_x - i\kappa_y & 0 \end{pmatrix}. \tag{4.19}$$

where we exchange the sublattices $A \longrightarrow B$ in the spinor for the K^- Dirac point in order to use a simple form for the Dirac equation

$$H^{\pm}\psi^{\pm} = \pm\hbar v_F(\sigma_1\kappa_1 + \sigma_2\kappa_2)\psi^{\pm} = \varepsilon\psi^{\pm}, \tag{4.20}$$

where σ_1 and σ_2 are Pauli matrixes and $\psi^{\pm}$ are spinor wavefunctions for the two valleys.

4.2.5 Chirality

The wavefunctions for $K^{\pm}$ points can be found by solving equation (4.20) as

$$\begin{aligned}
\psi_e^{K^{\pm}} &= \frac{1}{\sqrt{2}} \begin{pmatrix} 1 \\ \pm\frac{\kappa_x + i\kappa_y}{\sqrt{\kappa_x^2+\kappa_y^2}} \end{pmatrix}, \\
\psi_h^{K^{\pm}} &= \frac{1}{\sqrt{2}} \begin{pmatrix} \pm\frac{-\kappa_x + i\kappa_y}{\sqrt{\kappa_x^2+\kappa_y^2}} \\ 1 \end{pmatrix},
\end{aligned} \tag{4.21}$$

where indexes e and h correspond to electrons and holes, respectively. One can construct a pseudochirality operator [52] defined as

$$\hat{h} = \frac{\kappa_x\sigma_x + \kappa_y\sigma_y}{\sqrt{\kappa_x^2 + \kappa_y^2}}, \tag{4.22}$$

which has a specific eigenvalue if it acts on the wavefunctions in Eq. (4.21). Namely,

$$\hat{h}\psi_e^{K^{\pm}} = \pm\psi_e^{K^{\pm}},\ \hat{h}\psi_h^{K^{\pm}} = \mp\psi_h^{K^{\pm}}, \tag{4.23}$$

where electrons and holes have opposite sign eigenvalue (chirality) in both valleys. Electrons have $+1$ chirality in the K^+ valley and -1 chirality for the K^- Dirac point. Conservation of this quantum number plays an important role in transport properties of quasiparticles in graphene discussed in the next section.

4.3 Transport properties

Graphene is a semiconductor with zero band gap. When the resistance of graphene placed on top of SiO_2 is measured as a function of gate voltage, a single peak of

large but finite resistance is observed. The Fermi energy (or gate voltage) at which this peak occurs is called the Dirac or electroneutrality point. In ideal graphene without doping the Fermi level should lie at the Dirac point (zero gate voltage) if the dispersion relation is symmetric with respect to zero energy (crossing points). This is correct only if transfer integrals to nearest neighbours are taken into account. Doping shifts the Fermi level and thus the resistance peak from the zero gate voltage position.

It has been observed experimentally that the resistance at the Dirac point is not infinite (as one can expect because of zero concentration of free charge carriers) but finite. Many samples have approximately the same resistivity in the Dirac point, $h/4e^2$. This can be due to layer of water formed during the mechanical cleavage. The closeness of the value of the resistivity to $h/4e^2$ in the Dirac point has suggested it is a universal value [56]. However, it was recently shown that the amplitude of the Dirac peak as well as mobility depends on doping and decreases [57] due to scattering on Coulomb impurities. The amplitude of the peak is roughly independent of temperature [58], but only in the case of graphene on Si/SiO_2 substrate. Since transport measurements of free standing graphene have been carried out, it has been shown that the peak resistivity is not universal and has temperature dependence [59].

The Dirac point has more complications because at small carrier density graphene becomes inhomogeneous due to disorder and electron-hole puddles are formed [60]. However, for transport properties in the diffusive regime not close to the Dirac point, a standard Boltzmann transport equation is used [61]. The applicability of the Boltzmann approach fails only close to the Dirac point where the wavelength tends to infinity (because the energy goes to zero). Due to chirality of the carriers in graphene the collision integral has to be revised, because this property prohibits backscattering, as has been shown in all orders of perturbation theory by Ando [62].

The conductivity is given by the conventional formula

$$\sigma = ne\mu, \tag{4.24}$$

where n is the concentration of mobile carriers, e is elementary charge, and mobility μ is given by [21]

$$\mu = \frac{ev_F^2}{\varepsilon_F}\tau(\varepsilon_F). \tag{4.25}$$

The relaxation time $\tau(\varepsilon_F)$ is given by the collision integral [61]

$$\frac{\hbar}{\tau(\varepsilon_F)} = 2\pi \int \frac{d^2\kappa'}{(2\pi)^2} \langle |V_{\kappa,\kappa'}|^2 \rangle (1 - \cos(\theta_\kappa - \theta_{\kappa'})) \delta(\varepsilon_\kappa - \varepsilon_{\kappa'}), \tag{4.26}$$

where $\theta_\kappa - \theta_{\kappa'}$ is an angle between incident κ and scattered κ' wavevectors, $\delta(\varepsilon_\kappa - \varepsilon_{\kappa'})$ is the Delta function, and $\langle |V_{\kappa,\kappa'}|^2 \rangle$ is the average of the scattering potential matrix element in momentum space over the distribution of scatters. The latter is changed with the type of the defects that create the scattering potential. There are two main defects in the lattice which are considered by theoreticians using the Born approximation: short range disorder and Coulomb impurities [61].

Coulomb impurities are the most important source of scattering as they determine the constant mobility of graphene at high gate voltages (far from the Dirac point) [61]. By replacing the Cartesian coordinate system with a polar one and performing integration over energy in Eq. (4.26) we arrive at the expression

$$\frac{\hbar}{\tau(\varepsilon_F)} = 2\pi n_i D(\varepsilon_F) \int_0^\pi \frac{d\theta}{2\pi} (1 - \cos(\theta))(1 + \cos(\theta)) \left(\frac{2\pi e^2}{\kappa q \varepsilon(q)} \right)^2, \tag{4.27}$$

where $D(\varepsilon_F)$ is density of states in graphene at the Fermi energy, n_i is the concentration of impurities (about 10^{12} cm^{-2} for thermally oxidised Si), $q = 2\varepsilon/\gamma \sin\theta/2$, γ is the band parameter equal to 6.5 eV·Å [61]. The factor $(1 + \cos(\theta))$ in the integral comes from the chirality of the particles which prohibits backscattering. The latter integral can be evaluated and the conductivity due to scattering on Coulomb impurities becomes

$$\sigma_0 = \frac{e^2}{4\pi^2\hbar} \frac{n}{n_i} H_0, \tag{4.28}$$

where H_0 is a constant, and n is carrier concentration. This expression is linear as a function of carrier concentration and it shows that the mobility is independent of concentration.

For short range scatterers the picture is completely different. A short range impurity is the one that acts on a particle only in a range less than the carbon-carbon distance and is near an A or B site in the crystal lattice. The presence of such an impurity means that the electron has different energies when it localised on A site or on B site and the conditions for the applicability of a continuum model (Dirac equation) with independent Dirac points are not satisfied [62]. It has been

shown that the conductivity for short range scatterers is independent of energy [63]. Physically, this can be explained as follow. According to the Fermi's golden rule $1/\tau \propto \langle |V_{\kappa,\kappa'}|^2 \rangle D(E_F)$, where $D(E_F) \propto E$. Thus, the mobility is inversely proportional to the carrier concentration, $\mu \propto n^{-1}$ and the conductivity is independent of the Fermi energy.

The total resistance can be viewed as a sum of two contributions: from scattering on short range impurities ρ^S (lattice defects or screened Coulomb potential) and long-range ρ^L (for example, nonscreened Coulomb potential). As soon as scattering on Coulomb impurities is avoided (by suspending graphene over silicon dioxide) the mobility can increase to 2×10^5 cm^2 V^{-1} s^{-1} [59] because of the large intrinsic mobility [58] related to internal (phonons) scattering processes. This large mobility can be useful for production of ballistic structures to study some effects specific to graphene. But there is another way to study ballistic transport in graphene, by producing a sample that is small compared to the mean free path (or measure transport in a small part of a larger sample) or producing a *p*-*n* junction.

4.3.1 *p*-*n* junction

A *p*-*n* junction can be created in a graphene flake by a top-gate. The top-gate can change locally not only the conductance of graphene but also the type of carrier, from electrons to holes or vice versa. By applying to the top-gate opposite to the back-gate polarity under the top-gate one can have an electron region, while away from the top-gate holes can be the charge carriers. Top gates have already been made using a dielectric between the graphene flake and the gate [64–68].

Graphene is considered as a promising material for future electronic applications. However, to replace the silicon technology graphene needs to overcome a serious limitation. Because graphene is a semiconductor with zero band gap, the transistors have leakage current and just producing top-gate is not enough to make a working transistor. One of the possible ways to produce a band gap and reduce leakage is to make a narrow ribbon about 10 nm width. In this case the spectrum of carries is broken into several quantized subbands and a band gap between the lowest electron subband and the highest hole subband is formed.

The type of dielectric between the top-gate and the graphene flake strongly

affects the mobility of the carriers [65]. If the mobility is small, ballistic effects will be suppressed. One of the possible solutions of this problem is to avoid the use of a dielectric but make a suspended top-gate [69].

Due to the chirality of carriers, transport through a p-n junction in graphene has its own specifics. The case of a rapid change of the potential in the p-n junction is discussed in [46]. It has also been shown that ballistic quasiparticles can penetrate a p-n junction without reflection at zero angle of incidence. At other angles there is a probability for carriers to be scattered back. This result has been extended to any smooth potential including a linear one where the quasiclassical approximation is applicable [43].

A p-n junction can be diffusive, when there are scatterers in the region of the p-n junction or ballistic when there are no scatterers there. In the first case, to predict the resistance of the p-n junction a diffusive transport model should be used. In the diffusive transport model the probability of the carriers to penetrate through the p-n junction is independent of the angle of incidence, but in the case of ballistic transport the theory by [43] should be applied. Due to the reflection at other than zero degree angles, the resistance of a ballistic p-n junction in graphene is larger than a diffusive one. This excess resistance above the prediction of the diffusive model in a graphene structure with a p-n junction was observed in [65].

4.3.2 Ballistic transport in a p-n junction

Cheianov and Fal'ko [43] have studied penetration of chiral particles through ballistic p-n junctions with a linear energy barrier as a function of coordinate x (in the current direction):

$$u(x) = Fx, \tag{4.29}$$

where F is an energy gradient. F is the main parameter which affects the transmission coefficient through the p-n junction and thus its resistance.Ballistic transport through p-n junction means that electrons which approach the boundary of a p-n junction penetrate from the p region into the n region without scattering on impurities or defects. If the particle has a nonzero κ_y wave vector-component, there is a region of classically unreachable space which the particle can penetrate only via tunnelling (see Fig. 4.4). The total energy of electrons (with the assumption that

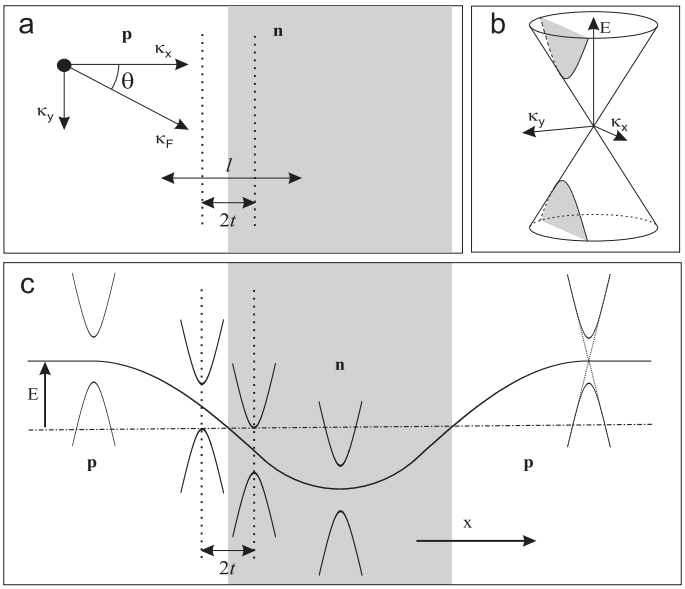

Figure 4.4: (a) Momentum of an electron approaching a p-n junction at an angle θ. (b) The gap in the spectrum $E(\kappa_x)$ (highlighted) at $\theta \neq 0$. (c) Band-structure profile along the length of the p-n-p structure. The value of the gap determines the tunneling length $2t(2\theta)$.

graphene is undoped) is

$$\varepsilon_{tot} = \pm\hbar v_F \sqrt{\kappa_x^2 + \kappa_y^2} + u(x), \tag{4.30}$$

where $u(x)$ is the (in general, not linear) electrostatic potential energy produced by the gates, or, in other words, the position of electroneutrality point. If the total energy is assumed to be zero, then the momentum of a particle along the direction of propagation is described by the following relation:

$$\kappa_x(x) = \pm\frac{1}{\hbar v_F}\sqrt{u(x)^2 - \hbar^2\kappa_y^2 v_F^2} = \pm\frac{1}{\hbar v_F}\sqrt{u(x)^2 - \varepsilon_F^2 \sin^2\theta}, \tag{4.31}$$

where ε_F is the Fermi energy in the contacts.

At finite angles, there is a region where momentum has a complex value (this is a classically unreachable region). The turning points $\pm t$ in space where the total momentum is equal to zero are obtained by solving the following equation:

$$u(\pm t) = \pm\varepsilon_F \sin\theta. \tag{4.32}$$

A semiclassical model for tunnelling [70] tells us that the probability of penetration

through a long and high potential barrier is described by the expression

$$w_{pn}^{exact}(\theta) \sim e^{-2S/\hbar} = \exp\left(-2\int_{-l}^{l}|\kappa_x(x)|dx\right). \tag{4.33}$$

Here S is action. In general, the probability has to be small compared to unity to make this quasiclassical model applicable, but Cheianov and Fal'ko have proved, using a transfer matrix formalism, that this formula with a coefficient calculated can be used to obtain the total angular dependance of probability of tunnelling. Conductance of the p-n junction per unit width is given by

$$G_{np} = \frac{4e^2}{h}\int \frac{d\kappa_y}{2W\pi} w_{pn}^{exact}(\theta) = \frac{4e^2}{h}\int \frac{Wk_F\cos\theta d\theta}{2\pi} w_{pn}^{exact}(\theta), \tag{4.34}$$

where W is the width of the sample. For small angles (where the transmission is not small) Eq. 4.34 can be simplified and the conductance of a p-n junction can be calculated analytically (by integrating over the range of θ from $-\infty$ to $+\infty$):

$$G_{np} = \frac{2e^2}{\pi h} W\sqrt{\frac{F}{\hbar v_F}}. \tag{4.35}$$

One can see that the conductance is independent of the Fermi energy. In a real sample, to see ballistic transport through a p-n junction we have to have the mean free path l larger than tunnelling distance $2t$, as shown in Fig. 4.4(a). An effective band gap appears if the quasiparticle approaches the p-n junction at a non-zero angle, due to a finite y component of the wavevector, Fig. 4.4(b). In this case there is a region of the p-n junction where the quasiparticle has an imaginary wavevector: this region has length $2t$ and depends on angle θ (Fig. 4.4(c)).

4.3.3 Ballistic transport in a p-n-p junction

Katsnelson [46] has discussed ballistic transport through a rectangular potential barrier in graphene. It was predicted that a particle approaching with normal incidence to a rapid barrier has perfect transmission, without backscattering for any height of the barrier. This has an analogy in high-energy physics called "the Klein paradox". The effect has not yet been observed experimentally.

The model of transport through a rectangular barrier is formed on the basis

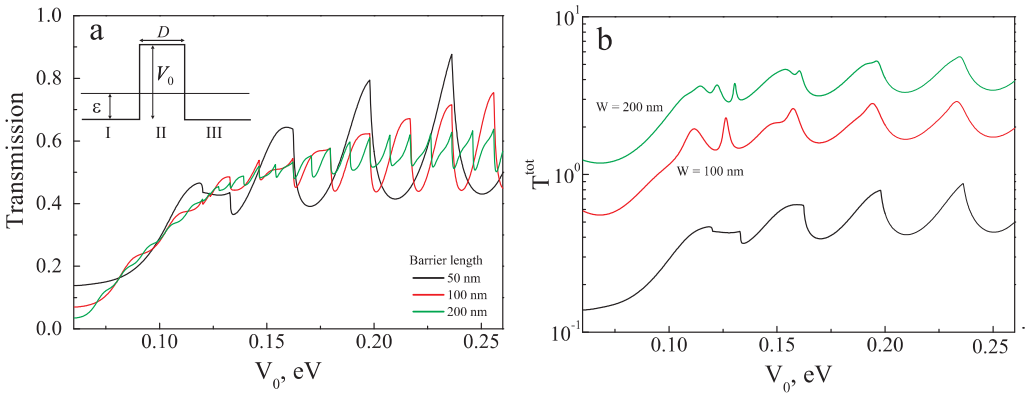

Figure 4.5: Total transmission as a function of height of a rectangular barrier. (a) Different lengths of the barrier, using Eq. (4.40) for a single channel. Energy of electrons ε=0.06 eV. The model potential $u(x)$ is shown in the top left inset. (b) Influence of the finite width of the ribbon for 50 nm barrier length. T^{tot} for a single channel, 100 nm, and 200 nm width is presented.

of a low energy effective Dirac Hamiltonian (Eq. 4.19). The barrier region with potential of height V_0 should have a Hamiltonian with an additional term: namely, the Hamiltonian for the K^+ valley with an external potential $u(x)$ can be written as:

$$\hat{H} = -i\hbar v_F \sigma \cdot \nabla + u(x), \tag{4.36}$$

where $\hbar$ is Plank's constant, v_F is Fermi velocity, $\sigma = (\sigma_x, \sigma_y)$ is a vector consisting of Pauli matrixes, and $\nabla = (\nabla_x, \nabla_y)$ is a gradient operator. The potential is different for the three regions shown in the inset in Fig. 4.5(a):

$$u(x) = \begin{cases} V_0, & 0 < x < \text{ D, region II} \\ 0, & \text{otherwise, regions I and III} \end{cases}.$$

Let D be the width of the barrier and ε the energy of a particle. Then if we divide the space of the problem into three regions, we can write the solution of Dirac equation for each region as

$$\psi_I(\mathbf{r}) = \frac{1}{\sqrt{2}} \begin{pmatrix} 1 \\ se^{i\phi} \end{pmatrix} e^{i(k_x x + k_y y)} + \frac{r}{\sqrt{2}} \begin{pmatrix} 1 \\ se^{i(\pi-\phi)} \end{pmatrix} e^{i(-k_x x + k_y y)}, \tag{4.37}$$

$$\psi_{II}(\mathbf{r}) = \frac{a}{\sqrt{2}} \begin{pmatrix} 1 \\ s' e^{i\theta} \end{pmatrix} e^{i(q_x x + k_y y)} + \frac{b}{\sqrt{2}} \begin{pmatrix} 1 \\ s' e^{i(\pi-\theta)} \end{pmatrix} e^{i(-q_x x + k_y y)}, \tag{4.38}$$

$$\psi_{III}(\mathbf{r}) = \frac{t}{\sqrt{2}} \begin{pmatrix} 1 \\ s e^{i\phi} \end{pmatrix} e^{i(k_x x + k_y y)}, \tag{4.39}$$

where $\phi = \arctan(k_y/k_x)$, $\theta = \arctan(k_y/q_x)$, and wavevectors in the region I and III are equal to $k_x = k_F \cos\phi$, $k_y = k_F \sin\phi$, for the region II under the barrier the wavevector is $q_x = \sqrt{(V_0 - \varepsilon)^2/v_F^2 - k_y^2}$, $s = \text{sign}(\varepsilon)$ and $s' = \text{sign}(\varepsilon - V_0)$. There are two unknown coefficients, r and t, which should be determined from the conditions of continuity of the wave function at the boundaries of the rectangular potential. By solving this problem the expression for the transmission probability as a function of angle is calculated [53] as

$$T(\phi) = \frac{\cos^2\theta \cos^2\phi}{[\cos(Dq_x)\cos\phi\cos\theta]^2 + \sin^2(Dq_x)[1 - ss'\sin\phi\sin\theta]^2}. \tag{4.40}$$

Using this expression, the dependence of transmission on the height of barrier has been plotted in Fig. 4.5(a). The form of the transmission for a single channel has an oscillatory behavior as a function of height of the barrier, which follows from the interference of transmitted and reflected waves within the barrier. In Fig. 4.5(a) three lengths of the barrier are shown to demonstrate that the period of oscillations as well as their amplitude decrease with increasing length. However, for a narrow sample the calculation of the transmission should be revised because of the finite number of propagating modes. The component of the wavevector parallel to the barrier takes only quantised values which are determined by the width of the sample and boundary conditions for an ideal ribbon [71]. The values are

$$\kappa_n = \left(n + \frac{1}{2}\right)\frac{\pi}{W},\ n = 0, 1, 2, ..., \tag{4.41}$$

where W is width of the sample. Thus, the total conductance is calculated from the sum of the transmission probabilities of individual modes with wavevectors less

than the Fermi wavevector

$$G = \frac{4e^2}{h} T^{tot} = \frac{4e^2}{h} \sum_{n=0}^{N-1} T_n, \tag{4.42}$$

where N is total number of propagating modes. If we consider a finite width of the ribbon, for example, 100 nm or 200 nm (see Fig. 4.5(b)), the relative amplitude of the oscillations is conserved. The variation of the resistance is about 20 %.

In section 4.4.4, we will use this model for comparison with an experiment which has been performed on top-gate graphene structures.

4.4 Experiment and analysis

4.4.1 Overview of the experimental results

The data and analysis for three two-terminal graphene samples with 'air-bridge' top-gates are presented. The samples were fabricated by Roman Gorbachev from the laboratory of Quantum Transport in Nanostructures at Exeter University using the technology discussed in Section 2.2.3. Details of these samples are given in Table 4.1. The third sample S3 has been measured by the author and the data for the first and second samples (S1 and S2 respectively) are provided by Roman Gorbachev. The resistivity dependence on back-gate voltage for these three samples is shown in Fig. 4.6(a). The samples have different mobilities, and it was expected that the first sample, with the largest mobility, has to show some features of ballistic transport through a p-n junction formed by the top-gate. (In this sample the mean free path becomes comparable to the gate length.)

The top-gate dependence at fixed back-gate voltages for the three studied samples are shown in Fig. 4.6(b-d). On the same graphs the expected resistance as a function of top-gate voltage is shown assuming purely diffusive transport dominates (see Section 4.4.2). The difference between experiment and predictions are clearly seen on the graphs.

We attribute the difference between experiment and diffusive theory to the ballistic transport through the two p-n junctions (but not through the whole p-n-p structure) formed by the top-gate. To calculate the expected value for the resis-

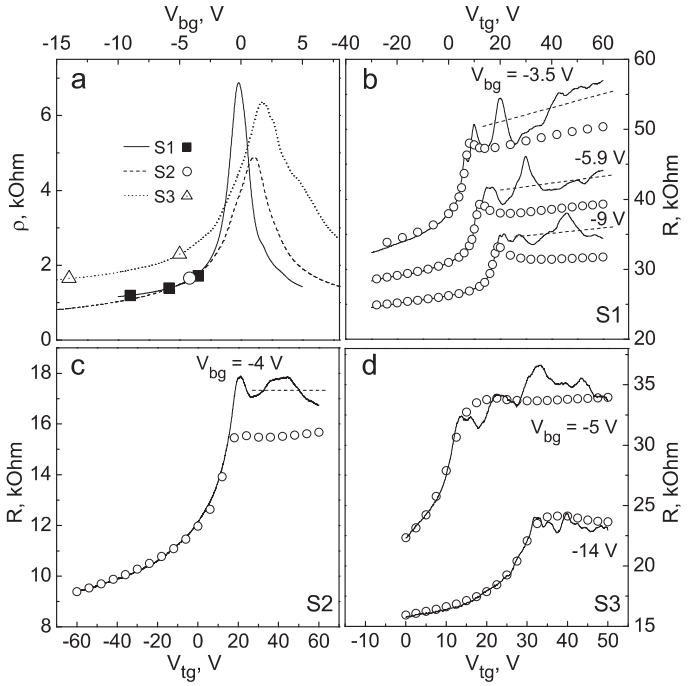

Figure 4.6: (a) Resistivity of the three samples as a function of the back-gate voltage, at $V_{tg} = 0$, at $T = 50$ K. Points indicate the values of V_{bg} where the top-gate voltage was swept to produce *p*-*n*-*p* junctions. (b) The resistance of sample S1 as a function of top-gate voltage at different V_{bg}. (c,d) The resistance as a function of top-gate voltage at different V_{bg} of samples S2 and S3, respectively. Points show the results of the calculations of the expected resistance assuming diffusive transport of carriers. (Dashed lines in b,c are guides to the eye.)

tance of a single *p*-*n* junction we have used theory [43] as described earlier (4.3.2). This resistance is determined by the energy gradient F in the middle of the junction. To find the energy profile, the density of states in graphene should be taken into account. This has been done by solving the 2D electrostatic problem with correct boundary conditions on graphene, as discussed in Section 4.4.2. The results of these calculations are presented in Table 4.1 (last two entries).

Characteristics	S1	S2	S3
Width, μm	0.3-0.15	0.6	0.15
Length, μm	5	4.3	1.45
Dirac point, V	0.05	1.11	1.68
Resistivity in Dirac point, kOhm	6.9	4.87	6.36
Mean free path, nm	100	75	45
Top-gate length, nm	170	170	100
Top-gate distance, nm	140	210	130
Resistance difference, kOhm	3.8 (-9 V)	-1.82 (-4 V)	0 (-14 V)
Efficiency of top-gate	0.35	0.24	0.4
Energy gradient, eV/m	$1.5 \cdot 10^6$	$0.8 \cdot 10^6$	$2.4 \cdot 10^6$
Mobility, $cm^2V^{-1}s^{-1}$ (n=$3{\cdot}10^{11}$ cm^{-2})	12.5	11	6-7
Fermi wave vector, 10^7 m^{-1}	6.5	3.4	5.87
Fermi energy, eV	0.043	0.0225	0.038
Fermi wavelength, nm	96	188	109
Critical angle	~ 25	~ 25	~ 30
Critical tunnelling distance	~ 40	~ 40	~ 40
Number of modes	7	11	3
Resistance, kOhm (diffusive model)	2.17	0.62	1.85
Resistance, kOhm (Cheianov model)	3.6	1.95	4.4

Table 4.1: Parameters of graphene samples with 'air-bridge' top-gates.

For sample S3, the resistance as a function of back and top-gate voltage, temperature and magnetic field has been measured (see Fig. 4.7). The colour scale (4.7(a)) indicates the efficiency of the top-gate (how the energy changes with voltage) by the slope of the dashed line, which shows the position of the peak in the resistance corresponded to formation of two *p-n* junctions. The efficiency is equal to 0.4, which makes the distance between the flake and top-gate found by modelling (for details see Section 4.4.2) the smallest out of the three samples. This creates the narrowest *p-n-p* junction in graphene. To see how ballistic the junction is, we need to estimate the mean free path. Using the standard formula for conductivity

$$\sigma = \frac{2e^2}{h}\kappa_F l, \tag{4.43}$$

and taking into account that $\kappa_F = \varepsilon_F/\hbar v_F = \pm 31\,\mathrm{meV}\sqrt{|V_{bg}|}/\hbar v_F$ (where V_{bg} is given in V) the mean free path

$$l = 2.7 \cdot 10^{-4}\frac{\sigma}{\sqrt{|V_g|}}([\mathrm{m}]). \tag{4.44}$$

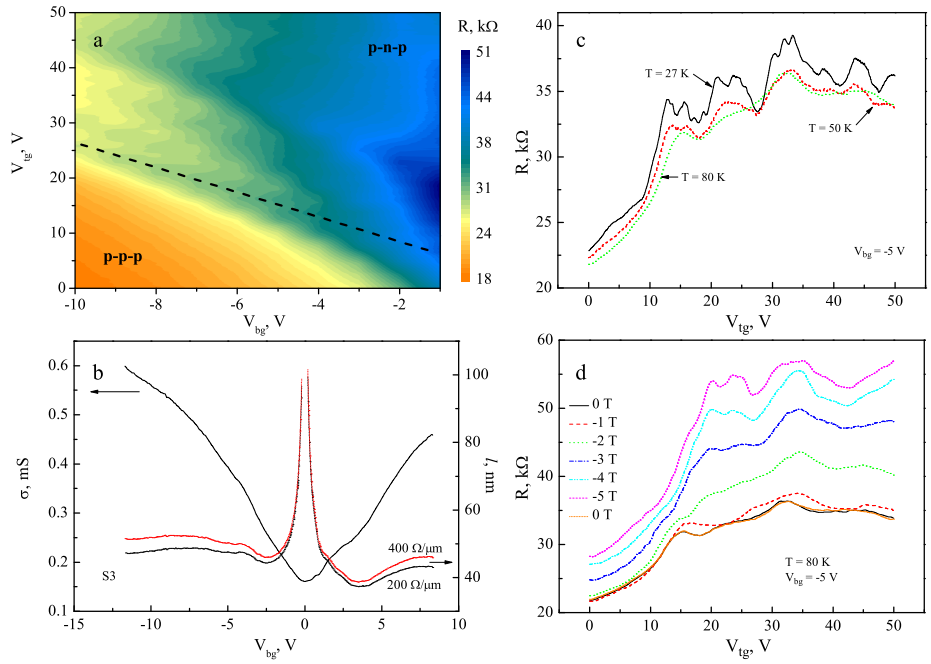

Figure 4.7: Sample S3. (a) Colour-scale of the resistance as a function of top-gate voltage and back-gate voltage at T=50 K. The dashed line shows the position of the Dirac point under the top-gate and separates the p-p-p region from the region where the *p-n-p* junction is formed. (b) Conductivity and mean free path as a function of back-gate voltage at T = 50 K. The mean free path is calculated for two different contact resistances 200 Ω/μm and 400 Ω/μm. (c) Temperature dependence of the resistance fluctuations as a function of top-gate voltage. (d) Resistance as a function of top-gate voltage at T = 80 K for different magnetic fields perpendicular to the flake. The orange curve shows reproducibility of the result.

In Fig. 4.7(b) the conductivity and mean free path as a function of back-gate voltage for different contact resistances are shown. (Here the Dirac point is shifted to zero back-gate voltage.) The total measured resistance also includes the contact resistance between the flake and the two ohmic contacts. This contact resistance should be subtracted before calculation of the mean free path. Typical values of 200 Ω/μm for two-terminal graphene samples have been determined by comparison of the values of the resistance in quantum Hall plateaux with the expected ones [24]. The mean free path of sample S3 is smaller than that of S1 and S2 and is equal to 45 nm for the electron region and 50 nm for the hole region. It decreases slightly with decreasing back-gate voltage, but increases dramatically near the Dirac point due to the divergence which occurs at zero concentration. (In reality the concentra-

tion of the carriers in the Dirac point is not zero, because of strong inhomogeneity and formation of electron-hole puddles [60], hence the simple formula (4.43) is not applicable in this region.) Thus, the increase of the mobility near the Dirac point can be an artefact of using incorrect relation.

In Fig. 4.7(c) the resistance as a function of top-gate voltage is presented for three temperatures (27 K, 50 K, 80 K). The first peak appears at $V_{tg} = 13$ V, when two p-n junctions are formed. The resistivities of the two p-n junctions are higher than that in other regions of the structure – this is the reason for the resistance increase. If the top-gate voltage increases further, no big change of the resistance of the structure at the formation of p-n junctions is seen. In this V_{tg}-range the resistance has shown reproducible fluctuations as a function of top-gate voltage. These fluctuations have a smaller "period" and larger amplitude at low temperatures. We can suggest several reasons for these fluctuations. The first is mesoscopic resistance fluctuations, as seen in normal small MOSFET samples at low carrier densities [29]. The second reason is a variation of unintentional doping in the flake which results in different position of the Dirac point under the top-gate. In this case each resistance peak corresponds to different Dirac points. Non-uniformity of the structure can be caused by non-uniformity of the top-gate itself. Instead of a constant height across the flake, the gate can contain areas with different distances from the flake. Then, even if the 2D gas is homogenous, the efficiency of different parts of the top-gate becomes a function of x-coordinate. The third reason is ballistic transport through the whole p-n-p structure which can produce oscillations in the resistance as a function of top-gate voltage. This latter reason can be only applicable near the onset of p-n-p structure where the length of the n-region can be comparable to the mean free path.

In Fig. 4.7(d) the resistance as a function of top-gate voltage at $V_{bg} = -5$ V measured at $T = 80$ K is shown for different fixed magnetic fields up to 5 T. It is seen that the positive magnetoresistance is significantly stronger at large V_{tg} when a p-n-p structure is formed. We attribute this magnetoresistance to geometric magnetoresistance discussed in Section 4.4.5.

In the following subsections we introduce our electrostatic model and apply the theory of ballistic transport through p-n and p-n-p junctions to explain the experimental results.

4.4.2 Electrostatic model

To find the resistance of a graphene flake at any voltage applied to the back-gate and top-gate we have to know the distribution of the electrostatic potential along the flake. Then, using the known relation between this potential and the back-gate voltage, we can find the resistivity at a point along the flake for a specific value of electrostatic energy. Finally, assuming a simple diffusive model, we can integrate the resistivity over the length to obtain the total resistance of the sample or any part of the *p*-*n*-*p* structure.

Solution of 3D electrostatic problem is complicated and time consuming, and we have chosen a simple 2D model for our numerical calculations. We have assumed that the sample has infinite size in the direction perpendicular to the current. This assumption should not affect the final result as long as edge effects can be neglected. The 2D coordinate system has the coordinate x along the length of the sample in the direction of the current flow and z is the vertical coordinate perpendicular to the flake.

The geometry of the electrostatic model is shown in Fig. 4.8. The total region of the calculations is taken to be large enough to exclude the influence of the boundary conditions at the outer boundaries: in this case the potential in the flake does not depend on the boundary conditions on the "box". The length of the calculated region is 25 μm and its height is 6 μm. (It was tested that the main result does not change if we increase the "box" by two times or take other than periodic boundary conditions.) The length of a graphene flake placed in the middle of the region is 5 μm for the first sample, 4.3 μm for the second sample, and only 1.45 μm for the third sample: this is much smaller than the size of the "box". The typical distance from the flake to the top-gate is about 200 nm (see Table 4.1). The geometry shown in Fig. 4.8(a) is for S2 sample where the distance from the flake to the top-gate is 250 nm. The metallic top-gate in Fig. 4.8(b) is shown as a rectangle with constant potential along the boundaries. The flake has been modeled as a line placed on top of a SiO_2 substrate of 300 nm thickness, with specific boundary conditions discussed below.

We have solved the Laplace equation, $\triangle\phi = 0$, in 2D (xz-plane), with a numerical package FEMLAB, which uses a finite-element method to solve 2D problems. The

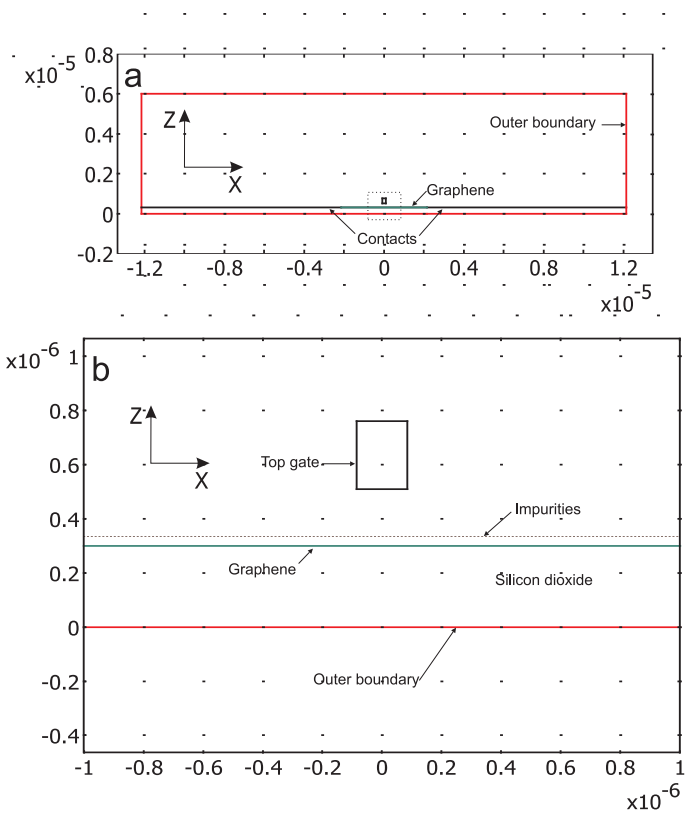

Figure 4.8: Electrostatic model used to find the distribution of potential in a graphene flake. It uses real size geometry and correct boundary conditions for graphene (see Eqs. (4.45) and (4.46)). (a) Whole geometry of the model, (b) Zoom-in region under the top-gate. An additional layer of impurities is shown by the dotted line.

code has been used to obtain the distribution of electrostatic energy in the graphene flake as a function of the x-coordinate by calculating the potential along the line of the graphene flake. This code is given in Appendix 6. We have set potentials on the back and top-gates to reproduce experimental conditions. The graphene flake was modeled using charge surface density boundary conditions, assuming that the temperature is zero. The displacement field has to have a discontinuity on the graphene flake:

$$\mathbf{n} \cdot (\mathbf{D}_1 - \mathbf{D}_2) = \rho_s, \tag{4.45}$$

where $\mathbf{n}$ is a unit vector normal to the graphene surface, $\mathbf{D}_1$ and $\mathbf{D}_2$ are displacement field vectors above and below the flake, and ρ_s is charge density defined as

$$\rho_s = -e \int_0^{e\phi} \frac{g_s g_v}{2\pi\hbar^2 v_F^2} \varepsilon d\varepsilon = -\frac{g_s g_v e^3}{2\pi\hbar^2 v_F^2} \frac{\phi^2}{2} \mathrm{sign}(\phi), \tag{4.46}$$

where sign(ϕ) determines the sign of the potential (sign(ϕ) = 1 if $\phi > 0$, otherwise sign(ϕ) = -1), g_s is the spin degeneracy, and g_v is the valley degeneracy. The charge cannot move (there is no current) but is allowed to redistribute in a self-consistent way over the flake. The carrier concentration can then be written as

$$n = g_s g_v \int \frac{d\kappa_x d\kappa_y}{(2\pi)^2} = g_s g_v \int \frac{2\pi\kappa d\kappa}{(2\pi)^2} = \int \frac{g_s g_v |\varepsilon|}{2\pi\hbar^2 v_F^2} d\varepsilon. \tag{4.47}$$

In this relation, the density of states $g_s g_v|\varepsilon|/2\pi\hbar^2 v_F^2$ for graphene is used – it is linear as a function of energy and disappears at zero energy.

The resistance as a function of back-gate voltage gives the dependance of resistivity on potential in the graphene flake, $\rho(\phi)$, if the relation between ϕ and V_{bg} is known. As soon as we know the potential distribution in the graphene flake obtained from the modelling, the resistance of any part or whole structure can be found by integration of the resistivity $\rho(\phi(x))$ over the flake length. We used for calibration the experimental resistance dependence on back-gate voltage to find $\rho(\phi(x))$. The calibration curve has been fitted by a piecewise polynomial function to get an analytical expression which later has been used in numerical integration. Thus, the resistance as a function of top-gate voltage at different fixed back-gate voltages can be obtained from the integral

$$R = \int_0^L \rho(\phi(x)) dx. \tag{4.48}$$

The position of the Dirac point in the three samples is shifted from zero V_{bg} (see 4.6(a)) due to unintentional doping. In our calculations we assumed that the Dirac point is at zero back-gate and top-gate voltages, by shifting the whole curve, but adding a layer of charged impurities above the flake to the model has helped to introduce the Dirac peak shift seen in experiment. (The shift of the Dirac point occurs due to doping and the value of the shift gives us the concentration of these impurities.) The charged impurities induce the same charge but of opposite sign is added to the flake. The resistance dependence on back-gate voltage is reproduced exactly by the model with this impurity layer. We have found that there is no difference in $R(V_{bg})$ if the layer position is shifted from 1 nm to 10 nm above the graphene flake.

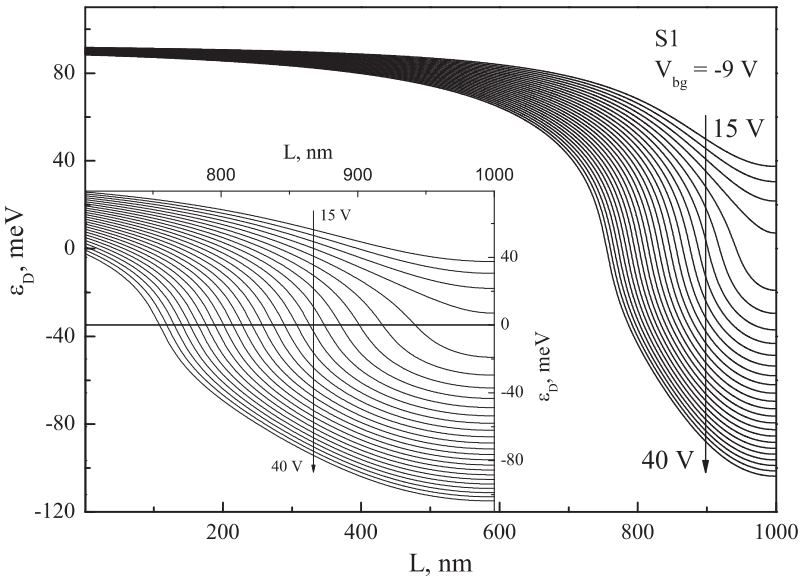

Figure 4.9: Position of the Dirac point, ε_D, for different top-gate voltages at -9 V applied on the back-gate as a function of coordinate for sample S1. Half of the potential is presented. Top-gate voltage changes from 15 V to 40 V with 1 V increment. Inset: zoomed in region.

To compare the model with the experimental dependence of the resistance of the structure on top-gate voltage at different back-gate voltages (see Fig. 4.6(b-d)) we have had to find a specific doping level which should be introduced to make the resistance $R(V_{tg} = 0)$ in agreement with $R(V_{bg})$. In the range of V_{tg} corresponding to accumulation (negative V_{tg}) and depletion (small positive V_{tg}) under the top-gate, the resistance is well-described by the diffusive model, Fig. 4.6(b-d). Then we have found the efficiency of the top-gate (in other words, how efficiently the top-gate can change the concentration in comparison with the back-gate) which is determined by the distance between the flake and the top-gate only, for our samples. This distance was left as a free parameter in the model. We have found that the distance changes from 130 nm to 210 nm for samples S3 and S2, respectively, Table 4.1.

The dependence of the length of the n-region for sample S1 when a *p*-*n*-*p* structure is formed under the top-gate is presented in Fig. 4.9. This graph shows the position of the Dirac point, or equivalently the potential in the flake as a function of distance for different top-gate voltages. It is seen that the energy gradient (see the inset in the same figure) of the electrostatic energy at zero energy (energy of mobile electrons) changes very slowly as a function of top-gate voltage from 25 V to 40 V. Thus, from the point of view of tunnelling through the junction, the resistance of a ballistic *p*-*n*

junction, Eq. 4.35, should be constant as a function of top-gate voltage and we need only calculate one point in top-gate voltage to estimate this resistance. (We have not considered the strongly nonlinear regime near the point where p-n junction is just formed.)

4.4.3 p-n junction

In the range of V_{tg} corresponding to accumulation (negative V_{tg}) and depletion (small positive V_{tg}) under the top-gate, the resistance is well-described by the diffusive model, Fig. 4.6(b-d). One adjustable parameter, the distance h between the top gate and the graphene flake, was used in plotting the calculated values: h =140, 210 and 130 nm for samples S1, S2 and S3, respectively. The obtained values are close to those expected from the fabrication process and agree with observed efficiency of the top gate, Fig. 4.6(d). With larger positive V_{tg} and formation of the p-n-p structures, samples S1 and S2 show significantly larger values of the resistance than expected from the diffusive model: $\Delta R \simeq$4 and 2 kOhm, respectively. However, the narrowest sample S3 with the lowest mobility shows agreement with the diffusive model in the whole range of V_{tg}, Fig. 4.6(d).

To explain these observations, we find the characteristic thickness of the $p-n$ junctions in the three samples and compare it with the mean free path l. According to [43], the reason for the enhanced resistance of a junction is the decrease of the transmission when the electron approaches the junction at an angle $\theta \neq 0$, Fig. 4.4(a). Conservation of the parallel component of the momentum k_y produces a gap in the energy spectrum $E(k_x)$ for the motion across the junction, Fig. 4.4(b). The distance $2t$ is then defined as the classically inaccessible region which requires electrons to tunnel along it, Fig. 4.4(c): $t = \hbar v_F k_F \sin\theta/F$. The critical angle for carrier transmission in the three samples varies in the range $\theta_c = 20-30°$, assuming the length of the ballistic p-n junction to be l and taking the k_F-value at a point $x = -l/2$ from the barrier, Fig. 4.4(a). As the tunneling distance $2t$ depends on the angle of incidence, we take for a typical value of the barrier thickness $2t(2\theta_c) \simeq 40$ nm in our samples.

The mean free path l has been found using $R(V_{bg})$ of a uniform sample at $V_{tg} = 0$, Fig. 4.6(a), and the relation $\sigma = 2e^2(k_F l)/h$. The value of l weakly depends on V_{bg},

and when extrapolated to the Dirac point ($V_{bg} = 0$ for an undoped sample) gives $l \simeq 100$, 75 and 45 nm, respectively, for samples S1, S2 and S3. Comparing the tunnelling length with the mean free path shows that the p-n junctions in S1 and S2 are ballistic ($l \gg 2t$), while in S3 they are less ballistic ($l \sim 2t$). This can explain the agreement of the resistance of S3 with the result of the diffusive model in Fig. 4.6(d).

To find the expected resistance R_{pn} of ballistic p-n junction in samples S1 and S2 and compare it with the observed difference ΔR in Fig. 4.6, we first assume a smooth potential barrier, $2k_F t \gg 1$, and by using the calculated value of electric field F we get the tunneling probability $w_{np}(\theta)$ from

$$w_{np}(\theta) = e^{-\pi\hbar v_F \kappa_y^2/F}. \tag{4.49}$$

Equation 4.35 is then used to obtain the resistance of the ballistic p-n junction. We have found that using summation rather than integration is more appropriate in our case, as samples S1 and S2 have less than 12 modes (the narrowest sample S3 has only three modes). The value of the Fermi momentum k_F in these calculations is taken at a distance $l/2$ from the barrier using the values of the mean free path found above; however, the result for R_{pn} hardly changes if the value of l is varied by two times either way. This is clear as the tunneling probability $w_{np}(\theta)$ in Eq. 4.49 depends only on k_y which takes specific, quantised values $k_y = \pi n/W$. The obtained values are R_{pn} =5 and 2 kOhm for samples S1 (at $V_{bg} = -9$ V, $V_{tg} = 40$ V) and S2 (at $V_{bg} = -4$ V, $V_{tg} = 30$ V).

Taking into account the Fermi wavelength at the distance $l/2$ from the barrier, we see that $2k_F t \simeq 2$ for the three samples. To examine the applicability of a smooth-barrier approximation for this (not too large) value of $2k_F t$, we have calculated $w(\theta)$ directly using numerical methods [72] and compared the result with that obtained from Eq. 4.49. It shows less than 5% difference from the value of R_{pn} calculated above.

In experiment, it is not the resistance of an individual ballistic p-n junction which is measured but the resistance of the whole p-n-p structure. It can be different depending on whether its middle, n-region is long or short compared with l (i.e., diffusive or ballistic). For a diffusive n-region with three independent contributions (two junctions and middle region) $R_{pnp} \geq 2R_{pn}$, while for a ballistic n-region, $R_{pnp} \simeq$

R_{pn} [43]. The resistance of a ballistic *p*-*n*-*p* structure should not increase with addition of another junction as the electrons approaching the second junction have already been selected by the first junction within the critical angle θ_c. Therefore, they all will have high transmission probability $w_{np}(\theta)$ going through the second junction.

Fig. 4.6(b,c) shows clearly that the resistance of S1 and S2 is larger than that expected in the diffusive model by ΔR, because of the ballistic transport of chiral carriers through two *p*-*n* junctions. To find their resistance, we assume that they are independent; that is, the *n*-region is diffusive. Then the observed difference $\Delta R = 2(R_{pn} - R^D_{pn})$, where R^D_{pn} is the resistance of the diffusive *p*-*n* junction on the length l which was taken into account in the diffusive-model calculation shown in Fig. 4.6. With the values l =100 and 75 nm, one finds that R^D_{pn} =2 and 0.6 kOhm for samples S1 and S2, respectively. This gives the corresponding resistance of the ballistic *p*-*n* junction R_{pn} =4 and 1.6 kOhm, which is close to the expected values of 5 and 2 kOhm. (Even better agreement, within 10%, is achieved if another quantisation rule for graphene is used [71]: $k_y = \pi(n + 1/2)/W$, $n = 0, 1, 2, \ldots$) The assumption of the diffusive nature of the *n*-region at large V_{tg} is confirmed by Fig. 4.9, where the whole *p*-*n*-*p* region is seen to be larger than the mean free path. However, near the onset of the *p*-*n* junctions, at small V_{tg}, the *p*-*n*-*p* region is much shorter and can be fully ballistic.

We now discuss the applicability of Eq. (4.49) for the real potential. Using Eq. 4.31 we can rewrite Eq. 4.33 as

$$w^{exact}_{pn}(\theta) = \exp\left(-\frac{2}{v_F\hbar}\int_{-l}^{l}\sqrt{|u(x)^2 - \varepsilon_F^2\sin^2\theta|}dx\right) \tag{4.50}$$

where $u(x)$ is the real electrostatic potential energy plotted in Fig. 4.9. In Fig. 4.10 we compare the momentum as a function of distance for the real potential and the linear approximation. Because the dependence of the probability on angle θ is sharp, there is a small difference (within 1 %) between the exact probability and the approximations.

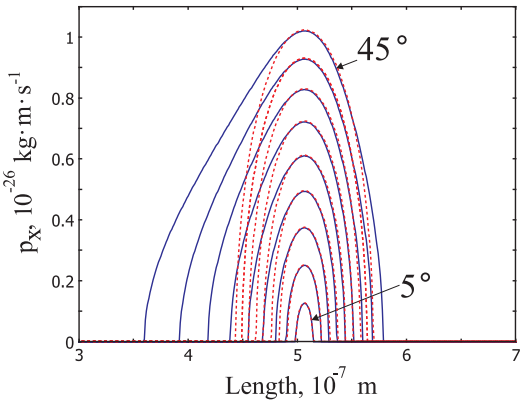

Figure 4.10: Comparison of exact and approximated potential momentums. The real part of momentum ($p_x = \sqrt{\varepsilon_F^2 \sin^2\theta - u(x)^2}/v_F$) as a function of coordinate at different angles of incidence from 5 ° to 45 ° is presented. The red dashed curves are calculated using linear approximation of potential. The most important parts of the momentum which make the main contribution to the probability are positioned in the region of $2t$. This region is around the middle of the p-n junction (505 nm).

4.4.4 p-n-p junction

We now consider the resistance oscillations which we observed in sample S1. The mean free path for sample S1 is 100 nm. This is much smaller than the width of the middle n-region in the p-n-p junction formed by the top-gate as shown in Fig. 4.9 which is about 400 nm. As transport can still be ballistic at the onset of p-n-p structure, we can speculate about the expected magnitude and period of the resistance oscillations. We have used the function $qtrans3$ (listing is given in App. 6) written by F. Guinea, which calculates the probability of passing through a p-n-p junction at some angle. This code works for any strong or sharp potential. The results of calculations for sample S1 at $V_{bg} = -9$ V and V_{tg} varying from 19 V to 40 V are shown in Fig. 4.11. For the calculations 20 modes were used. The period of these oscillations is about 1.3 V which is about 3 times smaller than those observed in experiment. The amplitude of the oscillations is 0.4 kOhm, which is also smaller than experimental value of 1-5 kΩ. To observe oscillatory behavior of the resistance originating from the interference of electron waves within the n-region as a function of top-gate voltage we need a much shorter n-region, which can be done only if the top-gate width is shorter than 100 nm and the distance between this gate and the flake smaller than 100 nm.

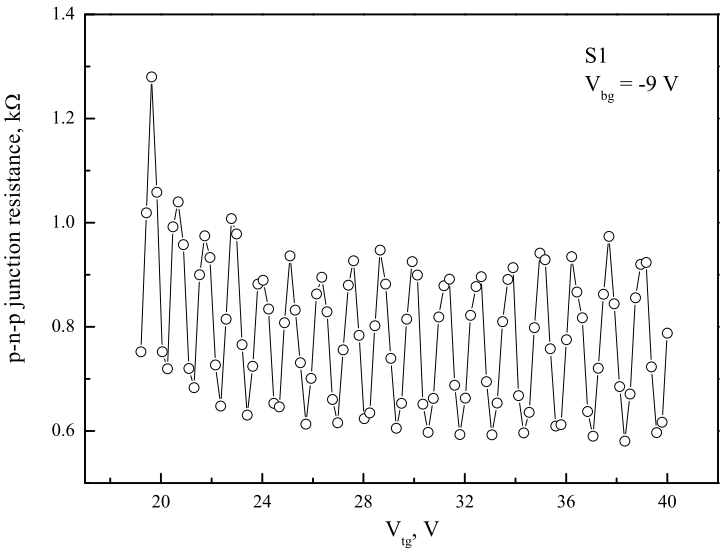

Figure 4.11: Oscillation of the resistance as a function of top-gate voltage for S1 sample for discreet valuers of the wavevector. $V_{bg} = -9$ V.

4.4.5 Magnetoresistance of p-n-p structure

In Fig. 4.7(d) top-gate dependences of the resistance at different magnetic fields for sample S3 are presented. It is seen that the magnetoresistance is approximately linear as a function of magnetic field, which can be due to geometric magnetoresistance as it expected to be linear at high magnetic fields [73]. The geometry of the sample has to be taken into account, when a region with different types of carrier is formed under the top-gate. When the sample has three regions connected in series: left p-region, central n-region, and right p-region, the magnetoresistance increases because the central "sample" is shorter than the whole structure (where geometric resistance is the smaller). Sample S3 has not been studied in detail.

To study the effect of magnetic field on the resistance of p-n-p, a structure diffusive sample S5 has been used, Table 2.3. Fig. 4.12(a) shows the resistance as a function of back-gate voltage at $T = 50$ K($V_{tg} = 0$ V). The Dirac point is at $V_{bg} = -0.75$ V. This $R(V_{bg})$ dependence has been used to find the separation between the top-gate and graphene layer. The measurements of the resistance as a function of V_{tg} at $V_{bg} = -9$ V show good agreement with our diffusive transport modelling, Fig. 4.12(b).

The resistance as a function of magnetic field, B, has been measured at different back-gate voltages, Fig. 4.13(a). The magnetoresistance at different V_{bg} as a function of B-field is shown in Fig. 4.13(b). The source of the magnetoresistance in weak magnetic field is weak localisation [24], but when magnetic field increases, at $V_{bg} = -7$ V Shubnikov-de Haas effect can be seen [21, 22]. In the Dirac point magnetoresistance has a peculiar shape observed recently in [74], which is probably caused by the presence of two types of carrier near the Dirac point.

To explain the magnetoresistance a program written on Matlab for calculation of the resistance in 2D sample has been used. This code was written by Andrei Shytov (Department of Physics, University of Utah, Salt Lake City, US) and Leonid Levitov (Department of Physics, Massachusetts Institute of Technology, Cambridge, US). If the resistivity tensor, $\rho(x, B)$ is given as a function of space coordinate the program allow to calculate the resistance of a rectangular sample. The experimental magnetoresistance dependence of a uniform sample at $V_{bg} = 0$ have been used to find a relation between the gate voltage and resistivity at fixed magnetic field. Because we only had results for three back-gate voltages, two linear fits were used to find the resistivity at any back-gate voltage. Then we have calculated the position of the Fermi level along the sample using the electrostatic model (at some fixed back-gate and top-gate voltages) and and using the linear extrapolation of the magnetoresistance, found the local resistivity, $\rho_{xx}(x, B)$, as a function of the x-coordinate. To find the $\rho_{xy}(x)$-component of the resistivity tensor, a standard assumption of the dependence on the carrier concentration has been used:

$$\rho_{xy}(x) = \frac{B}{en(p)}, \tag{4.51}$$

where $n(p)$ is the local concentration of electrons (holes), and e is the electron (hole) charge. Because the behaviour of $\rho_{xy}(x)$ near the Dirac point is unknown, we have used a cut-off energy (± 40 meV) where resistivity $\rho_{xy}(x)$ is constant (these regions are shown be arrows in Fig. 4.13(c)). Fig. 4.13(c) shows the components of the resistivity tensor for $V_{bg} = -7$ V, $V_{tg} = -40$ V, $B = 1$ T.

The comparison between experiment and theory is presented in Fig. 4.13(d). Good agrement is seen between experiment and calculations up to $B = 2$ T at $V_{tg} = 15$ V, when the sample has no p-n junctions. When $V_{tg} = 40$ V is applied

one can see that there is good agreement up to $B = 1$ T, but then experimental magnetoresistance shows a more rapid increase. This discrepancy can be due to lack of accuracy, because we have only three back gate voltages in the calibration procedure. The temperature can affect the magnetoresistance at higher magnetic field (we have compared the magnetoresistance of *p-n-p* structure measured at $T = 22$ K, Fig. 4.13(d), with the calibration curves measured at $T \sim 30$ K, Fig. 4.13(a)).

Finally, we can conclude that the diffusive model of magnetoresistance shows good agrement with experiment within $B = 1$ T and more accurate measurements are required for higher magnetic fields.

4.5 Conclusions

An electrostatic model for a top-gated graphene sample has been presented which can be used to calculate the dependence of the resistance on top-gate voltage. In this model the characteristic feature of graphene (linear density of states) is explicitly used. We have found that the transport in the fabricated *p-n* junctions is indeed ballistic, with the characteristic feature of selective transmission of chiral particles. Using this model has allowed us to find unambiguously the contribution of ballistic resistance of individual *p-n* junctions to the total resistance of the *p-n-p* structure. The theory by Cheianov's and Fal'ko's [43] for a ballistic *p-n* junction is used to obtain a quantitative agreement between theory and experiment.

The analysis of magnetoresistance of the studied *p-n-p* structures has revealed a significant contribution of classical geometric magnetoresistance . We show that its contribution has to be taken into account when searching for new quantum effects in the magnetoresistance of chiral particles.

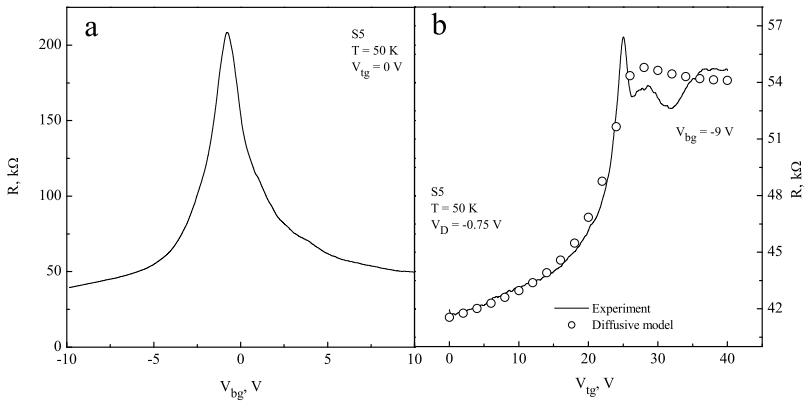

Figure 4.12: (a) Resistance of sample S5 as a function of the back-gate voltage, at $V_{tg} = 0$ V, $T = 50$ K. (b) The resistance of sample S5 as a function of top-gate voltage at $V_{bg} = -9$ V. Points show the results of the calculations of the expected resistance assuming diffusive transport of carriers.

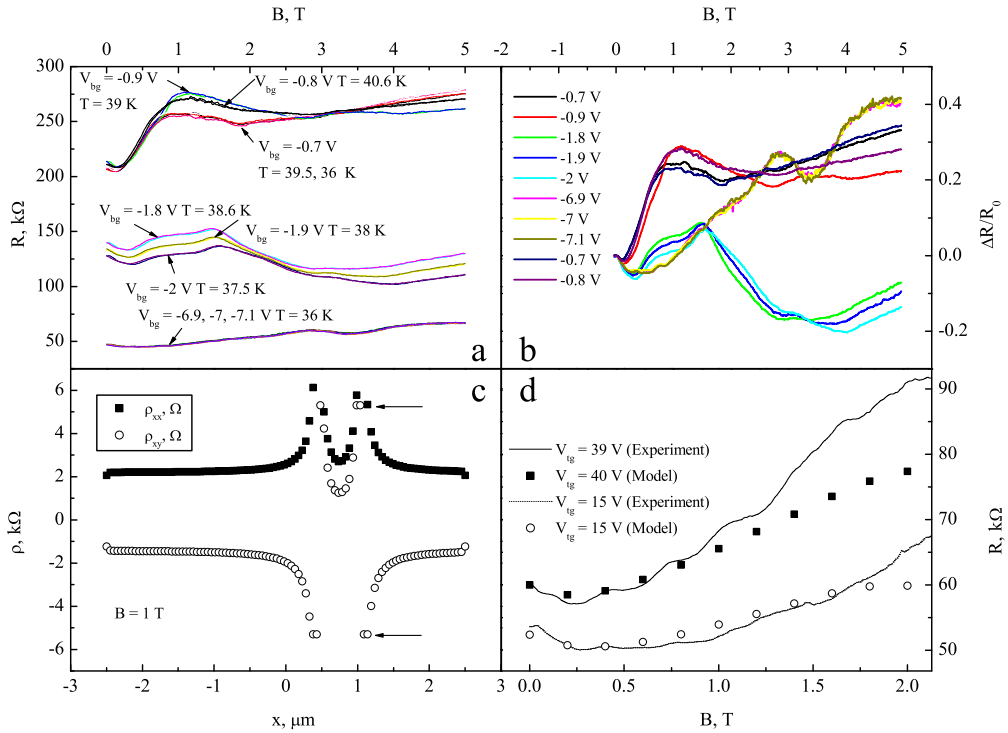

Figure 4.13: Analysis of the magnetoresistance of sample S5. (a) Resistance as a function of magnetic field at several V_{bg}. (b) Magnetoresistance at different V_{bg} using B-field dependences from (a). (c) The calculated components of the resistivity tensor at $B = 1$ T for $V_{bg} = -7$ V and $V_{tg} = 40$ V. (d) Comparison of the experimental resistances as a function of magnetic field at $V_{tg} = 15$ V and $V_{tg} = 39$ V ($T = 22$ K) with the calculated resistances at $V_{tg} = 15$ V and $V_{tg} = 40$ V, respectively.

Chapter 5

Noise in graphene

5.1 Introduction

In this chapter we describe $1/f$ noise measurements in graphene and few-layer graphene samples. It is important to investigate the noise properties of graphene if its properties such as its high mobility at room temperature are to be explored in electronic applications. A decrease of the noise in the Dirac point of few-layer graphene in a wide temperature range and a decrease in the noise in the Dirac point of graphene above 50 K have been observed. We will discuss possible physical reasons for this behavior.

The first part of this chapter is an introduction to the $1/f$ noise physics of conventional MOSFET structures and nanotubes (graphene rolled into a cylinder). Knowledge of the origin of noise in MOSFETs (based on Si/SiO_2) is crucial for understanding that in graphene on Si/SiO_2 substrate. It is also important to compare the noise in graphene with that in nanotubes due to the strong material similarity.

In the second part, the experimental results on noise are presented and discussed for multilayer and single-layer graphene. Similarities between nanotubes and graphene both placed on top of SiO_2 can be used to understand the origin of $1/f$ noise in graphene.

5.2 Noise in conventional systems

The phenomenon of $1/f$ noise has been observed in many different electronic systems. It has been extensively studied in silicon MOSFET structures [6]. Here, the

influence of the charge traps in the SiO_2 was recognised as the primary source of the noise [75]. Occupancy of these traps by charge carriers can change the current in the MOSFET by Coulomb interaction and by fluctuating carrier concentration in the channel. This leads to temporal switching of the current depending on the occupancy of a trap – Random Telegraph Noise (RTN). The model of many RTN signals (Sec. 1.3.4) with a broad range of characteristic times is usually used to explain the appearance of the $1/f$ spectral power dependence (discussed below). However, the existence of $1/f$ noise not only in MOSFET but also in many other electronic systems suggests that a more fundamental and universal mechanism might exists, but it has not been discovered yet.

Hooge's empirical relation [76] provided a useful transformation between the normalised noise amplitude and number of mobile carriers in the system. The relation comes from the assumption of a Poisson distribution of random fluctuations and is applied to many studied systems, although it is not universal [10]. This relation states that the normalised noise power, S_R, of resistance fluctuations is inversely proportional to the number of carriers, N: [76]:

$$\frac{\Delta S_R}{R^2} = \frac{\alpha}{N}\frac{1}{f}, \tag{5.1}$$

where α is a factor which depends on the material and f is the frequency. A smaller number of carriers N leads to larger relative fluctuations of the resistance R.

5.2.1 $1/f$ noise in MOSFETs

Here we discuss two models for $1/f$ noise in MOSFETs commonly used in literature. Impurities in SiO_2 play an important part in these models. A sketch of a gated MOSFET with impurities close to the 2DEG is shown in Fig. 5.1.

Using the Drude formula, Eq. 4.24, which describes the conductivity in metallic-like two-dimensional samples, conductivity fluctuations can be written as

$$\Delta\sigma = \Delta n e\mu + ne\Delta\mu, \tag{5.2}$$

where Δn represents the concentration fluctuations of mobile carriers, and $\Delta\mu$ the mobility fluctuations. One of the $1/f$ noise models in MOSFETs, proposed by

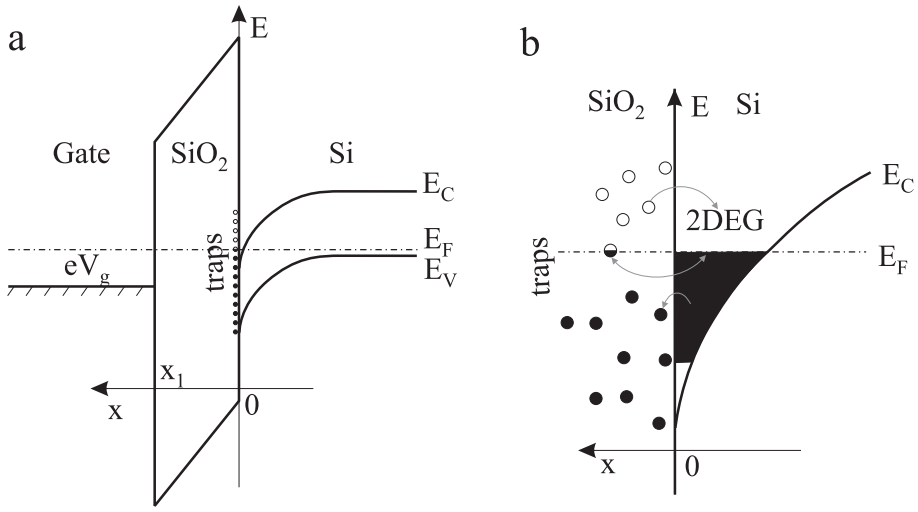

Figure 5.1: Model of charge traps at the Si/SiO_2 interface. (a) The band diagram with bias V_g applied to the gate. (b) A zoomed-in region near the interface where tunnelling between the 2DEG and traps occurs.

Hooge [77], suggests that the mobility fluctuations are the reason for $1/f$ noise in inversion layers in MOSFETs. The power spectral density of mobility fluctuations is given by

$$S_\mu = \mu^2 \frac{\alpha_H}{Nf}, \tag{5.3}$$

where α_H is called Hooge's constant and equal to $\sim 2 \times 10^{-3}$ for many two-dimensional systems.

A magnetic field and specific sample geometry (Corbino disk) can be used to distinguish between fluctuations in concentration and mobility [78]. Basically the statement is that noise has to disappear at the point where the product of the mobility at zero field and magnetic field is equal to unity, namely mobility fluctuations are given by [6]

$$\frac{S_\mu(f,B)}{\mu^2} = \left(\frac{1-(\mu_0 B)^2}{1+(\mu_0 B)^2}\right)^2 \frac{S_\mu(f,0)}{\mu_0^2}, \tag{5.4}$$

where $\mu = \mu_0/(1+(\mu_0 B)^2)$ is the mobility in magnetic field, and μ_0 is the mobility at $B = 0$. This has been tested in n-GaAs systems where it was shown that the noise power spectral density is independent of magnetic field. Therefore in these systems the noise originates from fluctuations in the number of carriers, but not in the mobility [79].

The second model which was, historically, first introduced by McWhorter [11] describes how $1/f$ noise originates from fluctuations in the number of mobile carriers.

These fluctuations occur naturally when electrons in the 2DEG jump to the traps in SiO_2, Fig. 5.1(b). Scorfield and Fleetwood [75] in a similar model assumed that the distribution of the traps, which in general is dependent on energy and distance from the 2DEG, is constant and independent of the coordinate: $n_t(E_t, x) = n_{0t}$. Because the probability of tunnelling is exponentially depend on distance, the autocorrelation function for this random process is given by [75]

$$G_{n_t}(\Delta t) = \frac{n_{0t}}{LW} f(E,T)(1 - f(E,T)) e^{\frac{-|\Delta t|}{\tau(E)}}, \tag{5.5}$$

where $\tau(E)$ is the characteristic time for tunnelling, the product LW is the area of the sample, and $f(E,T)$ is the Fermi-Dirac distribution. A Fourier transform of the last expression gives the power spectral density for the corresponding RTN signal,

$$S_{n_t} = \frac{n_{0t}}{LW} f(E,T)(1 - f(E,T)) \frac{4\tau(E)}{1 + (2\pi f \tau(E))^2}. \tag{5.6}$$

To get the total noise power one has to integrate over the energy and distance of the traps from the Si/SiO_2 interface. This can be simplified at low temperatures where the product $f(E,T)(1 - f(E,T))$ can be replaced by the Dirac-delta function. The total power spectral density of the number of carriers is then given by [75]

$$S_{N_t} \approx \frac{kT D_t(E_F)}{LW \ln \tau_1/\tau_0} \frac{1}{f}, \tag{5.7}$$

where τ_0 and τ_1 are the limits related to the cut-offs for low and high frequencies, $D_t(E_F) = x_1 n_{0t}$ is the number of traps per unit area and per unit energy at the Fermi level. It can be seen that the noise in this model has a linear temperature dependence. The measured relative noise is related to S_{N_t} via the capacitance of the oxide C_{ox} as

$$\frac{S_V}{V^2} = \left(\frac{e}{C_{ox}(V_g - V_T)} \right)^2 S_{N_t} = \frac{S_{N_t}}{n^2}, \tag{5.8}$$

where V is a source-drain voltage, V_g is the gate voltage (Fig. 5.1(a)), V_T is a threshold voltage where the conduction of the inversion layer starts.

5.2.2 $1/f$ noise in carbon nanotubes

Noise in carbon nanotubes (CNT) has been studied because of its importance in device applications. By studying the influence of the material of the contacts to a semiconducting nanotube FET in the ballistic regime, Appenzeller *et al.* [80] showed that $1/f$ noise comes from fluctuation in the number of carriers in the channel but not fluctuations of the mobility. They found Hooge's constant to be equal to 7.5×10^{-4}. In contradiction with this result, a study [81] has shown that the mobility does fluctuate, and with a much larger Hooge's constant equal to 9.3×10^{-3}. They have found that the normalised noise does not obey Eq. 5.8, but $S_V/V^2 \propto 1/|V_g - V_T| \propto 1/n$. An additional result in this paper was that the adsorbates on the nanotube do not effect the noise: no difference was found in the noise of the nanotube in vacuum and exposed to air.

The influence of impurities in the substrate on CNT noise has also been studied [82]. The authors measured $1/f$ noise in a nanotube on a Si/SiO_2 substrate before and after removing part of the SiO_2 under the nanotube substrate, and found that noise was reduced by an order of magnitude.

5.2.3 Experiments on $1/f$ noise in graphene nanoribbons

Previously, $1/f$ noise has been observed in graphene nanoribbons [20, 83]. The width of these nanoribbons is so small (about 20 nm) that a bandgap of about 26 meV is formed [20], making them a narrow-gap semiconductors. $1/f$ noise in several two-terminal field-effect transistors has been studied at room temperature. The resistance as a function of back-gate voltage of one single-layer device and one double-layer sample are shown in Fig. 5.2(a). The resistivity peak is about 32 kOhm (it is about order of magnitude higher than in our samples) in the Dirac point. The amplitude of the noise, defined as $A_N = fS_I/I^2$, changes from 10^{-6} Hz^{-1} at high concentration (± 20 V) to $2.5 \cdot 10^{-6}$ Hz^{-1} in the Dirac point. This observed increase of the noise is similar to the behaviour of $1/f$ noise in normal MOSFET structures and carbon nanotubes. The authors claim that Hooge is applicable for graphene nanoribbons and found $\alpha_H = 10^{-3}$. The experiment with a double-layer graphene has shown a qualitatively different behaviour of noise amplitude as a function of gate voltage. The noise amplitude has a dip in the Dirac point, Fig. 5.2(c). The

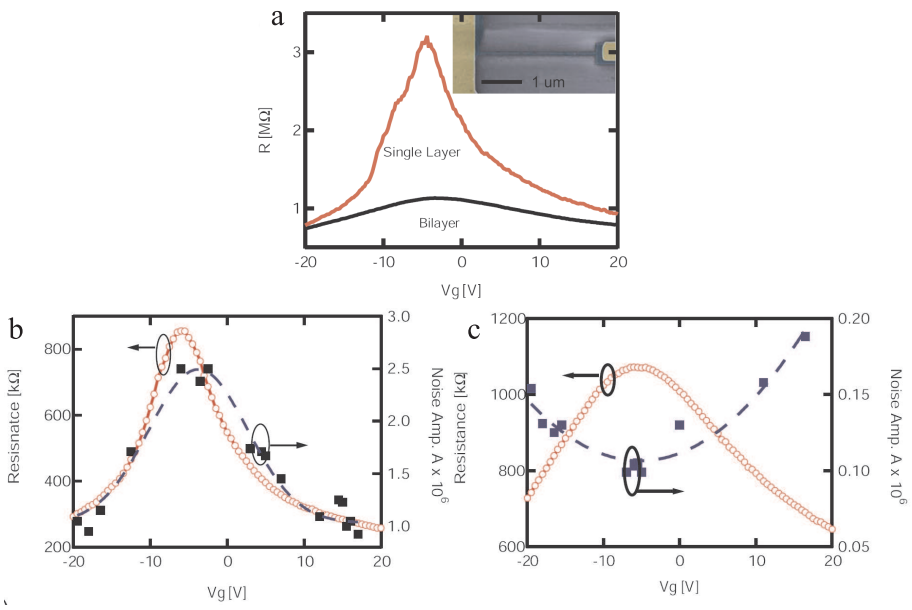

Figure 5.2: (a) Resistance of one single-layer and one bilayer graphene nanoribbon devices measured as a function of gate voltage (at $T = 300$ K). The two devices have identical channel layout (width $W = 30$ nm and length $L = 2.8$ μm) as shown in the inset. (b) The resistance, R, and the noise amplitude A_N, of the single-layer graphene nanoribbon device measured as a function of gate voltage. The dashed curve is a guide to the eye, illustrating the correlation between A_N and R. (c) The resistance and the noise amplitude of the bilayer graphene device measured as a function of gate voltage. The dashed curve is a guide to the eye, illustrating the inverse relation between A_N and R. Adapted from [83].

amplitude of the noise in the Dirac point decreased in comparison to the single layer by 25 times. However it appears that due to small width ($\sim$ 30 nm) of the nanoribbon the authors are dealing with a regular narrow-gap semiconductor ($\sim$ 20 meV), but not with single-layer graphene with a zero band gap.

5.3 Experiments and analysis

5.3.1 $1/f$ noise in multilayer graphene

Sample ML2 has a thickness of $\sim$ 2 nm (estimated by eye using the difference in the visibility contrast of different flakes) which corresponds to about 4 layers of graphene. The sizes of the sample are given in Table 2.2. The sample cannot be thicker than 10 layers, because otherwise it would not have good gate control seen experimentally. We expect that $1/f$ noise would be too small to be measured in the case of a bulk graphite sample where all traps in the SiO_2 are well screened and

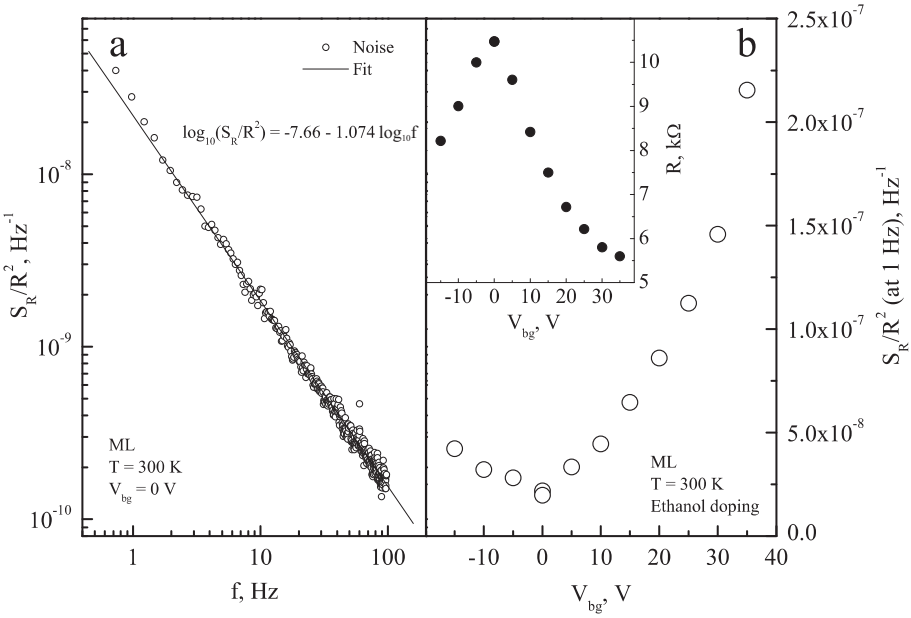

Figure 5.3: Noise in a multilayer graphene sample ML2 after ethanol doping. (a) An example of the spectrum measured up to 100 Hz at 0 V on the gate at $T = 300$ K. The slope of the fit is about 1. (b) The dependence of the resistance noise spectral power at 1 Hz as a function of gate voltage. Inset: the resistances for each gate voltage where noise has been measured. One can clearly see that the dip in the noise corresponds to the resistance peak.

cannot change much the concentration or mobility of the sample. This two-terminal device has been used for noise measurements at room temperature with two different dopants (ethanol and tap water), and also at 4.2 K in a helium dewar. Spectra have been taken in the range from 0.25 to 100 Hz at room temperature and from 0.5 Hz to 400 Hz at liquid helium temperature. For a given resistance, R, the noise power S_V was found to scale with the square of $V_{\rm sd}$ across the sample as expected. in addition, we have not observed at room temperature any nonlinear current-source-drain voltage characteristics. An influence of the doping by tap-water and ethanol on noise in multilayer graphene (the doping is made by placing a droplet of tap water or ethanol on top of the sample).

The background noise at $V_{sd} = 0$ has been subtracted from the total noise to get excess noise with 2 mV applied across the sample at room temperature. Then, the noise power has been divided by the square of voltage to obtain the quantity $S_R/R^2 = S_V/V^2$ as a function of frequency. The obtained dependence has been fitted to check the power dependence for $1/f^\alpha$ noise. The slope α is about 1 ± 0.1 for all measured resistances (an example of noise measured in the Dirac point is

shown in Fig. 5.3(a)). From the fit we have obtained the magnitude of the noise at 1 Hz and plotted it in the Fig. 5.3(b), as a function of V_{bg}.

The position of the Dirac point is shifted to zero voltages after ethanol doping. The main feature of the noise dependence on back-gate voltage in the sample doped by ethanol is the observation of the noise minimum at the position of the resistance peak (see the inset in Fig. 5.3(b)). Such behaviour of noise is in contradictions with Hooge's relation which states that the largest resistance fluctuations are observed at small carrier concentration, Eq. 5.1.

After tap water doping, the Dirac point is shifted to positive gate voltages (the position of the Dirac point is about 15 V). The slope of the power spectral density of noise dependence on frequency has a good stability and is always very close to 1, Fig. 5.4(a). The minimum in the noise is again observed, but it has been shifted so that the position of the dip corresponds to the new position of the Dirac point. This is shown in Fig. 5.4(b). This suggests that the minimum in noise is not related to a specific distribution of impurities in the oxide, but is a result of different physics in the Dirac point. It is seen that the smallest noise observed in the Dirac point of sample ML2 at 300 K is $\sim 10^{-8}$ Hz^{-1}.

It is known that there are electron-hole puddles in single-layer and double-layer graphene near the Dirac point [60, 84]. If the noise has a minimum in the Dirac point which is shifted due to doping, it has to be related to the properties of the graphene itself, but not to the properties of the SiO_2. Below is a qualitative model how the presence of puddles near the Dirac point can explain the noise dip.

Lets assume that we have a finite concentration of the two types of carrier ($N(t)$ is for electrons and $P(t)$ is for holes) in the puddles. Let us also assume that we can write the noise in terms of the fluctuations of the number of carriers as

$$\frac{S_V}{V^2} = \left(\frac{\Delta N}{N} + \frac{\Delta P}{P}\right)^2, \tag{5.9}$$

where ΔN is a random fluctuation in number of electrons.

Eq. 5.9 can be simplified if we take into account that for random fluctuations $\Delta N/N = 1/\sqrt{N}$ and $\Delta P/P = 1/\sqrt{P}$, and that the average number of carries in the electron and hole puddles changes with gate voltage as $N_0 + CV_g/2$ and $N_0 - cV_g/2$, respectively. Assuming that the number of electrons and holes in the puddles is the

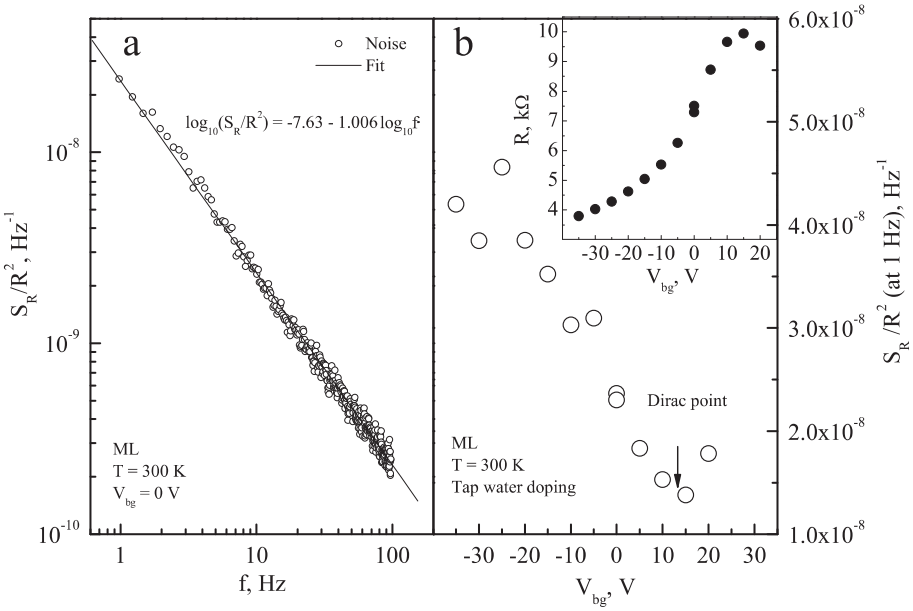

Figure 5.4: Noise in sample ML2 after tap-water doping. (a) An example of the spectrum measured up to 100 Hz at 0 V on the back-gate at $T = 300$ K. The slope of the fit is about 1. (b) The dependence of the resistance noise at 1 Hz as a function of back-gate voltage. Inset: the resistances for each back-gate voltage where noise has been measured.

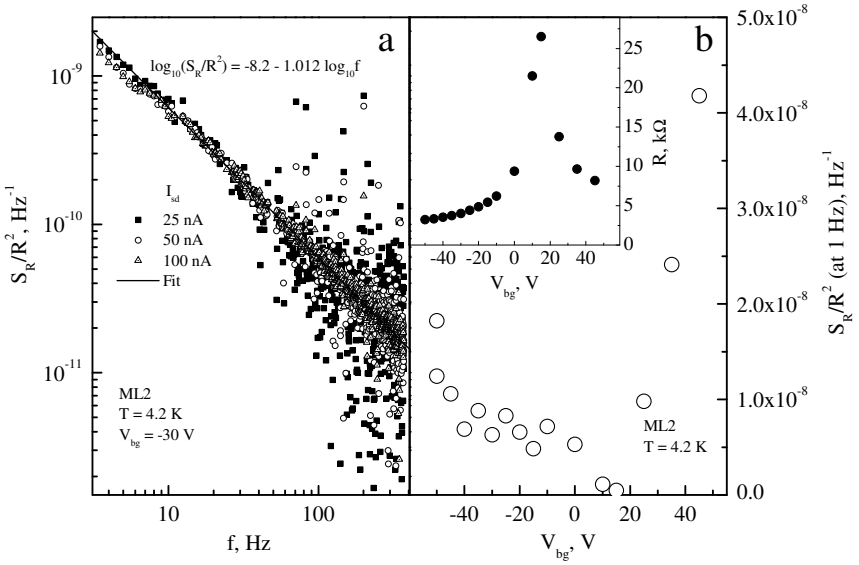

Figure 5.5: Noise in sample ML2 at 4.2 K. (a) An example of the spectrum at -30 V on the back-gate at $T = 4.2$ K for three source-drain currents calculated as $S_V/(RI_{sd})^2$. The slope of the fit is about 1. (b) The dependence of the resistance noise at 1 Hz as a function of back-gate voltage. Inset: the resistances for each back-gate voltage where noise has been measured.

same at zero gate voltage:

$$\frac{S_V}{V^2} = \left(\frac{1}{\sqrt{N + \frac{CV_g}{2}}} + \frac{1}{\sqrt{N - \frac{CV_g}{2}}} \right)^2 \frac{\alpha_M}{f}$$
$$= \left(\frac{2N}{N^2 - \frac{(CV_g)^2}{4}} + \frac{2}{\sqrt{|N^2 - \frac{(CV_g)^2}{4}|}} \right) \frac{\alpha_M}{f}. \quad (5.10)$$

where α_M is a constant which, in general, can depend on temperature and magnetic field.

This expression leads to a minimum in the noise in the Dirac point where $V_g = 0$ and the maximum near the region where the total number (both electrons and holes) of carriers in the puddles is equal to the number of carriers produced by the gate. Here, we can interpret Eq. 5.10 as a modified Hooge's relation for graphene. If we consider a hole V_g-region with the total number of carriers $P_1(t)$ in the puddle, it will fluctuate as a normal sample with one type of carrier, $S_V/V^2 \propto 1/P_1$: i. e. each uniform part of the graphene sample obeys the Hooge relation. When we apply a small gate voltage we change the concentration in the puddle: if we decrease number of holes relative fluctuations will increase and if we apply negative gate voltage the noise decreases in this puddle according to the Hooge relation. When the gate voltage is large enough, $CV_g \gg N_0$, to produce a sample without puddles we have to have a standard metallic system which obeys the Hooge relation, $S_V/V^2 \propto 1/(CV_g)$.

Because the number of carriers in the puddles has to be dependent on the temperature the existence of temperature dependence naturally appears in the model: namely the noise in the Dirac point at room temperature has to be smaller than at lower temperature (if we forget for a moment about temperature dependence of the noise amplitude, α_M).

The temperature was decreased to 4.2 K to see the effect on the noise power. The result is shown in Fig. 5.5(a). The dip in the noise is still seen at the Dirac point. However, the power density of the noise has dropped to a smaller value in the Dirac point. The decrease is about 6 times in the hole region, and 20 times in the Dirac point. It is clearly seen that the electron region has larger noise than the hole region and the ratio between the noise in the Dirac point and the noise power

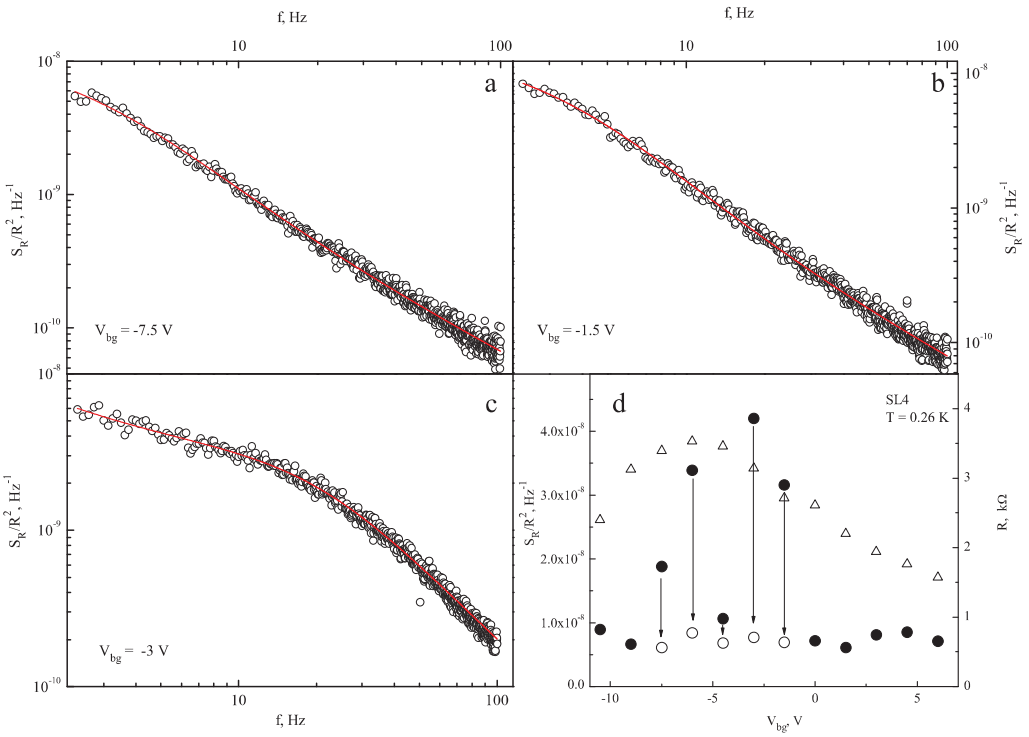

Figure 5.6: Resistance noise at T=0.26 K for sample SL4. (a-c) Spectra for different back-gate voltages -7.5 V, -1.5 V, and -3 V. (RTN is better seen in (c).) Red solid lines are the best fit using equation 5.11. (d) Solid circles show resistance power spectral density for extrapolated values at 1 Hz. The empty circles represent $1/f$ noise power at 1 Hz without the contribution of RTN, arrows show the change in $1/f$ noise amplitude when RTN is taken into account. Triangles show the resistance as a function of back-gate voltage.

at 45 V on the back-gate is 0.01 (see Fig. 5.5(b)).

Voss [85] has discussed how gate voltage fluctuations can affect $1/f$ noise. Assuming that these fluctuations can originate from the non-stable voltage source, or fluctuating occupancies of impurities in SiO_2 can produce effective fluctuating V_g, we can conclude that relative resistance fluctuations $\Delta R/R$ are proportional to the derivative of the resistance with respect to gate voltage dR/dV_g. In this case the noise would have a minimum in the Dirac point (where $dR/dV_g = 0$) and two maxima where the second derivative is zero (thus the first derivative has a maximum). A leakage current between the gate and the sample occurs through defects in the SiO_2 and causes fluctuations in voltage across the sample. In this case the noise will be proportional to the resistance of the sample. However, in our experiments we have tested the leak between the gate and the sample and the expected position of the maxima have not been observed.

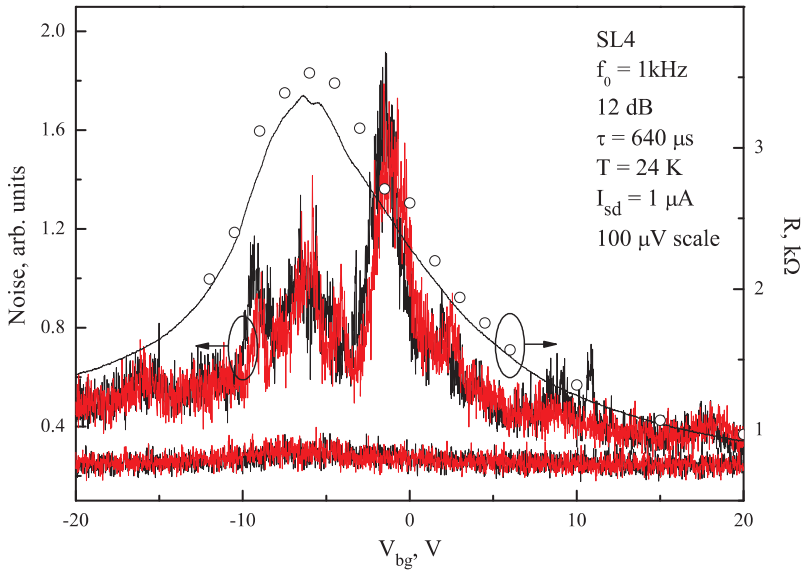

Figure 5.7: Noise measured in sample SL4 by lock-in amplifier at $T = 24$ K with 1 μA constant source-drain current as a function of back-gate voltage. Forward and backward sweeps are presented by different colors. Resistance as a function of back-gate voltage is shown at 24 K (solid line) and several resistances at base temperature from Fig. 5.6 are presented by open circles. The two lowest curves (backgrounds) are measured without applied voltage across the sample.

5.3.2 $1/f$ noise in single-layer graphene

Resistance noise has also been measured in sample SL4 at base temperature of Helium-3 system (0.26 K). The slope of the spectra for several points in back-gate voltage near the Dirac point deviates from 1, Fig. 5.6. We have attributed this to a strong effect of a single impurity which can modulate the resistance of the sample and produce (RTN) resistance noise which is added to $1/f$ noise. The total resistance noise, S_R^{tot}, is then described by the equation

$$\frac{S_R^{tot}}{R^2} = \frac{S_R^{RTN}}{1+(2\pi f\tau)^2} + \frac{S_R^{1/f}}{f}, \tag{5.11}$$

where S_R^{RTN} and $S_R^{1/f}$ are power spectral density for RTN and $1/f$ noise, respectively, and τ is a characteristic time of the RTN. The quality of the fit is shown in Fig. 5.6(a-c) by the red curves. If the contribution to the total noise from the RTN is removed, the resulting $1/f$ noise is found to be independent of the back-gate voltage from -10 V to 5 V, Fig. 5.6(d). This is different from the noise behaviour in sample ML2, where a dip in the noise is observed in the Dirac point at low temperature.

For sample SL4, we have tested the influence of the current contacts on noise.

If the voltage noise in the contacts produces fluctuations in the current, this will be seen as voltage noise on the sample. However, this (normalised) noise will be reduced by a factor $(rR_c/R_b^2)^2$, where r is the sample resistance, R_c is the contact resistance, and R_b is a large ballast resistance. In this test we have taken $r = 2.85$ kΩ (at $V_{bg} = 0$ V and $T = 8.5$ K) and two ballast resistors of 10 MΩ and 100 MΩ. The $1/f$ noise showed no difference between these two ballast resistors up to 0.25 mV applied (the noise was $1.2 \cdot 10^{-8}$ Hz^{-1}). Therefore this coefficient of suppression ($\sim 10^{-8}$) is large enough to neglect the contribution of the current contacts to the total noise.

The sample has a weak temperature dependence of the resistance, if one compares the resistance at $T = 24$ K (solid line) and at $T = 0.26$ K (empty circles), Fig. 5.7. At $T = 24$ K we have measured the integral noise in sample SL4 by lock-in amplifier at 1 μA source-drain current, Fig. 5.7. The lock-in amplifier has been used to integrate the spectral amplitude of the signal in the bandwidth, $1/8\tau$, around a central reference frequency, $f_0 = 1$ kHz. The result is shown in Fig. 5.7 by black and red noisy curves. The background (flatline in Fig. 5.7) is constant and comes from the noise of the preamplifiers. Nonmonotonic excess noise appears when a source-drain current is applied. This has a maximum not only in the Dirac point, where noise has to be larger due to the larger voltage applied, but also maxima in the region close to the Dirac point. The strongest peaks occurs at $V_{bg} = -1$ V and at 5 V from the Dirac point. The width of the peak at $V_{bg} = -1$ V is about 150 K (here we have used the expression for the change in the Fermi energy due to change of back-gate voltage $\Delta\varepsilon_F = 30\,[\text{meV}]\,\Delta V[\text{V}]/2\sqrt{V[\text{V}]}$), which is much larger than the temperature. We attribute this peak to the existence of impurities in the SiO_2 or on top of the flake in this sample. These impurities have a contribution to the noise amplitude only in a narrow back-gate voltage span of about 2 V, when the Fermi energy crosses the energy band (maxima in the density of states) occupied by the impurities. It is interesting to note that the low temperature measurements, Fig. 5.6 have shown $1/f$ noise with a slightly steeper slope, -1.31 instead -1 (for $1/f$ noise) at $V_{bg} = -1.5$ V, for another point at $V_{bg} = 0$ V there is no RTN contribution to the noise. It is worth mentioning that the half width of the noise peak is smaller than the distance between the peak and $V_{bg} = -3$ V where a clear RTN spectrum is observed, Fig. 5.6(c). We can conclude that the RTN observed at $V_{bg} = -1$ V is

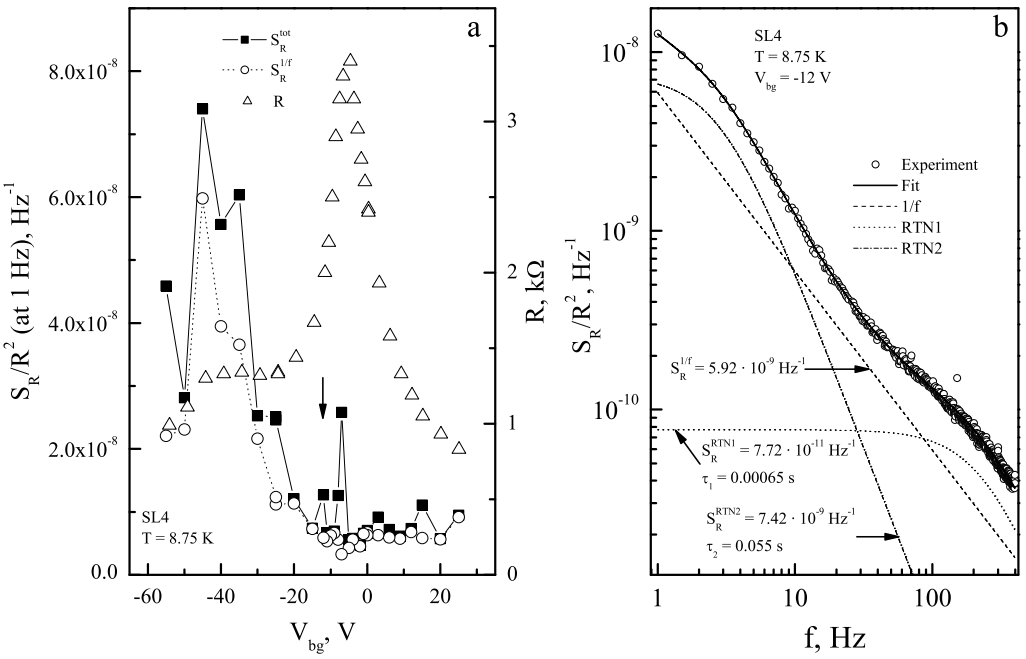

Figure 5.8: (a) Power spectral density at 1 Hz as a function of back-gate voltage at $T = 8.75$ K for sample SL4. (b) Fitting the spectrum at $V_{bg} = -12$ V using two RTN signals and $1/f$ spectrum.

not related to the RTN at $V_{bg} = -3$ V. It is also seen that the strong RTN signal at $V_{bg} = -3$ V is not present in the integrated noise dependence on back-gate voltage.

To see how temperature affects the noise, $1/f$ noise as a function of V_{bg} at 8.75 K has been measured in sample SL4. Figure 5.8(a) shows a dip in noise at 0 V (black squares). The amplitude of the noise increases from 0.5×10^{-8} Hz^{-1} (Dirac point) to 6×10^{-8} Hz^{-1} (at -40 V), and the noise decreases at higher gate voltages. Even less scattered data can be obtained if we take into account the contribution of several RTNs in the total spectrum as it shown in Fig. 5.8(b), where two RTNs with amplitudes 7.72×10^{-11} Hz^{-1} and $7.42 \cdot 10^{-9}$ Hz^{-1} are detected. The resulting noise dependence on gate voltage (empty circles) has more monotonic behaviour. This behaviour is in qualitative agreement with Eq. 5.10: there is a deep in the Dirac point, and a maximum in the noise is seen at $V_{bg} = -40$ V, and the noise decreases at larger negative voltages.

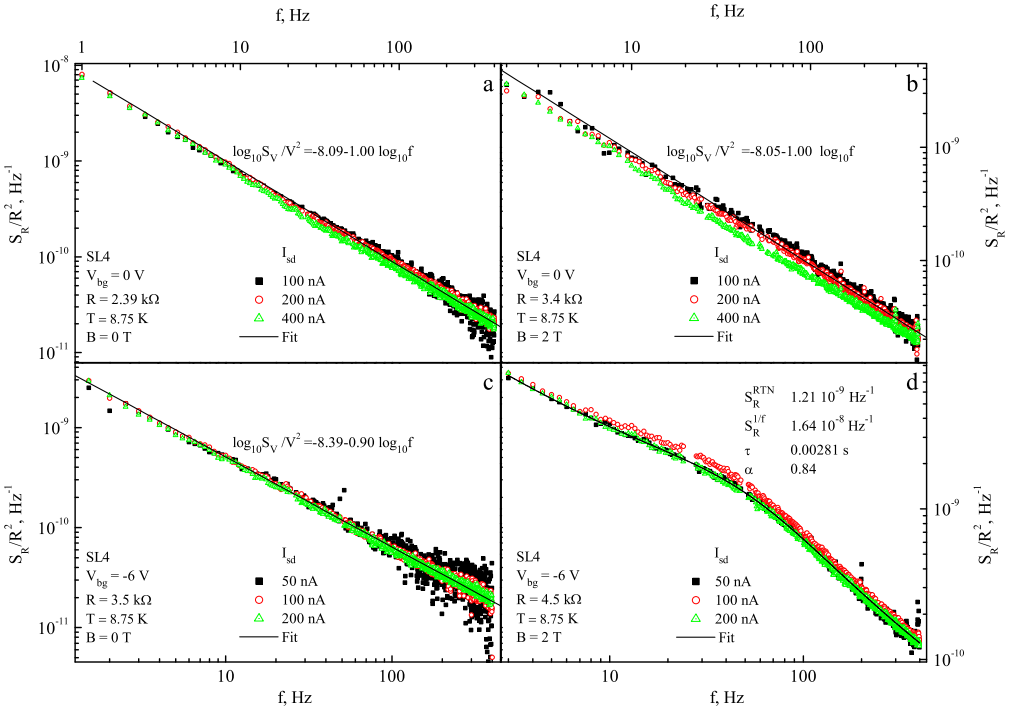

Figure 5.9: Spectra for sample SL4 at 8.75 K at three source-drain currents. (a-b) $1/f$ noise spectra away from the Dirac point show good $1/f$ dependence without magnetic field (a) and with $B = 2$ T applied (b). (c-d) Noise at the Dirac point.

5.3.3 Influence of magnetic field on $1/f$ noise

We have tested the influence of magnetic field on $1/f$ noise in single-layer graphene at $T = 8.75$ K. For sample SL4 two points in the back-gate voltage have been taken: 0 V and -6 V (Dirac point). We have measured noise spectra at magnetic fields of 0 T and 2 T applied perpendicular to the sample, Fig. 5.9. At back-gate voltage equal to 0 V (which is away from the Dirac point) we have observed a good $1/f$ frequency dependence of the spectra, with a small change in noise amplitude between 8.1×10^{-9} Hz^{-1} at 0 T and 8.9×10^{-9} Hz^{-1} at 2 T. The resistance also changes from 2.39 kOhm as 0 T to 3.4 kOhm at 2 T. In the Dirac point $1/f^{\alpha}$ noise has been observed without magnetic field, where $\alpha = 0.9$. When a magnetic field of 2 T was applied a RTN appeared and the amplitude of noise S_R/R^2 increased from 4.07×10^{-9} Hz^{-1} to 1.64×10^{-8} Hz^{-1}. Thus there is a transition in magnetic field from the situation when noise in the Dirac point is the smallest to the case where it is the largest. We have not studied this effect in detail, and we do not have yet

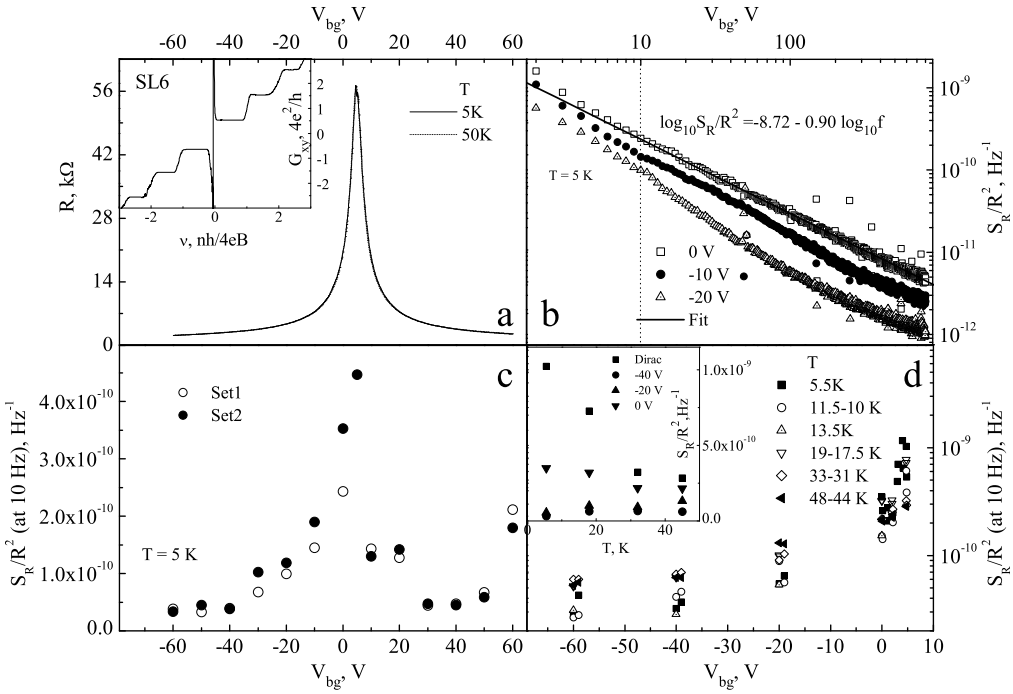

Figure 5.10: $1/f$ noise in graphene SL6 sample. (a) Resistance as a function of back-gate voltage at temperature 5 K and 50 K. Inset: quantum Hall effect for single-layer graphene measured at 5 K and fixed magnetic field 12 T. (b) Three noise spectra at 5 K for 0 V (squares), -10 V (circles), and -20 V (triangles) on the back-gate. (c) Noise amplitude at 10 Hz for two sets of measurements. (d) Temperature dependence of noise amplitude for hole region from 5.5 K to 48 K.

any conclusion about the mechanism of this transition.

5.3.4 Temperature dependence of noise

Figure 5.10(a) shows the temperature dependence of the resistance in single-layer graphene (sample SL6). It is seen to have a very weak (close to the Dirac point) or no temperature dependence. Quantum Hall effect has been measured to prove that we are dealing with a single-layer sample (see inset to Fig. 5.10(a) where the off-diagonal conductance component G_{xy} is shown as a function of the filling factor).

The noise spectra at 5 K do not have pure $1/f$ dependence, instead a contribution of RTN is seen and the slope of frequency dependence is close to 0.9 instead of 1. We have measured $1/f$ noise as a function of V_{bg} twice (see Fig. 5.10(c)). (The two measurements are separated in time by one day.) An increase of noise near the

Dirac point is seen for both sets of measurements. The noise increased by an order of magnitude from a high-conduction hole region to the Dirac point. This is usual behaviour for standard MOSFET structures (except for the last point at 60 V).

In Fig. 5.10(d) the temperature dependence of noise is shown from 5 K (filled squares) to 48 K (filled triangles) where one can see an increase of noise with increasing temperature at high hole concentration ($V_{bg} = -60$ V, -40 V, -20 V) by factor of 2. However, close to the Dirac point (-4.7 V) the noise amplitude shows an opposite behaviour: the noise decreases with increasing temperature. It is clearly seen in the inset to Fig. 5.10(d) where the results for four gate voltages are presented as a function of temperature. This unusual effect has not been observed before. It highlights the difference in the origin of noise in the Dirac point and may be related to the presence of the minimum in the dirac point in sample SL4.

The influence of the temperature on noise in sample SL6 has been studied in another cool-down. The noise dependence on gate voltage has been measured for three temperatures (140 K, 100 K, and 60 K). The results of measurements for the highest temperature are presented in Fig. 5.11. The difference of the resistance in the Dirac point at $T = 140$ K and $T = 50$ K is less than 10 %. At $T = 140$ K noise amplitude as a function of back-gate shows a dip in the Dirac point. In addition, two maxima in noise amplitude have been observed: at $V_{bg} = 1$ V and $V_{bg} = 5.5$ V. These maxima do not correspond to the maxima in the squared derivative of the sample resistance with respect to V_{bg} and cannot therefore be related to same effective gate voltage fluctuations.

It has been shown that the noise decreases from 140 K to 60 K, Fig. 5.12(a). The decrease is larger at higher gate voltage (by order of magnitude at $V_{bg} = -20$ V) but in the Dirac point the noise amplitude is smaller only by 3 times. The dip in the noise amplitude as a function of V_{bg} seen at 140 K and 100 K is absent at $T = 60$ K. This interesting observation requires more detailed studies.

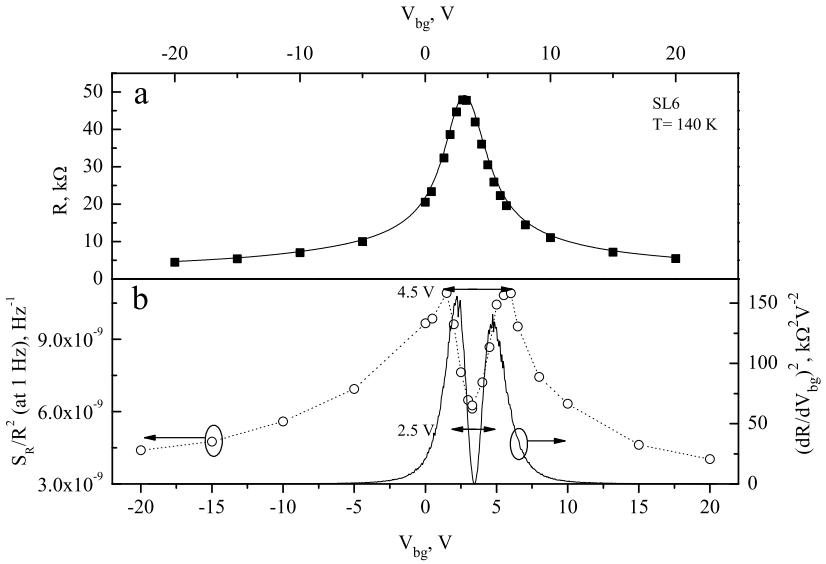

Figure 5.11: $1/f$ noise in graphene SL6 sample at $T = 140$ K. (a) Resistance as a function of back-gate voltage at $T = 140$ K. Points show the resistances for each back-gate voltage where noise has been measured. (b) The resistance noise at 1 Hz as a function of V_{bg} (left ordinate axis), and the squared derivative of the sample resistance with respect to V_{bg} as a function of V_{bg} (right ordinate axis).

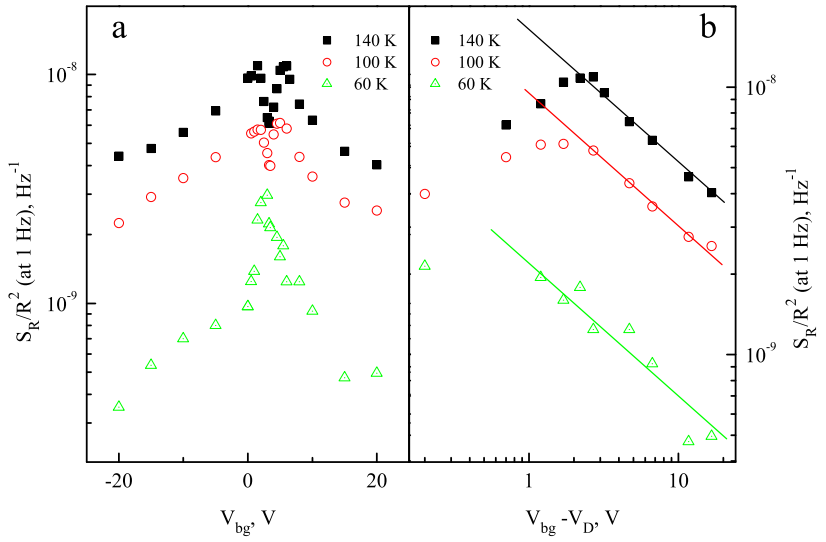

Figure 5.12: $1/f$ noise in graphene SL6 sample at three temperatures. (a) The resistance noise at 1 Hz as a function of V_{bg} at 140 K (squares), 100 K (circles), and 60 K (triangles) temperatures. (b) The dependence of the resistance noise (electron region) at 1 Hz on $(V_{bg} - V_D)$ in log-log scale. The solid lines have slopes equal to -0.5.

Fig. 5.12(b) shows the dependence of the resistance noise (electron region) at 1 Hz as a function of $(V_{bg} - V_D)$, where $V_D = 3.3$ V, in log-log scale. The lines have the slope equal to -0.5. Good agreement is seen with a square root dependence of the noise amplitude on $(V_{sd} - V_D)$. This gives another interesting feature of single-layer graphene: the Hooge relation is not applicable for graphene because in experiment

$$S_R/R^2 \propto (V_{bg} - V_D)^{-1/2} f^{-1} \propto N^{-1/2} f^{-1}. \tag{5.12}$$

Such behaviour of $1/f$ noise is observed in a wide range of temperatures, from 5 K to 140 K.

5.3.5 Current-voltage characteristic

If the differential resistance changes as a function of source-drain bias it will affect the measured noise. Therefore the nonlinearity in the current-voltage characteristic has to be taken into account. The measured monolayer (SL4 and SL6) and multilayer (ML2) graphene samples have shown a linear $I(V_{sd})$ at room temperature: SL4 and SL6 in the studied range of V_{sd} up to 1 mV, and ML2 up to 10 mV. A nonlinearity can occur at lower temperature.

A question about the influence of the contacts on the voltage dependence of the differential resistance appears due to possible the Shottky barrier between graphene and a metallic contact. In Fig. 5.13 we show the results of the normalised differential resistance dependence on DC current for sample SL6 at $T = 5.5$ K using two- and four-terminal measurements (where contacts are not important) where one can see that there is no significant difference between two types of connections. We conclude from this that all nonlinearity comes from the properties of the graphene itself.

5.3.6 Shot noise in graphene sample SL6

Shot noise has been measured in two back-gate voltages of -60 V and -40 V. The resistances at these voltages are 2.28 kΩ and 2.48 kΩ at base temperature (0.26 K). The spectra have been measured at four different source-drain currents up to 1000 nA, which produces source-drain voltages up to 2.5 mV across the sample. A six-terminal device has allowed us to use the cross correlation technique in the

frequency range from 50 kHz to 100 kHz where $1/f$ noise can be neglected. The results are shown in Fig. 5.14. As one can see the spectra have a slight bending at high frequencies (5.14(a-b)), caused by parasitic capacitance in the circuit, which is taken into account by a correction procedure where the measured spectrum, S_I is multiplied by a factor

$$S_I^{SN} = S_I(1 + (2\pi f RC)^2), \tag{5.13}$$

where R is the sample resistance, C is the capacitance of the twisted pairs used in the circuit, and f is the frequency. It is known that thermal noise has a flat spectrum. Thus one can determine the capacitance, C, of the wires by "unbending" the background thermal noise. The determined capacitance is 1250 pF which is in agreement with the estimated length of the wires.

Once the capacitance of the wires is known, shot noise spectra are obtained using Eq. 5.13. The average values of each spectra are shown in Fig. 5.14(c-d) by solid squares. It is seen that the dependence of the current noise on source-drain current is approximately linear. To compare the current noise with the theoretical shot noise $S_I = 2eIF$, where F is the Fano factor, red circles are shown for Fano factors 0.34 and 0.17 for -40 and -60 Volts, respectively. The Fano factor of 0.34 is in agreement with noise measurements in disordered short graphene samples [86] and the theory for a square sample [87]. The decrease (in disagreement with the theory [86]) of the Fano factor at higher voltages has not been observed previously.

5.4 Conclusions

It has been shown that the noise in multilayer graphene samples shows a dip in noise amplitude as a function of back-gate voltage, which can be shifted to a new position by doping as it follows the Dirac point position.

For a single layer graphene we have found two opposite types of behaviour: a dip in the Dirac point in one sample (observed in sample SL4 at 8.75 K), but a noise peak in the Dirac point in another (SL6) at 5 K. However, a dip in noise amplitude at the Dirac point has been observed in sample SL6 at 100 and 140 K. More samples for statistics are required to explain this unusual effect. In sample SL6 we have observed an increase of the noise as a function of temperature at high hole

concentration, but in the Dirac point noise decreases as a function of temperature (from 5 K to 50 K), which unveil the presence of different mechanism of noise in these regions. This effect also requires further investigation.

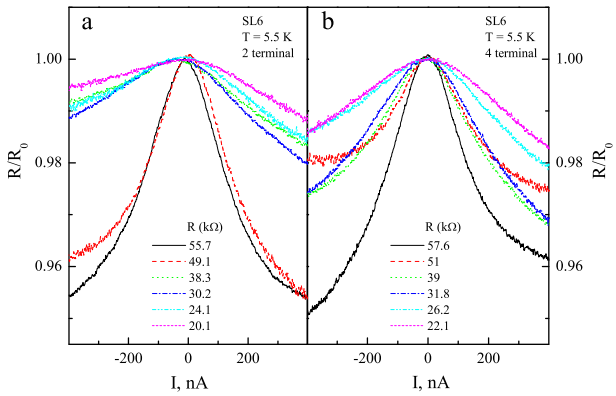

Figure 5.13: Normalised resistance in the Dirac point as a function of source-drain current for sample SL6 at 5.5 K. (a) 2 terminal circuit. (b) 4 terminal circuit.

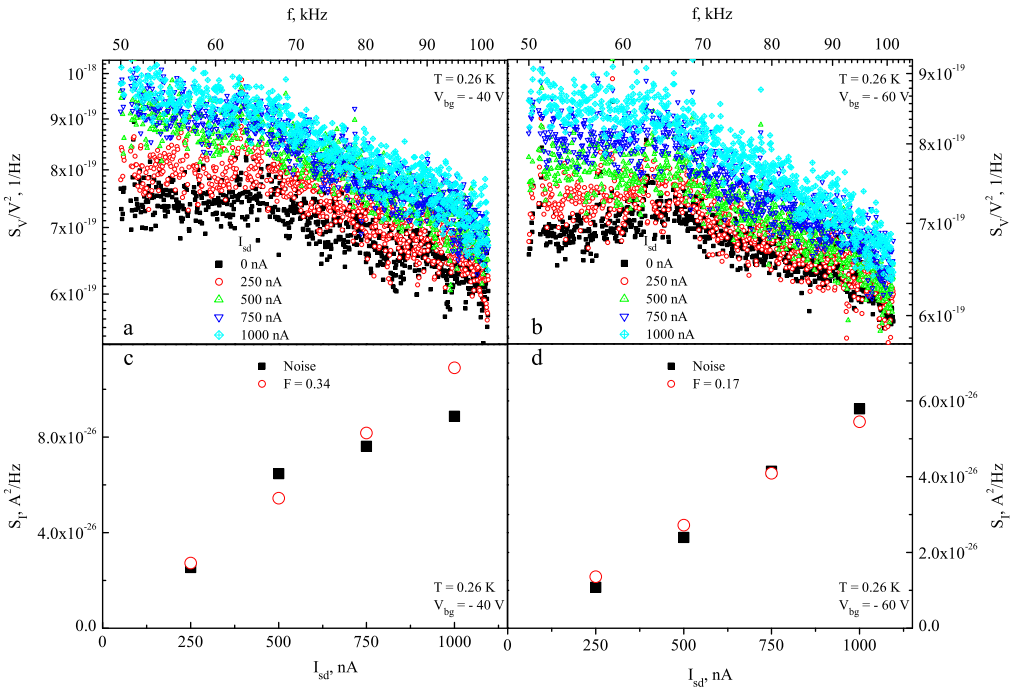

Figure 5.14: Shot noise in graphene at T=0.26 K. (a) Spectra for different source-drain currents for 50 a kHz span at -40 V on back-gate voltage. (b) Spectra for different source-drain currents for 50 a kHz span at -60 V on back-gate voltage. (c) Current noise (solid squares) as a function of current at $V_{bg} = -40$ V. Red circles show current noise at Fano factor equal 0.34. (d) Current noise as a function of current at $V_{bg} = -60$ V. Red circles show current noise at Fano factor equal 0.17.

Chapter 6

Conclusions and suggestions for further work

In this thesis the results of experimental studies of transport through double impurities placed in double-barrier resonant tunnelling diode, the ballistic transport of chiral particles through p-n junctions, and $1/f$ noise properties of graphene have been presented. It has been demonstrated that diffusive models can be applied to the diffusive graphene systems to explain the resistance dependence on back and top gate voltages. Also the magnetoresistance of a nonuniform sample can be explained by a geometrical magnetoresistance. It was shown that $1/f$ noise in graphene has much more complicated concentration and temperature dependence than that in usual metals.

We have used magnetic field parallel to the current to investigate resonant tunnelling through a double impurity in a vertical double-barrier resonant tunnelling diode, by measuring current-voltage and differential conductance-voltage characteristics. Information was obtained about the properties of the impurities: the energy levels, the effective electron mass and their spatial positions.

The chiral nature of the carriers in graphene has been demonstrated by comparing measurements of the transport through a ballistic p-n junction with the predictions of the diffusive models. This allowed us to find, unambiguously, the contribution of ballistic resistance to the total resistance of a p-n-p structure.

The first observation of $1/f$ noise in graphene has revealed a new feature not observed in conventional metals or semiconductors. The dip in the normalised noise

seen in the Dirac point of single-layer graphene at temperatures above 100 K still requires an explanation. A simple model of two different types of carrier in the Dirac point seems to be useful to explain the dip in the normalised noise.

Below are some suggestions for further work:

- We have not studied in detail the mutual arrangement of the impurities in the barriers of a DBRTD, but this can be done by rotation of magnetic field with respect to the current, in order to reveal the overlap between the wavefunctions of the two states.

- The studied graphene samples with *p*-*n*-*p* structures did not have large enough mean free path (or small enough *n*-region) to make the whole *p*-*n*-*p* structure fully ballistic. Making such structure would allow one to observe unambiguously the Klein paradox in graphene.

- We have not identified whether fluctuations in concentration or mobility are the main source of $1/f$ noise in graphene. This can be done using a Corbino disc geometry and measure the noise as a function of magnetic field to clarify this question.

Bibliography

[1] J. H. Devies. *The Physics of Low-Dimentional Semiconductors: an Introduction.* Cambridge University Press, Cambridge, (1998).

[2] B. M. Askerov. *Electron Transport Phenomena in Semiconductors.* World Scientific, Singapore, (1994).

[3] S. Datta. *Electronic Transport in Mesoscopic Systems.* Cambridge University Press, Cambridge, (1995).

[4] M. V. Entin. *private communication* .

[5] A. van der Ziel. *Noise in solid state devices and circuits.* Wiley-Interscience, (1986).

[6] Sh. Kogan. *Electronic noise and fluctuatiions in solids.* Cambridge University Press, Cambridge, (1996).

[7] R. F. Voss and J. Clarke. *Phys. Rev. Lett.* **40**, 913 (1976).

[8] R. F. Voss and J. Clarke. *Phys. Rev. B* **13**, 556 (1976).

[9] H. Wong. *Microelectronics Reliability* **43**, 585 (2003).

[10] M. B. Weissman. *Rev. Mod. Phys.* **60**, 537 (1988).

[11] A. L. Mc Whorter. *Semiconductor surface physics.* University of Pennsylvania press, Philadelphia.

[12] F. N. Hooge, T. G. M. Kleinpenning, and L. K. J. Vandamme. *Rept. Progr. Phys.* **44**, 479 (1981).

[13] P. Dutta and P. M. Horn. *Rev. Mod. Phys.* **53**, 497 (1981).

[14] C. W. J. Beenakker M. J. M. de Jong. *cond-mat/9611140* .

[15] Ya. M. Blanter and M. Büttiker. *Phys. Rep.* **336**, 1 (2000).

[16] S. S. Safonov, A. K. Savchenko, D. A. Bagrets, O. N. Jouravlev, Y. V. Nazarov, E. H. Linfield, and D. A. Ritchie. *Phys. Rev. Lett.* **91**, 136801 (2003).

[17] J. P. Holder. *Thesis: Resonant tunnelling spectroscopy of vertical GaAS/AlGaAs structures.* University of Exeter, (1999).

[18] K. S. Novoselov, D. Jiang, F. Schedin, T. J. Booth, V. V. Khotkevich, S. V. Morozov, and A. K. Geim. *PNAS* **102**, 10451 (2005).

[19] M. Ezawa. *Phys. Rev. B* **73**, 2006 (045432).

[20] Z. Chen, Y.-M. Lin, M. J. Rooks, and P. Avouris. *Physica E* **40**, 228 (2007).

[21] K. S. Novoselov, A. K. Geim, S. V. Morozov, D. Jiang, M. I. Katsnelson, I. V. Grigorieva, S. V. Dubonos, and A. A. Firsov. *Nature* **438**, 197 (2005).

[22] Y. Zhang, Y.-W. Tan, H. L. Stormer, and P. Kim. *Nature* **438**, 201 (2005).

[23] V. P. Gusynin and S. G. Sharapov. *Phys. Rev. Lett.* **95**, 146801 (2005).

[24] F. V. Tikhonenko, D. W. Horsell, R. V. Gorbachev, and A. K. Savchenko. *Phys. Rev. Lett.* **100**, 056802 (2008).

[25] W. R. Frensley. *Rev. Mod. Phys* **62**, 745 (1990).

[26] R. Tsu and L. Esaki. *Appl. Phys. Lett.* **22**, 562 (1973).

[27] M. W. Dellow, P. H. Beton, C. J. G. M. Langerak, T. J. Foster, P. C. Main, M. Henini, S. P. Beaumont, and C. D. W. Wilkinson. *Phys. Rev. Lett.* **68**, 1754 (1992).

[28] S. J. Bending and M. R. Beasley. *Phys. Rev. Lett.* **55**, 324 (1985).

[29] A. B. Fowler, G. L. Timp, J. J. Wainer, and R. A. Webb. *Phys. Rev. Lett.* **57**, 138 (1986).

[30] T. E. Kopley, P. L. McEuen, and R. G. Wheeler. *Phys. Rev. Lett.* **61**, 1654 (1988).

[31] J. P. Holder, A. K. Savchenko, V. I. Fal'ko, B. Jouault, G. Faini, F. Laruelle, and E. Bedel. *Phys. Rev. Lett.* **84**, 1563 (2000).

[32] H. C. Liu and G. C. Aers. *J. Appl. Phys.* **65**, 4908 (1989).

[33] P. C. Main, A. S. G. Thornton, R. J. A. Hill, S. T. Stoddart, T. Ihn, L. Eaves, K. A. Benedict, and M. Henini. *Phys. Rev. Lett.* **84**, 729 (2000).

[34] A. I. Larkin and K. A. Matveev. *Sov. Phys. JETP* **66**, 580 (1987).

[35] A. K. Savchenko, V. V. Kuznetsov, A. Woolfe, D. R. Mace, M. Pepper, D. A. Ritchie, and G. A. C. Jones. *Phys. Rev. B* **52**, 17021 (1995).

[36] E. Lind, B. Gustafson, I. Pietzonka, and L.-E. Wernersson. *Phys. Rev. B* **68**, 033312 (2003).

[37] T. Schmidt, R. J. Haug, K. v. Klitzing, A. F¨rster, and H. Lüth. *Phys. Rev. Lett.* **78**, 1544 (1997).

[38] V. Fock. *Z. Phys.* **47**, 446 (1928).

[39] I. E. Itskevich, T. Ihn, A. Thornton, M. Henini, T. J. Foster, P. Moriarty, A. Nogaret, P. H. Beton, L. Eaves, and P. C. Main. *Phys. Rev. B* **54**, 16401 (1996).

[40] T. Schmidt, R. J. Haug, Vladimir I. Fal'ko, K. v. Klitzing, A. F¨rster, and H. Lüth. *Phys. Rev. Lett.* **78**, 1540 (1997).

[41] G. Faini, C. Vieu, F. Laruelle, P. Krauz, E. Bedel, and C. Fontaine. *Surface Science* **361**.

[42] M. W. Dellow, P. H. Beton, C. J. G. Langerak, T. J. Foster, P. C. Main, L. Eaves, M. Henini, S. P. Beamont, and C. D. W. Wilkinson. *Phys. Rev. Lett.* **68**, 1754 (1991).

[43] V. V. Cheianov and V. I. Fal'ko. *Phys. Rev. B* **74**, 041403R (2006).

[44] K. S. Novoselov, A. K. Geim, S. V. Morozov, Y. Zhang D. Jiang, S. V. Dubonos, I. V. Grigorieva, and A. A. Firsov. *Science* **306**, 666 (2004).

[45] P. R. Wallace. *Phys. Rev.* **71**, 622 (1947).

[46] M. I. Katsnelson, K. S. Novoselov, and A. K. Geim. *Nature Physics* **2**, 620 (2006).

[47] M. I. Katsnelson. *Eur. Phys. J. B* **51**, 157 (2006).

[48] D. S. L. Abergel, A. Russell, , and Vladimir I. Fal'ko. *Appl. Phys. Lett.* **91**, 063125 (2007).

[49] P. Blake, E. W. Hill, A. H. Castro Neto, K. S. Novoselov, D. Jiang, T. J. Booth R. Yang, and A. K. Geim. *Appl. Phys. Lett.* **91**, 063124 (2007).

[50] A. C. Ferrari, J. C. Meyer, V. Scardaci, C. Casiraghi, M. Lazzeri, F. Mauri, S. Piscanec, D. Jiang, K. S. Novoselov, S. Roth, and A. K. Geim. *Phys. Rev. Lett.* **97**, 187401 (2006).

[51] N. M. R. Peres, F. Guinea, , and A. H. Castro Neto. *Phys. Rev. B* **73**, 125411 (2006).

[52] V. P. Gusynin, S. G. Sharapov, and J. P. Carbotte. *Int. J. Mod. Phys. B* **21**, 4611 (2007).

[53] A. H. Castro Neto, F. Guinea, N. M. R. Peres, K. S. Novoselov, and A. K. Geim. *Rev. Mod. Phys.* .

[54] Gordon W. Semenoff. *Phys. Rev. Lett.* **53**, 2449 (1984).

[55] T. Ando. *J. Phys. Soc. Jpn.* **74**, 777 (2005).

[56] A. K. Geim and K. S. Novoselov. *Nature Mater.* **6**, 183 (2007).

[57] J. H. Chen, C. Jang, M. S. Fuhrer, E. D. Williams, and M. Ishigami. *cond-mat/0708.2408* .

[58] S. V. Morozov, K. S. Novoselov, M. I. Katsnelson, F. Schedin, D. C. Elias, J. A. Jaszczak, and A. K. Geim. *Phys. Rev. Lett.* **100**, 016602 (2008).

[59] K. I. Bolotin, K. J. Sikes, Z. Jiang, M. Klima, G. Fudenberg, J. Hone, P. Kim, and H. L. Stormer. *Solid State Communications* **146**, 351 (2008).

[60] J. Martin, N. Akerman, G. Ulbricht, T. Lohmann, J. H. Smet, K. von Klitzing, and A. Yacoby. *Nature Physics* **4**, 144 (2008).

[61] T. Ando. *J. Phys. Soc. Jpn.* **75**, 074716 (2006).

[62] T. Ando, T. Nakanishi, and R. Saito. *J. Phys. Soc. Jpn.* **67**, 2857 (1998).

[63] N. H. Shon and T. Ando. *J. Phys. Soc. Jpn.* **67**, 2421 (1998).

[64] M. C. Lemme, T. J. Echtermeyer, and H. Kurz M. Baus. *IEEE Electron Dev. Lett.* **28**, 282 (2007).

[65] B. Huard, J. A. Sulpizio, N. Stander, K. Todd, B. Yang, and D. Goldhaber-Gordon. *Phys. Rev. Lett.* **98**, 236803 (2007).

[66] J. R. Williams, L. DiCarlo, and C. M. Marcus. *Science* **317**, 638 (2007).

[67] B. Özyilmaz, P. Jarillo-Herrero, D. Efetov, and P. Kim. *Appl. Phys. Lett.* **91**, 192107 (2007).

[68] J. B. Oostinga, H. B. Heersche, X. Liu, A. F. Morpurgo, and L. M. K. Vandersypen. *Nature Mater.* **7**, 151 (2007).

[69] R. V. Gorbachev, A. S. Mayorov, A. K. Savchenko, D. W. Horsell, and F. Guinea. *Nano Lett.* **8**, 1995 (2008).

[70] M. Razavy. *Quantum Theory of Tunneling.* World Scientific, Philadelphia, (2003).

[71] J. Tworzydło, B. Trauzettel, M. Titov, A. Rycerz, and C. W. J. Beenakker. *Phys. Rev. Lett.* **96**, 246802 (2006).

[72] E. Louis, J. A. Vergés, F. Guinea, and G. Chiappe. *Phys. Rev. B* **75**, 085440 (2007).

[73] H. H. Jensen and H. Smith. *J. Phys. C: Solid State Phys.* **5**, 2867 (1972).

[74] S. Cho and M. S. Fuhrer. *Phys. Rev. B* **77**, 084102 (2008).

[75] J. H. Scofield and D. M. Fleetwood. *IEEE Transactions on Nuclear Science* **38**, 1567 (1991).

[76] F. N. Hooge. *Phys. Lett. A* **29**, 139 (1969).

[77] F. N. Hooge. *Physica* **60**, 130 (1972).

[78] M. E. Levinshtein and S. L. Rumyantsev. *Sov. Phys. - Semiconductors* **17**, 1167 (1983).

[79] M.-Ho Song and H. S. Min. *J. Appl. Phys.* **58**, 4221 (1985).

[80] J. Appenzeller, Y.-M. Lin, J. Knoch, Z. Chen, and P. Avouris. *IEEE Trans. Nanotechnol.,* **6**, 368 (2007).

[81] M. Ishigami, J. H. Chen, E. D. Williams, D. Tobias, Y. F. Chen, and M. S. Fuhrer. *Appl. Phys. Lett.* **88**, 203116 (2006).

[82] Y.-M. Lin, J. C. Tsang, M. Freitag, and P. Avouris. *Nanotechnology* **18**, 295202 (2007).

[83] Y.-M. Lin and P. Avouris. *Nano Lett.* .

[84] V. V. Cheianov, V. I. Falko, B. L. Altshuler, and I.L. Aleiner. *Phys. Rev. Lett.* **99**, 176801 (2007).

[85] R. F. Voss. *J. Phys. C: Solid State Phys* **11**, L923 (1978).

[86] L. DiCarlo, J. R. Williams, Y. Zhang, D. T. McClure, and C. M. Marcus. *Phys. Rev. Lett.* **100**, 156801 (2008).

[87] C. H. Lewenkopf, E. R. Mucciolo, and A. H. C. Neto. *Phys. Rev. B* **77**, 081410 (2008).

Appendix A

Current amplitude in two-impurity tunnelling

Here we will discuss the integration of the conductance (Eq. 3.14) over energy from $-\infty$ to the Fermi energy μ. We neglect changes in the density of states. The integral is written as

$$I(V) = \int_{-\infty}^{\mu} \frac{e}{h} T(\varepsilon, \varepsilon_1, \varepsilon_2) d\varepsilon = \frac{e}{h} \int_{-\infty}^{\mu} \frac{4\Gamma_L \Gamma_R |H_{LR}|^2}{|(\varepsilon - \varepsilon_1 + i\Gamma_L)(\varepsilon - \varepsilon_2 + i\Gamma_R) - |H_{LR}|^2|^2} d\varepsilon \tag{A.1}$$

We are interested only in the current amplitude. The maximum of the current occurs at the resonance condition when the impurities have the same energy.

The four roots of the denominator in (A.1) are written as

$$\varepsilon_{I,II} = \frac{1}{2}\left(\varepsilon_1 + \varepsilon_2 - i(\Gamma_L + \Gamma_R)\right) \pm \sqrt{\frac{1}{4}\left[\varepsilon_1 - \varepsilon_2 - i(\Gamma_L - \Gamma_R)\right]^2 + |H_{LR}|^2}, \tag{A.2}$$

$$\varepsilon_{III,IV} = \frac{1}{2}\left(\varepsilon_1 + \varepsilon_2 + i(\Gamma_L + \Gamma_R)\right) \pm \sqrt{\frac{1}{4}\left[\varepsilon_1 - \varepsilon_2 + i(\Gamma_L - \Gamma_R)\right]^2 + |H_{LR}|^2}. \tag{A.3}$$

We know a simple link between energy levels (Eq. 3.18). It is possible to simplify expressions (A.2) and (A.3):

$$\varepsilon_{I,II} = \varepsilon^r - \frac{1}{2} i(\Gamma_L + \Gamma_R) \pm \sqrt{|H_{LR}|^2 - \frac{1}{4}(\Gamma_L - \Gamma_R)^2}, \tag{A.4}$$

$$\varepsilon_{III,IV} = \varepsilon^r + \frac{1}{2} i(\Gamma_L + \Gamma_R) \pm \sqrt{|H_{LR}|^2 - \frac{1}{4}(\Gamma_L - \Gamma_R)^2}. \tag{A.5}$$

We define $H = \sqrt{|H_{LR}|^2 - \frac{1}{4}(\Gamma_L - \Gamma_R)^2}$ and $\Gamma = \frac{1}{2}(\Gamma_L + \Gamma_R)$. If we assume that

$|H_{LR}|^2 > (\Gamma_L - \Gamma_R)^2/4$, then we can rewrite (A.4) and (A.5):

$$\varepsilon_{I,II} = \varepsilon^r - i\Gamma \pm H, \tag{A.6}$$

$$\varepsilon_{III,IV} = \varepsilon^r + i\Gamma \pm H. \tag{A.7}$$

The other possibilities, $|H_{LR}|^2 < (\Gamma_L - \Gamma_R)^2/4$ and $|H_{LR}|^2 = (\Gamma_L - \Gamma_R)^2/4$, we will consider below. Knowing the roots (A.6) and (A.7) for the denominator of the fraction under the integral we can factorise it to simplify integration. Combining ε_I with ε_{III} and ε_{II} with ε_{IV} we have

$$\begin{aligned}\frac{1}{|(\varepsilon-\varepsilon_1+i\Gamma_L)(\varepsilon-\varepsilon_2+i\Gamma_R)-|H_{LR}|^2|^2} &= \frac{1}{(\varepsilon-\varepsilon_I)(\varepsilon-\varepsilon_{II})(\varepsilon-\varepsilon_{III})(\varepsilon-\varepsilon_{IV})} \\ = \frac{1}{((\varepsilon-\varepsilon^r-H)^2+\Gamma^2)((\varepsilon-\varepsilon^r+H)^2+\Gamma^2)} &= \frac{1}{4H(H^2+\Gamma^2)}\left(\frac{\varepsilon-\varepsilon^r+2H}{(\varepsilon-\varepsilon^r+H)^2+\Gamma^2}\right. \\ \left. -\frac{\varepsilon-\varepsilon^r-2H}{(\varepsilon-\varepsilon^r-H)^2+\Gamma^2}\right)\end{aligned} \tag{A.8}$$

The last expression can be easily integrated. Consider the first term in the last expression (A.8):

$$\begin{aligned}\int_{-\infty}^{\mu}\frac{(\varepsilon-\varepsilon^r+H)+H}{(\varepsilon-\varepsilon^r+H)^2+\Gamma^2}d\varepsilon &= \int_{-\infty}^{\mu}\frac{(\varepsilon-\varepsilon^r+H)d(\varepsilon-\varepsilon^r+H)}{(\varepsilon-\varepsilon^r+H)^2+\Gamma^2} \\ +\int_{-\infty}^{\mu}\frac{H}{(\varepsilon-\varepsilon^r+H)^2+\Gamma^2}d\varepsilon &= \frac{1}{2}\int_{-\infty}^{\mu}d\ln((\varepsilon-\varepsilon^r+H)^2+\Gamma^2) \\ &+\frac{H}{\Gamma}\int_{-\infty}^{\mu}\frac{d((\varepsilon-\varepsilon^r+H)/\Gamma)}{((\varepsilon-\varepsilon^r+H)/\Gamma)^2+1} \\ = \frac{1}{2}\lim_{x\to-\infty}(\ln\left((x+H-\varepsilon^r)^2+\Gamma^2\right)) &+\frac{1}{2}\ln\left((\mu+H-\varepsilon^r)^2+\Gamma^2\right) \\ &+\frac{H}{\Gamma}\left[\tan^{-1}\left(\frac{\mu+H-\varepsilon^r}{\Gamma}\right)+\frac{\pi}{2}\right].\end{aligned} \tag{A.9}$$

The first term in (A.9) is infinite but the second term in (A.8) provides a similar negative value which cancels this divergence. The full expression for the current amplitude is

$$\begin{aligned}I_{max} = \frac{e}{h}\frac{\Gamma_L\Gamma_R|H_{LR}|^2}{H(H^2+\Gamma^2)}&\left[\frac{1}{2}\ln\left(\frac{(\mu+H-\varepsilon^r)^2+\Gamma^2}{(\mu-H-\varepsilon^r)^2+\Gamma^2}\right)+\right. \\ +\frac{H}{\Gamma}&\left.\left[\tan^{-1}\left(\frac{\mu+H-\varepsilon^r}{\Gamma}\right)+\tan^{-1}\left(\frac{\mu-H-\varepsilon^r}{\Gamma}\right)+\pi\right]\right],\end{aligned}$$

which is (3.19) in the text.

If we have $|H_{LR}|^2 < (\Gamma_L - \Gamma_R)^2/4$ than the answer for the current amplitude is

$$I_{max} = \frac{e}{\hbar}\frac{\Gamma_L\Gamma_R|H_{LR}|^2}{\Gamma H(\Gamma^2 - H^2)}\left(\pi H + (\Gamma + H)\tan^{-1}\frac{\mu - \varepsilon^r}{\Gamma - H} - (\Gamma - H)\tan^{-1}\frac{\mu - \varepsilon^r}{\Gamma + H}\right), \tag{A.10}$$

where $\Gamma = 1/2(\Gamma_L + \Gamma_R)$ and $H = \sqrt{-|H_{LR}|^2 + \frac{1}{4}(\Gamma_L - \Gamma_R)^2}$. Otherwise, if $|H_{LR}|^2 = (\Gamma_L - \Gamma_R)^2/4$ the answer is more simple

$$I_{max} = \frac{e}{\hbar}\frac{\Gamma_L\Gamma_R|H_{LR}|^2}{\Gamma^3}\left(\pi + \frac{\Gamma(\mu - \varepsilon^r)}{(\mu - \varepsilon^r)^2 + \Gamma^2} + 2\tan^{-1}\frac{\mu - \varepsilon^r}{\Gamma}\right). \tag{A.11}$$

Appendix B

Code for solving 2D Laplace equation (FEMLab)

```
format long
flclear fem

Graphene_flake_length=4.3e-6;
Dielectric_thickness=3.0E-7;
Small_box_width=1e-5;
Top_gate_length=170e-9;
Top_gate_heigth=250e-9;
Top_gate_distance=210e-9;
Box_width=2*Small_box_width+Graphene_flake_length;
Box_heigth=5.7E-6;
Impurities_distance=3.1E-7;

% Geometry
g2=rect2(Graphene_flake_length,Dielectric_thickness,'base','corner',....
'pos',[-Graphene_flake_length/2,0]);
g4=rect2(Small_box_width,Dielectric_thickness,'base','corner',...
'pos',[-Small_box_width-Graphene_flake_length/2,0]);
g6=rect2(Small_box_width,Dielectric_thickness,'base','corner',...
'pos',[Graphene_flake_length/2,0]);
g8=rect2(Box_width,Box_heigth,'base','corner','pos',[-Box_width/2,...
Dielectric_thickness]);
carr={curve2([-2.15E-6,2.15E-6],[Impurities_distance,...
Impurities_distance],[1,1])};
g9=geomcoerce('curve',carr);
gg=geomedit(g9);
g10=geomedit(g9,gg);
g11=geomcomp({g2,g4,g6,g8},'ns',{'g2','g4','g6','g8'},'sf',...
'g2+g4+g6+g8','edge','none');
g13=rect2(Top_gate_length,Top_gate_heigth,'base','center','pos',...
[0,Top_gate_distance+Dielectric_thickness+Top_gate_heigth/2]);
```

```
g15=geomcomp({g11,g13},'ns',{'g11','g13'},'sf','g11-g13','edge','none');

% Analyzed geometry
clear c s
c.objs={g10};
c.name={'B1'};
c.tags={'g10'};

s.objs={g15};
s.name={'CO2'};
s.tags={'g15'};

fem.draw=struct('c',c,'s',s);
fem.geom=geomcsg(fem);

% Initialize mesh
fem.mesh=meshinit(fem, ...
                  'hauto',5);

% Initialize mesh
fem.mesh=meshinit(fem, ...
                  'hauto',5, ...
                  'hmaxedg',[10,1e-8,11,1e-8,12,1e-8,13,1e-8]);

% (Default values are not included)

e=1.60217733*1e-19;
h=6.6260755*1e-34/(2*3.1415926);
e0=8.854187817e-12;
er=3.9;
d=3e-7;
vf=1e6;
C=er*e0/d;
rs=e^3/(3.1415926*h^2*vf^2);
GV=1/sqrt(rs/C);
Vdp=0.93;
Ef0=-1e-3/GV*sqrt(Vdp);
Density=strcat('-',num2str(rs),'*V^2*sign(V)');

Charge_density=strcat(num2str(sign(Ef0)*rs),'*',num2str(Ef0^2));

Rvtg=zeros(1,21);
for jj=1:1
Backgate_voltage=-4;
%Topgate_voltage=-66+jj*6;
Topgate_voltage=20;

Contact_Potential=GV*sqrt(abs(Backgate_voltage))*sign(Backgate_voltage);
```

```
% Application mode 1
clear appl
appl.mode.class = 'EmElectrostatics';
appl.module = 'ACDC';
appl.border = 'on';
appl.assignsuffix = '_emes';
clear bnd
bnd.rhos = {0,0,0,0,Density,Charge_density,0};
bnd.V0 = {0,Backgate_voltage,Contact_Potential,0,0,0,...
Topgate_voltage};
bnd.type = {'nD0','V','V','cont','r','r','V'};
bnd.name = {'Box','Backgate','Contacts','','Graphene',...
'Impurities','Topgate'};
bnd.ind = [1,2,1,3,1,4,2,5,6,7,7,7,7,4,2,3,1,1];
appl.bnd = bnd;
clear equ
equ.epsilonr = {3.9,1};
equ.name = {'Dielectric','Vacuum'};
equ.ind = [1,2,1,1];
appl.equ = equ;
fem.appl{1} = appl;
fem.frame = {'ref'};
fem.border = 1;
clear units;
units.basesystem = 'SI';
fem.units = units;

% Multiphysics
fem=multiphysics(fem);

% Extend mesh
fem.xmesh=meshextend(fem);

% Solve problem
fem.sol=femstatic(fem, ...
                  'solcomp',{'V'}, ...
                  'outcomp',{'V'}, ...
                  'linsolver','gmres');

% Save current fem structure for restart purposes
fem0=fem;

postplot(fem, ...
         'contdata',{'V','cont','internal','unit','V'}, ...
         'contlevels',20, ...
         'contlabel','off', ...
         'contmap','cool(1024)', ...
         'title','Contour: Electric potential [V]', ...
         'axis',[-1.5616550440727387E-6,1.7905022732366362E-6,...
```

```
        -9.184963735485299E-7,1.6417052435411149E-6,-1,1]);

% Plot in cross-section or along domain
[h,data]=postcrossplot(fem,1,[-2.15e-6 2.15e-6;300e-9 300e-9], ...
    'lindata','V', ...
    'linxdata','x', ...
    'title','Electric potential [V]', ...
    'axislabel',{'x','Electric potential [V]'});

subintegral=strcat('if(V^2*sign(V)*',num2str(1/GV^2),'>0,...
if(V^2*sign(V)*',num2str(1/GV^2),'>3,1/(0.00356+...
0.02904*V^2*sign(V)*',num2str(1/GV^2),')+5.5,1/(0.03271+...
0.00339*V^2*sign(V)*',num2str(1/GV^2),'+0.00824*(V^2*sign(V)*...
',num2str(1/GV^2),')^2-9.41747E-4*(V^2*sign(V)*',...
num2str(1/GV^2),')^3)+5.5),if(V^2*sign(V)*',num2str(1/GV^2),...
'<-5,1/(0.03416-0.01303*V^2*sign(V)*',num2str(1/GV^2),')+...
1.7,1/(0.0302-0.0027*V^2*sign(V)*',num2str(1/GV^2),'+...
0.00497*(V^2*sign(V)*',num2str(1/GV^2),')^2+5.57394E-4*...
(V^2*sign(V)*',num2str(1/GV^2),')^3)+1.7))');

% Integrate
I3=postint(fem,subintegral, ...
           'unit','', ...
           'dl',[8], ...
           'edim',1);

jj
I3/4.3e-6
Rvtg(jj)=I3/4.3e-6;
end
```

Appendix C

Mathematica code for qtans3 function to find $T(\theta)$ of a p-n-p structure (courtesy of F. Guinea)

```
gtrans3[w_, nn_, ep_, em_, k_, en1_] :=Module[{ww, fp, ffp, fm, ffm,
green1, green2, greend1, greend2, green, cc, tfp, tfm, auxp, auxm},
cc = 2*Cos[k/2]; For[i = 1, i < n + 2, {
tt[i] = ((1 + cc)/2 - (1 - cc)/2*(-1)^i)*t;
          en[i] = potential[en1, i]};i++];
      tfp = t*t*cc/(w - ep);
      wp = ((w - ep)*(w - ep) - t*t - t*t*cc*cc)/(w - ep);
      wwp = wp/(2*tfp); auxp = Sqrt[wp*wp/4 - tfp*tfp];
      If[wp*wp/4 - tfp*tfp > 0, fp = wp/2 - Sign[wp]*auxp,
      fp = wp/2 - auxp]; ffp = t*t/(w - ep) + fp;
      tfm = t*t*cc/(w - em);
      wm = ((w - em)*(w - em) - t*t - t*t*cc*cc)/(w - em);
      wwm = wm/(2*tfm);
      auxm = Sqrt[wm*wm/4 - tfm*tfm];
      If[wm*wm/4 - tfm*tfm > 0, fm = wm/2 - Sign[wm]*auxm,
      fm = wm/2 - auxm]; ffm = t*t*cc*cc/(w - em) + fm;
      tp[n] = tt[n]/(w - en[n + 1] - ffp);
      For[i = 1, i < n, {tp[n - i] =tt[n - i]/(w - en[n - i + 1] -
          tt[n - i + 1]*tp[n - i + 1])};i++];
      tm[1] = tt[1]/(w - en[1] - ffm);
      For[i = 2, i < n + 1, {
          tm[i] = tt[i]/(w - en[i] - tt[i - 1]*tm[i - 1])};i++];
      green1 = 1/(w - en[nn] - tt[nn - 1]*tm[nn - 1] -
      tt[nn]*tp[nn]);
      green2 = 1/(w - en[nn + 1] - tt[nn]*tm[nn] -
      tt[nn + 1]*tp[nn + 1]);
      greend1 = tm[nn]*green2;greend2 = tp[nn]*green1;
      green =2*tt[nn]^2*(2*Im[green1]*Im[green2] - Im[greend1]^2 -
      Im[greend2]^2)];
```

Appendix D

Code for solving 2D Laplace equation and finding the resistance of a p-n-p structure

```
format long
flclear fem

Graphene_flake_length=5e-6; Dielectric_thickness=3.0E-7;
Small_box_width=1e-5; Top_gate_length=170e-9;
Top_gate_heigth=250e-9; Top_gate_distance=140e-9;
Box_width=2*Small_box_width+Graphene_flake_length;
Box_heigth=5.7E-6; Impurities_distance=3.1E-7;

% Geometry
g2=rect2(Graphene_flake_length,Dielectric_thickness,...
'base','corner','pos',[-Graphene_flake_length/2,0]);
g4=rect2(Small_box_width,Dielectric_thickness,'base',...
'corner','pos',[-Small_box_width-Graphene_flake_length/2,0]);
g6=rect2(Small_box_width,Dielectric_thickness,'base',...
'corner','pos',[Graphene_flake_length/2,0]);
g8=rect2(Box_width,Box_heigth,'base','corner','pos',...
[-Box_width/2,Dielectric_thickness]);
carr={curve2([-Graphene_flake_length/2,Graphene_flake_length/2],...
[Impurities_distance,Impurities_distance],[1,1])};
g9=geomcoerce('curve',carr);
gg=geomedit(g9);
g10=geomedit(g9,gg);
g11=geomcomp({g2,g4,g6,g8},'ns',{'g2','g4','g6','g8'},'sf',...
'g2+g4+g6+g8','edge','none');
g13=rect2(Top_gate_length,Top_gate_heigth,'base','center',...
'pos',[Graphene_flake_length/6-Top_gate_length/2,...
Top_gate_distance+Dielectric_thickness+Top_gate_heigth/2]);
g15=geomComp({g11,g13},'ns',{'g11','g13'},'sf','g11-g13',...
'edge','none');

% Analyzed geometry
```

```
clear c s
c.objs={g10};
c.name={'B1'};
c.tags={'g10'};

s.objs={g15};
s.name={'CO2'};
s.tags={'g15'};

fem.draw=strUct('c',c,'s',s);
fem.geom=geomcsg(fem);

% Initialize mesh
fem.mesh=meshinit(fem, ...
'hauto',5);

% Initialize mesh
fem.mesh=meshinit(fem, ...
'hauto',5, ...
'hmaxedg',[10,1e-8,11,1e-8,12,1e-8,13,1e-8]);

% (Default values are not included)
e=1.60217733*1e-19; h=6.6260755*1e-34/(2*3.1415926); e0=8.854187817e-12;
er=3.9; d=3e-7; vf=1e6; C=er*e0/d; rs=e^3/(3.1415926*h^2*vf^2);
GV=1/sqrt(rs/C); Vdp=0.05; Ef0=-1e-3/GV*sqrt(abs(Vdp))*sign(Vdp);
Density=strcat('-',num2str(rs),'*V^2*sign(V)');
Charge_density=strcat(num2str(sign(Ef0)*rs),'*',num2str(Ef0^2));

Rvtg=zeros(1,100); RpnG=zeros(1,100);
sec=zeros(1,100);
secFano=zeros(1,100);
for jj=1:100
 Backgate_voltage=-9; Topgate_voltage=19+21*jj/100;
 Contact_Potential=GV*sqrt(abs(Backgate_voltage))*sign(Backgate_voltage);

% Application mode 1
clear appl
appl.mode.class = 'EmElectrostatics';
appl.module = 'ACDC';
appl.border = 'on';
appl.assignsuffix = '_emes';
clear bnd
bnd.rhos = {0,0,0,0,Density,Charge_density,0};
bnd.V0 = {0,Backgate_voltage,Contact_Potential,0,0,0,...
Topgate_voltage};
bnd.type = {'nD0','V','V','cont','r','r','V'};
bnd.name = {'Box','Backgate','Contacts','','Graphene',...
'Impurities','Topgate'};
bnd.ind = [1,2,1,3,1,4,2,5,6,7,7,7,7,4,2,3,1,1];
```

```
appl.bnd = bnd;
clear equ
equ.epsilonr = {3.9,1};
equ.name = {'Dielectric','Vacuum'};
equ.ind = [1,2,1,1];
appl.equ = equ;
fem.appl{1} = appl;
fem.frame = {'ref'};
fem.border = 1;
clear units;
units.basesystem = 'SI';
fem.units = units;

% Multiphysics
fem=multiphysics(fem);

% Extend mesh
fem.xmesh=meshextend(fem);

% Solve problem
fem.sol=femstatic(fem, ...
'solcomp',{'V'}, ...
'outcomp',{'V'}, ...
'linsolver','gmres');

% Save current fem structure for restart purposes
fem0=fem;

left=-250e-9;
right=750e-9;
points=3000;
[h,data]=postcrossplot(fem,1,[left right;300e-9 300e-9], ...
'lindata','V', ...
'linxdata','x', ...
'npoints',points, ...
'title','Electric potential [V]', ...
'axislabel',{'x','Electric potential [V]'});

pot=data.p(2,:)';

%Guinea
n = 3000; n0 = n; w = 0;
enpot=zeros(2*n,1);
en=zeros(n+1,1);
for ii = 1:n
    enpot(ii)=pot(ii);
    enpot(2*n+1-ii)=pot(ii);
end
```

```
for ii = 1:n
    en(ii) = enpot(2*ii);
end


nn1 = 40; em = en(1); ep = en(n); en(n + 1) = en(n);
t0 = 3; length = 2*10^3; aa = 1.4; length1 = 3/4*aa*n0/10;
t = t0*length1/length;


nphi = 1;
W=235e-9;
hbar=1.055e-34;
e=1.602e-19;
vf=1e6;

W=235e-9;
kn=pi/W*1e-10;
for ll=1:20
 q=qtrans3(w, nn1, ep, em, 2*pi/3 + kn*(ll-1/2)*aa*sqrt(3),en,n,t);
 sec(jj) = sec(jj) +q;
 secFano(jj)=secFano(jj)+q*(1-q);
end

secFano(jj)=secFano(jj)/sec(jj);
end
```